Analysis of thermoelectric materials with atomic spectrometric methods

Doctoral dissertation
for the granting of the degree
“Doctor rerum naturalium”

Submitted by
Dipl.Chem. Klaus-Georg Reinsberg
born in Cologne

to the Institute for Inorganic and Applied Chemistry
University of Hamburg
Department of Chemistry

Hamburg 2013

1. Gutachter: Prof. Dr. J.A.C. Broekaert

2. Gutachter: Dr. M. Steiger

Datum der Disputation: 26.07.2013

I would like to express my gratitude for the opportunity to work in his research group and for his faith in my decisions concerning my research to Prof. Dr. J.A.C. Broekaert.

Prof. Dr. K. Nielsch I thank for the organization of the “EChemTE” project and for always giving me the opportunity to get an insight into the interesting field of thermoelectrics.

For the great teamwork and the helpful discussions concerning the organization of the work I thank Dr. C. Schumacher.

Dr. Anges Tempez I thank for the great opportunity to perform measurements in the laboratories of Horiba Jobin Yvon in France and for the help at the GD-TOF-MS.

Dr. U.E.A. Fittschen I thank for the organization of beamtimes at the Hasylab and for spending long evening ours with me during the course of these measurements.

My thankfulness I would like to express to my good fried M.Sc. K.K. Moß to spare no effort and always trusting in my advice over the years in different projects I was lucky to guide.

I would like to thank L. Hermann for being good humored every time we met in her laboratory at the ICP-MS and elsewhere.

T. Krugmann I thank for her helpfulness in the work with the AAS and her valuable advice.

The whole workgroup and especially Dipl. Chem. M. Menzel for the friendliness over the last years.

My deepest gratitude I express to Mihaela my beloved wife for her never-ending and unquestioning support.

“The Bundesministerium für Bildung und Forschung” is acknowledged for financial support of the “EChemTE” project.

Contents

1 Introduction

1.1 Motivation

Thermoelectric materials convert heat into electrical power and can be used to recover energy wherever it is lost by extensive waste heat production. Examples for utilization are the automotive industry and combustion plants where waste heat can be regenerated. Smaller applications are wireless energy self-sustaining sensors for process control e.g. in chemical processes. For these kind of applications thermoelectrics will compete with batteries regarding costs of production and maintenance. One of the most famous applications of thermoelectric generators (TEG) have been space missions such as NASA's "Cassini" mission, where a long lasting ^{238}U radionuclide as heat source drives a TEG[1].

For room temperature use in the field of thermoelectrics, Bi_2Te_3 and Sb_2Te_3 and chalcogenides based on them like $Bi_{2-x}Sb_xTe_3$ or $Bi_2Te_{3-y}Se_y$ are the materials of choice[2–4]. Typically these materials are synthesized by directional crystallization, powder metallurgy processes or evaporation methods[3]. Also fabrication from the gas phase such as molecular beam epitaxy (MBE) and atomic layer deposition (ALD) lead to good material quality and are widely accepted[5]. Since such high vacuum methods are expensive a less cost intensive production method like the electrochemical deposition from an aqueous electrolyte is required. It offers an alternative to the classical methods[3] due to the comparably easy control over process parameters such as electrolyte bath composition and deposition potential[5].

The synthesis of Bi_2Te_3 with electrochemical deposition of layers has been widely described in the literature[3,6–15]. Also the synthesis of nano-structured thermoelectric materials, which promise higher thermoelectric efficiency[16,17], by electrochemical deposition was realized[18–20]. Due to the more challenging synthesis of Sb_2Te_3 less is published in this field[11,12,21–23]. The ternary compounds, such as $Bi_{2-x}Sb_xTe_3$ or $Bi_2Te_{3-y}Se_y$ were found to offer a higher thermoelectric efficiency than these binary compounds[1]. Some examples for synthesis of $\mathrm{Bi_{2-x}Sb_xTe_3}$[24–27] and $\mathrm{Bi_2Te_{3-y}Se_y}$[28–33] have been published.

The stoichiometry[2,34] and micro-structure[35] of thermoelectric materials are two key parameters for their thermoelectric performance. The micro-structure of electrochemically deposited $\mathrm{Bi_2Te_3}$ films was investigated by Takahashi et al.[10] and a change of the Te concentration with the depth was found. Li et al[14]. showed for non-stoichiometric deposits that grains with a different composition as compared to the bulk composition can be found. In many synthesis orientated publications[3,6–15,18–33] the development of good thermoelectric materials[5] is described but they often suffer from a lack of a detailed chemical characterization.

For the chemical analysis of thermoelectric materials energy dispersive X-ray fluorescence spectrometry coupled to a scanning electron microscope (SEM-EDS) or coupled to a tunneling electron microscope (TEM-EDS) has been used. Due to its ability to visualize the sample morphology SEM techniques are popular and the coupling of an EDS detector is a fast and simple way for additional chemical analysis. For films a SEM is suitable and for nano-size structures a TEM in most cases is used for the analysis of thermoelectric materials. In a few cases wavelength dispersive X-ray fluorescence spectrometry (WDS) is coupled to the SEM or TEM. Only a few authors make use of atomic spectrometric analytical methods like atomic absorption spectrometry (AAS)[22], or optical emission spectrometry with an inductively coupled plasma (ICP-OES)[10,26] for bulk analysis. Also the use of a glow discharge source for depth profile analyses (GD-OES)[10,26] has been used, despite these methods have been routinely used for metal analyses for many decades[36–38]. A series of reviews on atomic spectrometry cited hundreds of publications dealing with applications of atomic spectrometry from 1986 onwards. They deal e.g. with environmental analysis[39], food and clinical materials analysis[40], chemicals, iron, steel and non ferrous metals analysis[41] and mineral analysis[42].

When performing a determination of the main components in thermoelectric films many authors do not evaluate the precision or the accuracy of their results obtained typically with SEM-EDS. Some mention relative standard deviations down to 1%. For such measurements 10 replicates and an external calibration with solid sample standards was applied by Michel et al.[31,32]. Rostek et al.[15] covered a relatively large area of 0.3 mm^2 to achieve standard deviations of 0.5 at.%, which is also about a 1% relative standard deviation (RSD). For nanowires the measurements are more difficult as a result of the sample size. Measurements here are typically carried out with a transmission electron microscope using energy dispersive X-ray spectrometry (TEM-EDS). Martin-Gonzalez[30] reports for single nanowires typical standard deviations of 3 at.%, which corresponds to RSDs of approximately 5%. A detailed work on precise main component determinations with TEM-EDS has been published by Peranio and Eibl[43]. In their work they describe the effort which is needed for accurate and precise determinations with TEM-EDS. They are able to reach precisions below the 1% level for elements which have concentrations of beyond 30% in the samples, but their accuracy depends ultimately on the availability of reference samples. The ususally high standard deviations for small samples, such as nanowires, are due to the relatively high detection limits of EDS analyses, which are of the order of 0.1 to 1 wt.%. Indeed, the probed volume is of the order of 1 μm^3, which includes also the sample carrier[44]. Furthermore, for the elements under investigation in this work Bi, Sb, Te and Se EDS has only relatively high detection limits due to the interferences of the fluorescence lines with the bremsstrahlung background from decelerated electrons and due to the relatively low excitation energies of the electrons[44,45].

Especially the control of the homogeneity with respect to Seebeck values is used as an important tool for materials characterization in the field of thermoelectrics. The potential Seebeck microprobe (PSM) technique here is used as an indirect indication of the samples homogeneity[46]. It was reported that it is possible with this technique to detect inhomogeneities, different phases, even different doping levels or anisotropies, which is according to Platzek et al.[47] cannot be detected with other techniques such as SEM-EDS. With the PSM, however there is no possibility to distinguish between the different material parameters, which influence the Seebeck coefficient. Therefore, with atomic spectrometric methods such as ICP-OES/MS, AAS, GD-OES/MS, X-ray fluorescence spectrometry (XRF) and X-ray powder diffraction (XRD) more detailed information on the material properties can be obtained.

1.2 Outline

Within the frame of the “EChemTE” project the influence of the synthesis conditions in electrochemical deposition on the physical and chemical materials properties of thermoelectric materials were determined. Thermoelectric properties such as electrical conductivity (σ), thermal conductivity (κ) and the so-called Seebeck coefficient ($S = \Delta U/\Delta T$), the generated voltage for an applied temperature difference) critically depend on the composition and the homogeneity of the materials. This necessitates precise and accurate determinations of the main components and a detailed investigation of the sample homogeneity[48–50]. With appropriate atomic spectrometric methods, such as inductively coupled plasma optical emission spectrometry (ICP-OES) or inductively coupled plasma mass spectrometry (ICP-MS), glow discharge time-of-flight mass spectrometry (GD-TOF-MS), high resolution graphite furnace atomic absorption spectrometry (HR-GF-AAS), total reflection X-ray fluorescence (TXRF), micro-X-ray fluorescence (µ-XRF), micro-X-ray diffraction (µ-XRD) and X-ray absorption near edge structure analysis (XANES), bulk compositions, the in-depth and lateral homogeneity, oxidation states and crystal structures were determined.

To give an insight in the nature of thermoelectric materials, their structure and the process of electrochemical deposition a short introductions will be given in the Sections 1.3.1, 1.3.2 and 1.3.3. More detailed informations have been described by Schumacher[5], who performed within the Ph.D dissertation experimental work on the electrochemical deposition of thermoelectric materials and on their physical characterization. Results from his work in part will also be shown in this dissertation and vice versa analytical results obtained in our work were also used by Schumacher.

In chapter 2 the analytical methods, which were used throughout the work will be described. In chapter 3 the experimental conditions, which were selected are given in detail. In the chapters 4 and 5 investigations on thermoelectric layers with respect to bulk stoichiometry, structure and homogeneity will be presented. In Section 4.2 a procedure for the precise determination of the main components of the thermoelectric materials with ICP-OES will be described. In Section 4.3 the results of a structural characterization of thermoelectric layers with XRD will be given. In Sections 5.2 and 5.3 two procedures for the investigation of the materials homogeneity are presented. First, the in-depth homogeneity has been studied with

GD-TOF-MS (Section 5.2) and in Section 5.3 the investigation of the lateral homogeneity with Synchrotron μ-XRF and μ-XRD primarily is shown. Further, the findings of μ-XRF and μ-XRD were discussed in view of the results obtained for the thermoelectric properties of the materials, such as the results of PSM. In chapter 6 investigations on nano-structured materials with HR-GF-AAS, TXRF (Section 6.2) and ICP-MS (Section 6.3) will be presented. Each chapter will be preceded by a short introduction on the topic of the chapter and be followed by a discussion of the findings presented in the chapter.

1.3 Thermoelectric materials

1.3.1 Thermoelectric properties

The basic principles and parameters, which contribute to the performance of thermoelectric materials are presented below. In a homogeneous (semi-)conductor at a fixed temperature, charge carriers are distributed over the valence band and the conduction band. With increasing temperature the number of charge carriers in the valence band increases. When the ends of the (semi-)conductor are subjected to two different temperatures the number of charge carriers at the warm side, which are in the conduction band, will be higher than the number at the cold side. Due to the concentration gradient for the charge carriers they will move to the cold side. The effect is called thermo-diffusion and as a result of it a thermo-diffusion voltage is generated between the warm side and the cold side, which ultimately cancels the thermo-diffusion process. The warm side will be charged negative in n (semi-)conductors and positive in p (semi-)conductors. The thermo-diffusion voltage is proportional to the temperature difference between the warm and the cold side. The proportionality factor S is called the Seebeck coefficient, which is a material dependent constant. The described effect appears in all conductors but it is more pronounced for semiconductors[1,51].

To generate an electrical current at least two semi-conductors, one of them p conducting the other one n conducting, have to be connected electrically in series and thermally in parallel[1,52] as it is shown in Figure 1.1. This combination is called a thermocouple and it has two thermoelectric legs. Every positively charged end of a leg is connected to a negatively charged end of a leg, whereas a warm end is connected to a another warm end as it is the same for the cold ends of the legs. The generator uses a heat flow across a temperature gradient to power an electrical circuit. Due to the temperature difference a voltage is provided and the heat flow determines the electrical current[52].

To achieve a high value for S the material in each leg should have only one type of charge carriers so as to avoid an extinction of the heat induced Seebeck effect. The density of the charge carriers in such a material should be high enough so as to enable electrical conduction, but on the other hand not to high so as to avoid a high amount of thermal conduction, which reduces the temperature difference. Since the thermal and electrical conductivity are

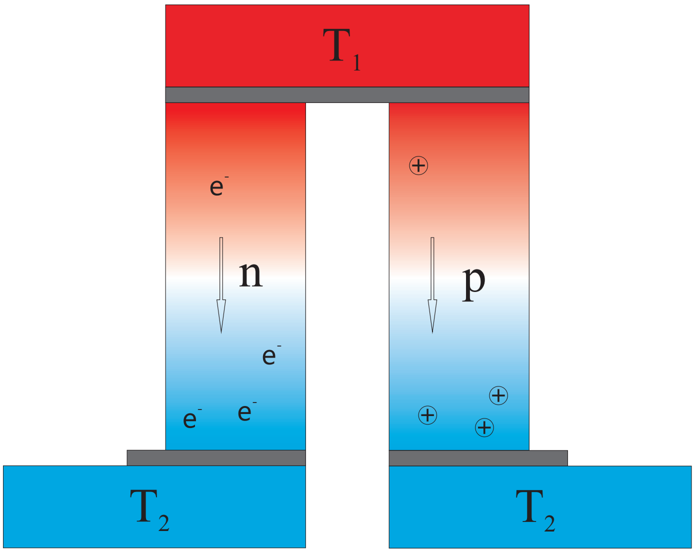

Figure 1.1: Working principle of a Thermocuple.

linked together over the Wiedemann-Franz-law (see Equation 1.1), they cannot be optimized separately[1].

$$\kappa = T\frac{\pi^2}{3}\left(\frac{k}{e}\right)^2\sigma \tag{1.1}$$

Here κ is the thermal conductivity, T is the temperature, k is the Boltzmann constant, e is the elementary electric charge and σ the electrical conductivity.

One goal is to find an optimum for the ratio between electrical and thermal conductivity. In contrast to the thermal conduction by electrons the thermal conduction by phonons does not depend on the electrical conduction[1]. Consequently, the performance of the material can be improved by reducing the heat conduction. This can be achieved according to the “electron crystal phonon glass” concept. The heat conduction by phonons can be reduced by site substitution (alloying) with iso-electronic elements, by which the crystalline electronic structure is preserved while creating large mass contrast to disrupt the phonon path. Typically an optimum charge carrier concentration is found in heavily doped semiconductors. The properties of these materials almost resemble those of metals with respect to their electrical conduction[52].

The dimensionless figure of merit for thermoelectric materials for an average working temperature (T) is the ZT value, which includes κ, σ and S. As described above an ideal thermoelectric material is a good electrical conductor but a bad thermal conductor, as it is described by Equation 1.2.

$$ZT = \frac{S^2\sigma}{\kappa}T \tag{1.2}$$

The ZT value depends on the temperature, which leads to the fact that the working ranges for different types of thermoelectric materials are as shown in Figure 1.2. For applications at temperatures near to the room temperature Bi_2Te_3 alloys have the best figures of merit in the case of n type semiconductors. The iso-structural Sb_2Te_3 has the best ZT values in the case of p type conduction. The iso-structural alloys such as $Bi_{2-x}Sb_xTe_3$ (p conduction) and $Bi_2Te_{3-y}Se_y$ (n conduction) are often used as well. The optimum stoichiometries for them were found to be $Bi_{0.4}Sb_{1.6}Te_3$ and $Bi_2Te_{1.6}Se_{0.4}$[52].

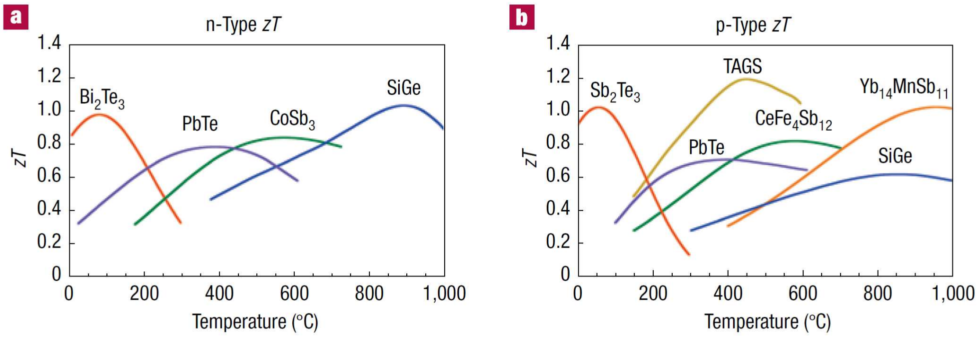

Figure 1.2: Working ranges for thermoelectric materials of the n-type (a) and p-type (b)[52].

1.3.2 Crystallographic structure

The rombohedral lattice system of Bi_2Te_3 belongs to a trigonal crystal system. It is formed in a $R\bar{3}m$ space group. Layers of Bi and Te have an hexagonal order and the Bi_2Te_3 shows S_6 symmetry. The layers are stacked according to $-Te^{(1)} - Bi - Te^{(2)} - Bi - Te^{(1)}$ in quintets. Within the quintets the $Te^{(1)} - Bi$ and $Te^{(2)} - Bi$ bonds are of a mostly covalent nature with some ionic character. The bonds between the quintets are Van-der-Waals bonds. This difference can be seen in the distance between the layers ($Te^{(1)} - Bi$ = 1.74 Å and $Te^{(2)} - Bi$ = 2.04 Å vs. $Te^{(1)} - Te^{(1)}$ = 2.60 Å)[2,32]. The cell axes are $a_{lat} = b_{lat} \neq c_{lat}$ (a_{lat} = 4.384 Å, c_{lat} = 30.487 Å). The layers are stacked perpendicular to the large cell axis (c). Also $Bi_{(2-x)}Sb_xTe_3$ and $Bi_2Te_{(3-y)}Se_y$ show a rombohedral lattice system and the space group $R\bar{3}m$. All compounds are isostructural and both Bi atoms can be substituted by Sb atoms whereas Te atoms can be substituted by Se atoms.

The crystal structure[32], which is shown in Figure 1.3, is important with respect to the intercalation of contaminations into Bi_2Te_3. The diffusion of Cu into Bi_2Te_3 was investigated and found to be faster in the direction of the a axis and accounted for the weak van der Waals bondings between the $Te^{(1)} - Te^{(1)}$ bondings. It was found that the amount of Cu intercalation[53] could be as high as 3 mg·g^{-1}. Also other metals such as Ni were found to intercalate[23]. A careful investigation of the impurities is therefore necessary.

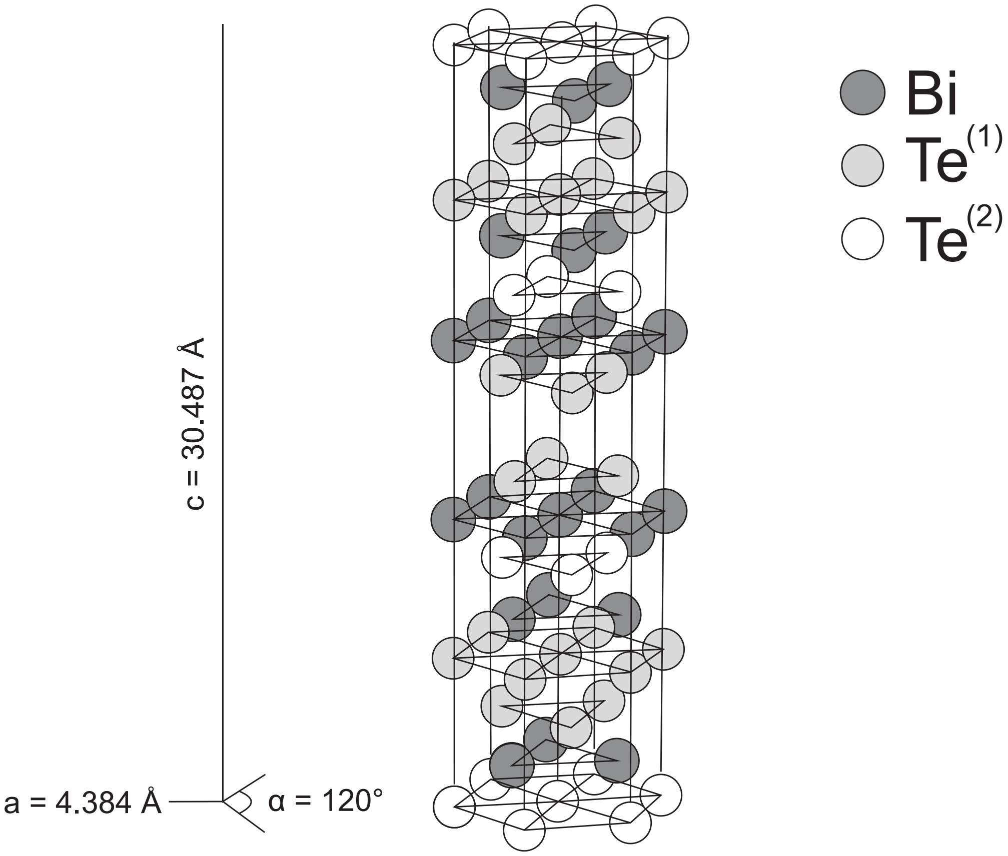

Figure 1.3: Layer structure of Bi_2Te_3. $R\overline{3}m$ space group and informations on the lattice constants.

1.3.3 Electrochemical deposition

In Figure 1.4 the set-up used for the electrochemical deposition of layers of thermoelectric materials on wafers, which was used within the frame of this project[5], is shown. In this system a Si wafer, which is coated with Au and Cr is placed under an opening at the bottom of a beaker made of Polytetrafluorethylene (PTFE), in which an electrolyte solution is stirred with a magnetic stirrer. To prevent leakages an O-ring is mounted between the beaker and the Si wafer. Under the wafer a Cu plate is mounted and a Ag contact paste is dispersed at the rim of the Si wafer to contact the top Au layer to the Cu plate. To the latter a potential is applied. The potential between the wafer and a Pt mesh as counter electrode is applied with reference to a third Ag/AgCl electrode with a potentiostat either pulsed or continuously. The deposition taking place depends on the applied potential and the ion concentration in the electrolyte solution.

The formation of Bi_2Te_3 was proposed to be a two-step mechanism, according to the Equations 1.3 and 1.4 and results in the sum reaction, which is given in Equation 1.5[54]. The formation of Sb_2Te_3 proceeds over several steps including the dissolution of Sb as SbO^+-tartaric acid complexes, which have to be used to overcome the relatively low solubility of Sb_2O_3 in HNO_3, and a possible co-deposition of elemental Sb and Te, as it is shown in Equations 1.6 to 1.8[55]. The sum reaction for the deposition of $Bi_{2-x}Sb_xTe_3$ can be formulated as given in Equation 1.9, but the mechanism is found to be strongly potential dependent[56]. The formation of $Bi_2Te_{3-y}Se_y$ was proposed to take place according to a similar two-step mechanism, as in the case of Bi_2Te_3. The sum reaction equation can be written as given in Equation 1.10[30].

$$HTeO_2^+ + 3H^+ + 4e^- \rightarrow Te + 2H_2O \qquad U^0 = 0.56\,V \tag{1.3}$$

$$3Te + 2Bi^{3+} + 6e^- \rightarrow Bi_2Te_3 \qquad U^0 = 0.45\,V \tag{1.4}$$

$$3HTeO_2^+ + 2Bi^{3+} + 18e^- + 9H^+ \rightarrow Bi_2Te_3 + 6H_2O \tag{1.5}$$

$$HTeO_2^+ + 3H^+ + 4e^- \rightarrow Te + 2H_2O \qquad U^0 = 0.56\,V \tag{1.6}$$

$$SbO^+ + 2H^+ + 3e^- \rightarrow Sb + H_2O \qquad U^0 = 0.21\,V \tag{1.7}$$

$$2SbO^+ + 3HTeO_2^+ + 13H^+ + 18e^- \rightarrow Sb_2Te_3 + 8H_2O \tag{1.8}$$

$$(2-x)\mathrm{Bi}^{3+} + x\mathrm{SbO}^{+} + 3\mathrm{HTeO}_2^{+} + (9+2x)\mathrm{H}^{+} + 18\mathrm{e}^{-} \rightarrow \mathrm{Bi}_{2-\mathrm{x}}\mathrm{Sb}_{\mathrm{x}}\mathrm{Te}_3 + (6+x)\mathrm{H}_2\mathrm{O} \tag{1.9}$$

$$2\mathrm{Bi}^{3+} + (3-y)\mathrm{HTeO}_2^{+} + y\mathrm{H}_2\mathrm{SeO}_3 + (9+y)\mathrm{H}^{+} + 18\mathrm{e}^{-} \rightarrow \mathrm{Bi}_2\mathrm{Te}_{3-\mathrm{y}}\mathrm{Se}_{\mathrm{y}} + (6+y)\mathrm{H}_2\mathrm{O} \tag{1.10}$$

For all reactions the mechanisms possibly contain two or more steps and every step strongly depends on the applied potential, as it can be seen from the standard potentials given for the reactions 1.3, 1.4, 1.6 and 1.7. Furthermore through the Nernst equation (Equation 1.11) they depend on the pH and on the ion concentrations.

$$U = U^0 + \frac{RT}{zF} ln \frac{c_{Ox}}{c_{Red}} \tag{1.11}$$

U it the electrode potential, U^0 is the standard electrode potential, R is the gas constant, T = temperature, z is the number of electrons exchanged (charge), F is the Faraday constant and c_{Ox} and c_{Red} are the concentrations of the reactants.

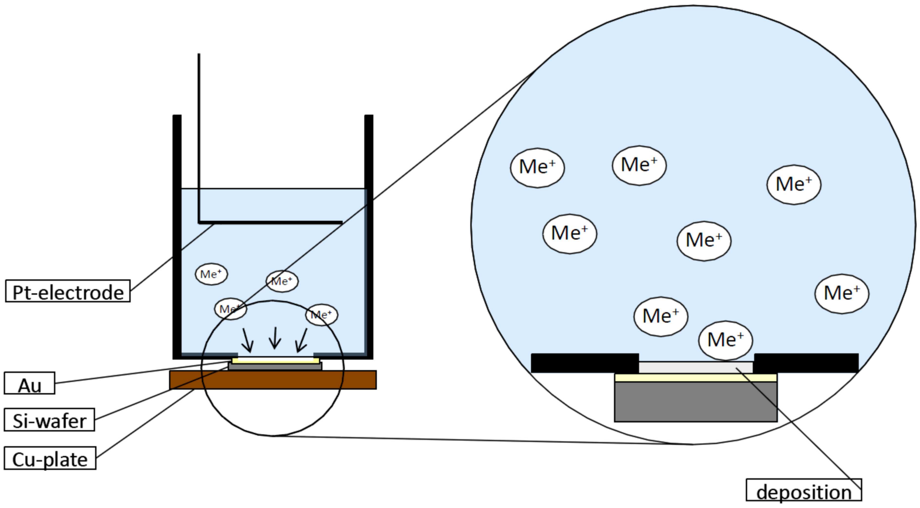

Figure 1.4: Set-up for electrochemical deposition.

A typical sample for chemical analysis is shown in Figure 1.5. To perform several measurements of chemical and physical properties typically the sample is cut in four pieces.

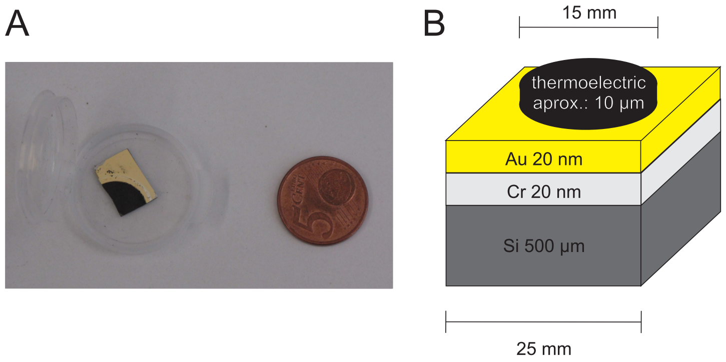

Figure 1.5: Photograph of a typical sample (A) and drawing (not to scale) (B). Samples are cut into four pieces so as to enable a chemical and a physical characterization from one deposition experiment.

2 Analytical methods

2.1 Atomic emission spectrometry

In optical emission spectrometry the transitions of valence electrons between discrete energy levels of an atom are used. According to Bohr's theory of the atomic structure the electrons in the atom can be at different discrete energy levels. As soon as the electron changes the energy level from a higher state to a lower state energy is emitted in the form of electromagnetic radiation. To promote an electron to a higher state energy has to be transferred to the atom. One of the possible ways for energy transfer is the absorption of electromagnetic radiation. According to Planck's law the wavelength of the radiation is proportional to the energy difference between the two energy levels involved[36].

$$\Delta E = h\nu = h\frac{c_{light}}{\lambda} \tag{2.1}$$

Here E is the energy, h is the Planck constant, ν is the frequency of the radiation, c_{light} is the velocity of light and λ is the wavelength.

Consequently, the emission wavelength gives a qualitative information on the atoms, which emit the radiation. Since according to the Pauli rule no electron can have the same energetic state as another electron of the same atom, many transitions are possible and the atomic spectra are line-rich. Quantitative information can be derived from the line intensity, which is proportional to the number density of the emitting atoms and the involved energy level. As emitting species neutral atoms and ions have to be considered.

The ICP-OES

In inductively coupled plasma optical emission spectrometry (ICP-OES), an electrodeless discharge in argon at atmospheric pressure is used as radiation source. An ICP optical emission spectrometer consists of several parts, namely a sample introduction system, the ICP and a spectrometric system to disperse and detect the radiation emitted.

Nebulization system

For analyses by ICP-OES mostly but not only samples dissolved in aqueous solutions are used. From liquid samples aerosols are generated by means of a nebulizer. In many cases pneumatic nebulization can be utilized. Several types of pneumatic nebulization systems are commercially available and routinely used. They are given in Figure 2.1 The most common nebulizer is a concentric nebulizer consisting of two quartz tubes being a smaller inner tube for the liquid and an outer tube for the gas. At the nebulizer tip the diameter of the quartz tubes is decreased to increase the velocity of the fluent. The gas catches up the liquid and disperses it into small droplets, with a certain size distribution. A further nebulizer is the cross-flow nebulizer, where liquid and solvent flow are brought together in a rectangular way. Again the gas catches up the fluid and disperses it. A modification of that principle is the so-called modified Lichte nebulizer. Here the liquid is pumped into a groove through which it runs off. A gas flow coming under an angle of 90° to the groove interacts with the liquid. To enhance the dispersion a glass ball is provided in front of the opening of the gas tube, so that the droplets hit the glass ball and are further broken up. To separate smaller droplets form larger ones the nebulizer is positioned in a spray chamber[36]. The chamber is built so that only smaller droplets can pass together with the gas flow through the chamber. Larger droplets will hit the wall and will be removed from the aerosol so that they cannot cause liquid depositions in the the connection to the radiation source. The droplet cut-off radius depends on the combination of nebulizer and spray chamber and for a double pass Scott type spray chamber is of the order of 10 µm to 20 µm[57]. Droplets of which the size exceeds 10 µm were found not to evaporate completely in the plasma and therefore they should be avoided in analytical work[58]. For a combination of a spray chamber and a nebulizer, which produces an aerosol with a large fraction of droplets smaller than the diameter mentioned the line intensities are increased[59]. A second function of the spray chamber is to provide for a compensation for fluctuations in the liquid flow, which are induced by the peristaltic pump transporting the sample liquid to the nebulizer[36].

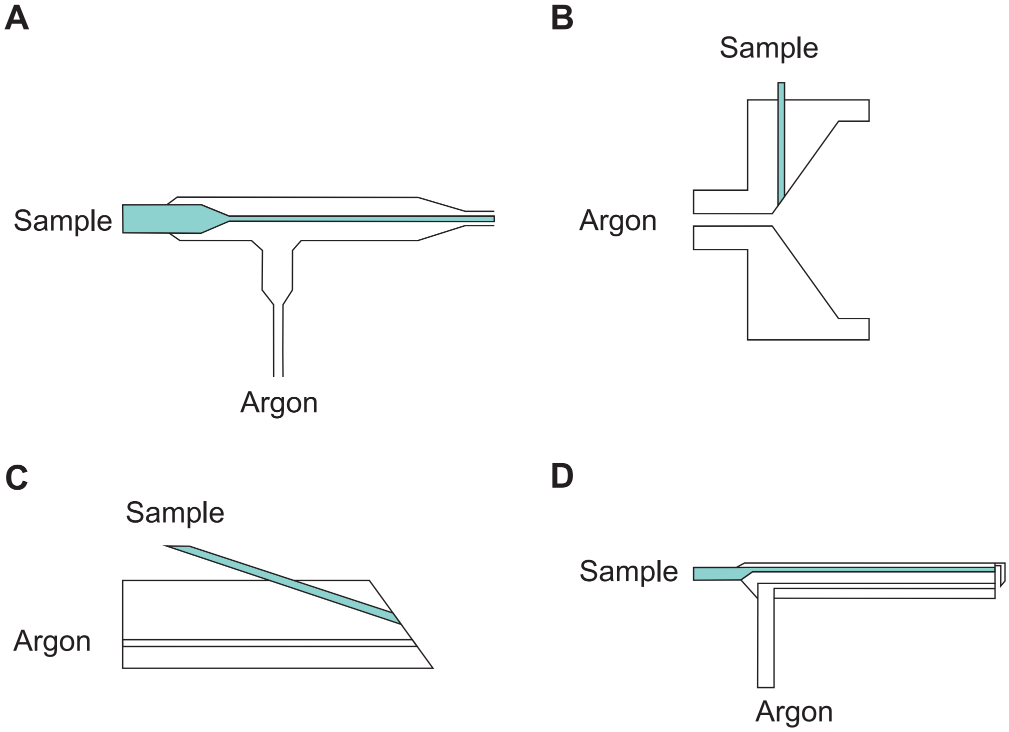

Figure 2.1: Concentric (A), Cross flow (B), Babington (C), Modified Lichte (D) nebulizers for ICP-OES.

Inductively coupled plasma

Based on the findings of Reed[60], Greenfield[61] and Fassel[62] plasma torches for analytical purposes were developed. In the case of a Fassel type torch a ring shaped toroidal plasma is formed[36]. From the spray chamber the aerosol is transported into the inner quartz tube of the plasma torch, which consists of three concentric quartz tubes. Through the outer tube the working gas is transported in a toroidal way by feeding it tangentially to it. A high gas flow (10 to 15 $\mathrm{L \cdot min^{-1}}$) is necessary to cool the outer quartz tubing so as to prevent it from melting. Through the middle quartz tube an auxiliary gas flow is led to push the plasma away from the middle and inner quartz tube to prevent them from melting, and also so as to avoid

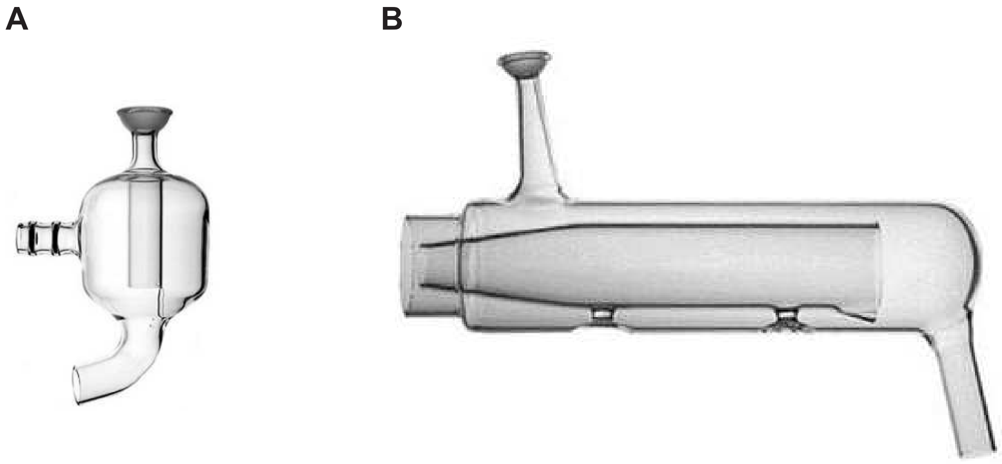

Figure 2.2: cyclonic spray chamber (A), Scott type double pass spray chamber(B) for ICP-OES.

salt or carbon deposition from liquids with high salt or organic matter loads. Through the middle quartz tube the sample aerosol is brought into the ICP.

Around the outer quartz tube a HF induction coil is mounted to feed energy to the plasma. The latter is ignited by a Tesla spark. This spark ionizes Ar atoms and the resulting electrons are accelerated by the magnetic field inside a hf-coil. By collisions these electrons ionize further Ar atoms and the plasma can be sustained[63].

The inductively coupled plasma is a special type of electrical discharge in which the gas is partially ionized. Partially ionized gases are usually denoted as plasmas. Non-radiative and radiative processes are responsible for the transfer of energy inside a plasma, so that molecules, atoms, ions, radicals and electrons can co-exist in a plasma. The energy transfer processes include collisions, emission, absorption and fluorescence of radiation[36]. The ICP is a very efficient excitation and ionization source. The excitation and de-excitation processes in a Ar plasma, which apply for Ar as well as for analyte atoms (M), are listed in Table 2.1.

Ar^m is a so-called metastable level (E=11.7 eV, the ionization energy of Ar is E_I=15.7 eV) and * denotes the excited levels.

The plasma temperatures for a typical ICP source depend on the region in the plasma (compare Figure 2.3). The analyte atoms travel through a central channel in the plasma and experience temperatures between 8000 K and 5500 K[64], or slightly lower values, depending

Table 2.1: Excitation and de-excitation mechanisms in an Ar-plasma[36].

electron impact	$Ar + e^-$	$\rightarrow$	Ar^*, Ar^m
	$M + e^-$	$\rightarrow$	M^*, M^{+*}
radiative recombination	$M^+ + e^-$	$\rightarrow$	$M + h\nu$
radiation trapping	$Ar + h\nu$	$\rightarrow$	Ar^+
charge transfer	$Ar^+ + M$	$\rightarrow$	$M^{+*} + Ar$
Penning effect	$Ar^m + M$	$\rightarrow$	$M^+ + Ar$

on the thermometer species selected[65]. In well defined zones a number of processes, such as aerosol drying, sample atomization, excitation of the atoms and ionization of the atoms occur[36]. In the coldest zone of the plasma self-reversal of spectral lines can occur and hereby the linear dynamic range in atomic emission spectrometric analysis is reduced. A shear gas flow[66] or a counter gas flow[67] can be used to push the coldest parts of the plasma aside from the optical path.

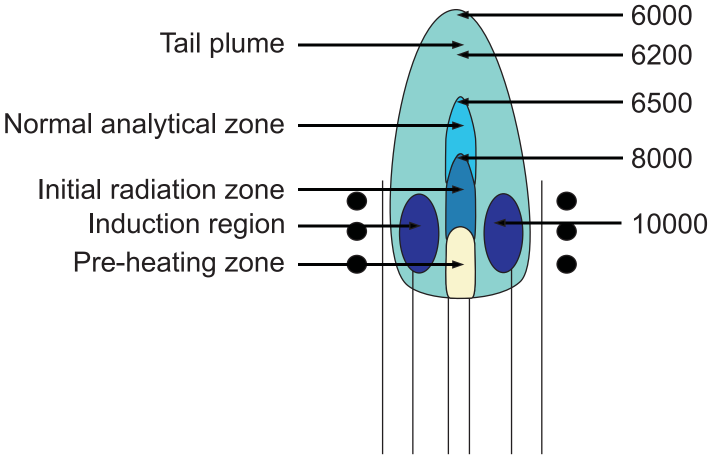

Figure 2.3: A: Temperature zones in an ICP[66].

Spectrometers

The emitted radiation from the plasma is spectrally dispersed by a spectrometer. Commonly used spectrometer types are the Czerny-Turner monochromator, in which the radiation is directed through an entrance slit to a collimating mirror. From here it is reflected to a grating. The dispersed radiation is then focused by a second mirror to the exit slit, behind which a detector is mounted. The spectral lines have to be measured sequentially because only a part of the spectrum is reflected by the second mirror to the exit slit.

In a Paschen-Runge mounting the radiation is focused on an entrance slit and directed to a holographic grating. This focuses the dispersed radiation on the so-called Rowland circle, in which CCD (Charge Coupled Device) detectors are mounted so as to simultaneously measure a high number of spectral lines in the complete spectrum.

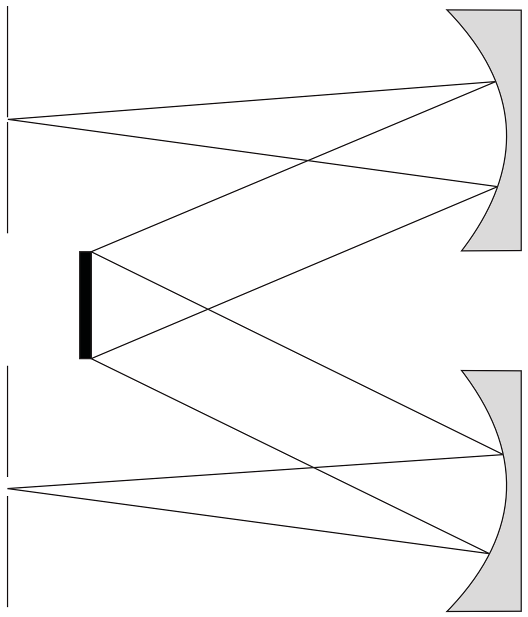

Figure 2.4: Czerny-Turner monochromator.

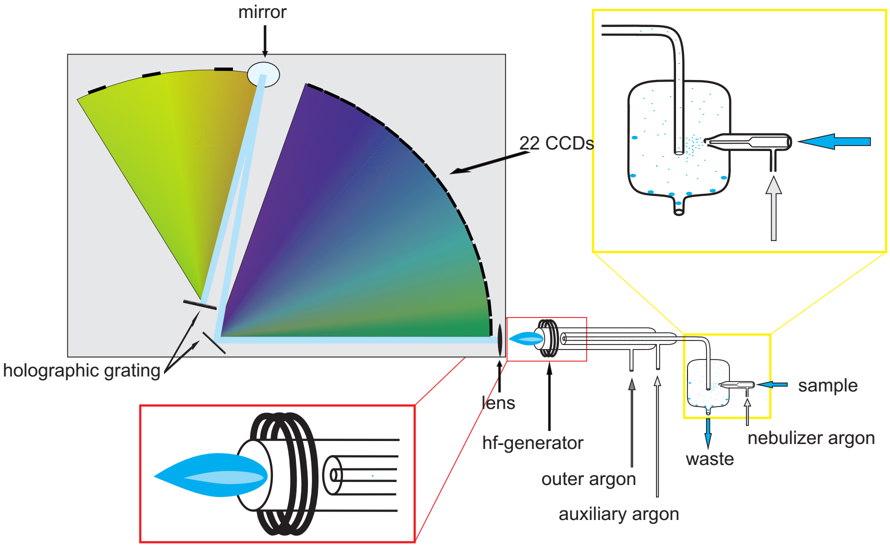

Figure 2.5: Inductively coupled optical emission spectrometer (ICP-OES), Spectro Ciros CCD. The aerosol is produced by a modified Lichte nebulizer with cyclone spray chamber (yellow). The radiation from the plasma torch (red) is led into a Paschen-Runge spectrometer equipped with 22 CCDs.

2.2 Depth-profiling with atomic spectrometry

2.2.1 Glow discharge sources

Glow discharges (GD) are traditionally defined as delocalized electrical discharges with a high burning voltage and low current density. Thy can be operated at reduced as well as at atmospheric pressure in an inert atmosphere and are gaseous electrical conductors. A glow discharge is one of many forms of gaseous discharges, which are often called plasmas. It is operated between two distinct electrodes in a gaseous medium, through which an electrical current is passed. The cathode has the negative potential and the anode has the positive potential formally. In reality the discharge is formed by potential differences between the electrodes and the designation of the cathode and anode is based only on the difference[38].

The glow discharge at reduced pressure is typically operated at 0.1 mbar to 10 mbar in an inert gas atmosphere (typically Ar) at powers below 100 W and voltages between 250-2000 V. Currents up to 0.1 A flow in a discharge. Glow discharges can exist at atmospheric pressures when a large resistor is placed electrically in series with the discharge. A first analytical application of such a device with a liquid as the cathode was realized by Cserfalvi et al.[68].

When the discharge current is increased in a glow discharge it finally turns over into a direct current arc, which is characterized by a large current of 10-1000 A. Here the cathode heats up and evaporates[38].

In a glow discharge the potential difference between the electrodes causes a breakdown of the discharge gas to form positively charged ions and free electrons, which are accelerated to the cathode (-) and the anode (+), respectively. The impact of the positive ions on the cathode transfers momentum to the surface, which initiates a so-called the sputtering process. In this way direct solids sampling and depth resolved analysis can be performed[38].

In comparison with high vacuum sputtering techniques such as secondary ion mass spectrometry (SIMS) the GD source has higher current densities (100 mA cm^{-2} vs. 1 μ A cm^{-2}) and far lower average kinetic energies ($<$100 eV vs. $>$1 keV). Therefore the sample ablation rates are in glow discharges much higher than in SIMS, but with far less lattice damage for the GD source[38].

In a direct current (dc) glow discharge atoms are ionized and impact on the cathode with high energy. By this the sample is ablated in a purely mechanical way (cathodic sputtering), or the cathode can be heated and start to evaporate (thermal volatilization). The ablation rate in an analytical glow discharge may be in the range of some milligrams per minute. The sputtered material can be partially ionized. This ionization contributes only for a small part (some percent) to the total glow discharge current. An analytical glow discharge with the sample as flat cathode was first described by Grimm[69]. In the source the cathode is cooled and the sample is ablated by sputtering only. Owing to the discharge form the ablation takes place layer by layer. The form of the burning crater formed, however is dependent on the field distribution[38].

Apart from dc also rediofrequency (rf) glow discharges found entrance in atomic spectrometry. In an rf discharge the field is applied through an antenna and in many cases through the cathode, when the sample is solid and is to be ablated. Frequencies in the low megahertz range are used so that electrons can easily follow the field but not the ions which have a higher mass. Accordingly, a bias potential on the sample is built up and the ions are accelerated towards the sample as a result of the induced field[38]. A major difference between dc and rf discharges is the applicability of the latter to the analysis of electrically non-conducting samples. When a dc potential is applied to a nonconducting sample a positive charge will build up on the surface, because no charge movement within the sample is possible. The presence of a positive charge on the sample surface counterweights the applied potential and stops the current flow in the discharge. The process is analogue to the charging of a capacitor. Thus a nonconducting sample cannot sustain a dc glow discharge and is not a viable sample for dc glow discharge analysis[38].

Three ways to circumvent the insufficient conductivity of samples are possible. The first one is to make the sample conductive by grinding it and mixing it with a conductive powder. This removes the possibility for depth-profile analysis. The second one is to place a conductive layer of metal on the sample surface, which is ablated by the discharge and sputtered onto the sample, so that the sample surface then is conductive due to the deposited metal layer. This process is difficult to optimize and not very straight forward. The third one is to use a rf field. Here the sample does not have to be changed or manipulated in any way. A negative potential builds up on the sample surface due to the rf field. It can be explained with the reaction and movement of electrons and Ar ions in the electric field. Due to the field Ar^+ ions are accelerated towards the sample surface. with a velocity v.

$$v = \sqrt{\frac{2eU}{m}} \tag{2.2}$$

eV is the product of the electrical charge e, U is the potential difference and m is the mass of the charge carrier.

This theoretically possible velocity is not achieved due to elastic collisions of Ar^+ and e^-. The Ar^+ ions kinetic energy is further reduced by charge transfer reactions of Ar^+ ions by collisions with Ar atoms. This process produces new Ar^+ ions, which are not subjected to the full electric field. Accordingly, the velocity of the Ar^+ ions during the negative portion of the rf half cycle is lower than the velocity of the e^- during the positive rf half cycle. As a result more negative charge is accumulated on the cathode surface and a net negative charge will offset the potential towards a negative bias potential. As a result of this effect a negative potential exists during approximately 90% of the rf cycle and the heavy Ar^+ ions are accelerated towards the cathode.

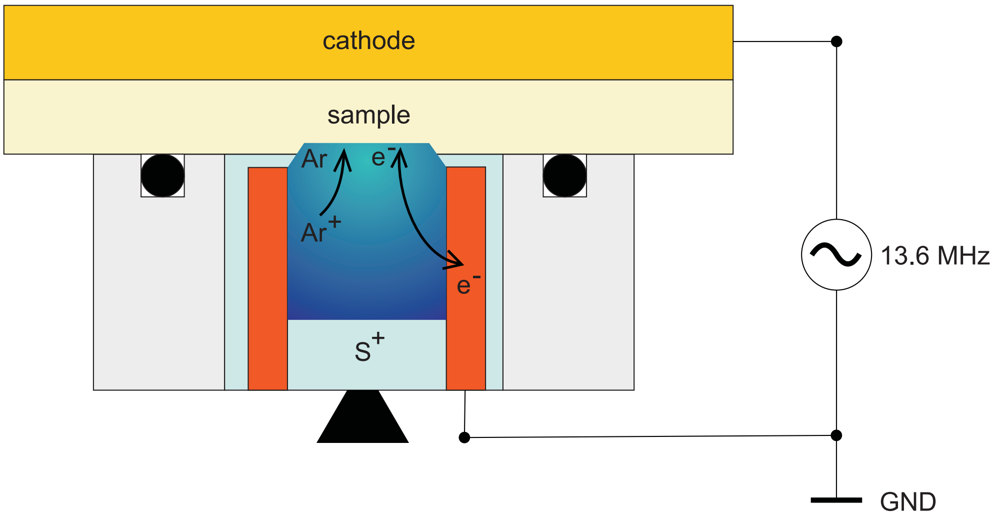

Figure 2.6: Principle of an rf glow discharge.

2.2.2 Time-of-flight mass spectrometry

Several different types of MS are frequently used in analytical chemistry. They differ with respect to mass separation and have their advantages. The quadrupole based MS is known as a cheap instrument, which suits the needs for most analyses. The detection of several elements is a rapid sequential one and therefore the time consumption is higher than with to other MS techniques. The time-of-fight MS enables the detection of fast transient signals over the full mass spectrum from ^{7}Li to ^{238}U with detection frequencies in the kHz range. Highly resolved mass spectra can be obtained with double focusing MS machines in Nier-Johnson geometry[70]. These machines detect like a quadrupole MS in a sequential manner. Truly simultaneous detection is enabled by a Mattauch-Herzog geometry with a large semiconductor detector[71].

In time-of-flight mass spectrometry the ions are extracted as a package by a short and well-defined voltage impulse of 4 to 35 kV orthogonally to or in the direction of their flight direction, to accelerate them. Further, they enter a field free flight distance of 0.1 to 4 m. The flight time ions need to reach the detector depends on the ion mass according to Equation 2.3 and ranges between 1 to 100 μs[63].

$$\frac{m}{z} = \frac{2Ut^2}{d^2} \tag{2.3}$$

m is the ion mass, d is the flight distance, t is the time of flight, U is the accelerating voltage and z is the ion charge.

It can be seen that light ions have a shorter flying time than heavier ions and the mass is proportional to the square of the time of flight.

On the flight path the ions are focused by ion lenses and can even be reflected by applying an electrical counter field. The reflection enables it to make the instrument smaller compared to an instrument without reflector and more importantly it increases the mass resolving power. The mass resolution depends on the initial kinetic energy distribution of the ions. An ion focusing according to mass is realized because faster ions need a longer flight distance within the reflector lenses of the spectrometer, which is proportional to their velocity excess. The mass resolving power is given according to Equation 2.4

$$\frac{\overline{m}}{\Delta m} = \frac{t}{2\Delta t} = \frac{s}{2\Delta s} \tag{2.4}$$

Here $\overline{m}$ is the mean value of the masses, which have to be resolved. Δm is the mass difference, which has to be resolved at a certain mass.

Typical mass resolving powers of commercial instruments are in the range of 3000 to 5000. The mass resolution power is mass depended and increases with increasing mass[63].

In connection with a glow discharge source a set-up, as shown in Figure 2.7 can be used.

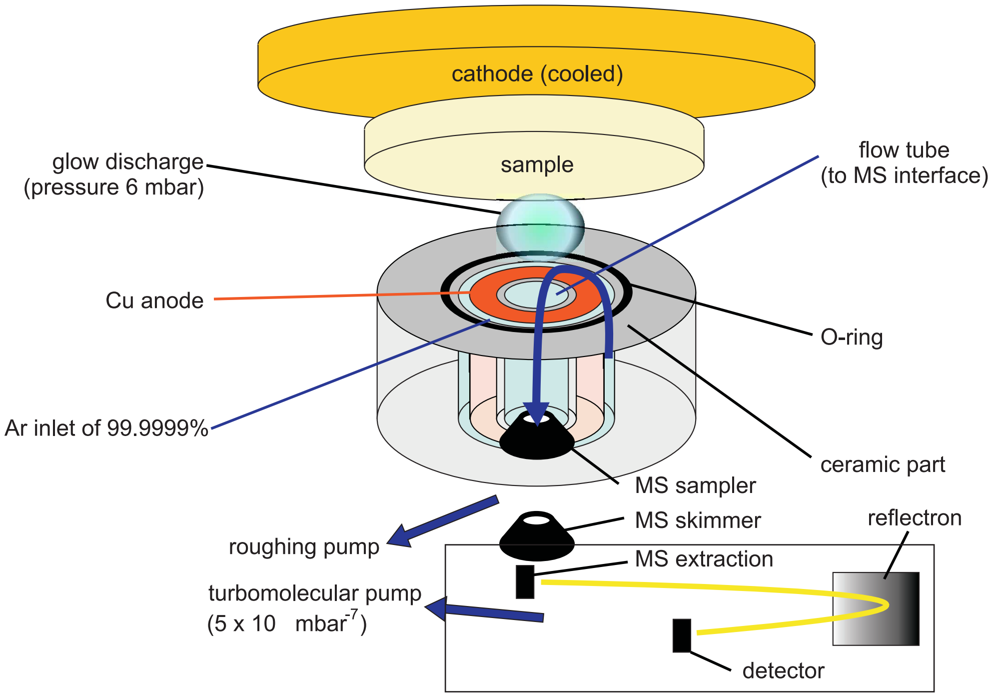

Figure 2.7: Set-up for glow discharge time-of-flight mass spectrometry (GD-TOF-MS).

2.3 X-ray fluorescence

Electromagnetic radiation between wavelengths of 0.02 nm and 2 nm (60 keV and 0.6 keV) is called X-ray radiation[63].

X-Ray sources

On a laboratory scale X-ray radiation can be generated with the aid of an X-ray tube. The tube is evacuated and contains a cathode and an anode made of a heavy element, typically Mo or W, which is called the target. The cathode is a heated metal wire, which emits electrons. The electrons are accelerated towards the anode as the result of a high voltage applied between the two electrodes. As a result of the electron bombardment the target material is excited and emits its element-characteristic X-ray radiation. Additionally, “Bremsstrahlung” is emitted by the electrons[63].

X-ray radiation can also be generated under the use of a synchrotron facility or a free electron laser (FEL)[63]. In both systems electrons are accelerated and their flight path is bent through the action of magnetic fields. Due to the bending a continuous “Bremsstrahlung” is emitted tangentially to the direction of movement of the electrons. Synchrotron radiation spreads out over the whole electromagnetic spectrum and has a high intensity emission. It is coherent radiation, which is highly brilliant.

Monocrhomators

To achieve a monochromatic emission with the aid of an X-ray tube is often obtained with a multilayer consisting of layers of heavy elements and their compounds[72]. Due to the periodic multilayer structure only a monochromatic radiation is reflected according to Bragg’s law (Equation 2.7), which also applies in XRD (compare Section 2.4). With the aid of crystals with known atom layer distances also synchrotron radiation can be spectrally resolved according to Bragg’s law.

X-ray fluorescence

X-ray radiation can penetrate through material but its intensity is weakened by interactions of the X-ray radiation with the material. The absorption can be described by the equation

$$I = I_0 \cdot e^{-\mu d} \tag{2.5}$$

I is the intensity of the radiation after its passing through the material, I_0 is the radiation intensity before the transition through the material, d is the thickness of the material and μ is the absorption coefficient of the material.

The radiation interacts with the electrons of the material atoms. Three types of interaction are to be considered. The photoelectric effect, where the X-rays being photons with the energy $h\nu$, remove an electron of the atom shell. This is possible when the energy of the incoming radiation is larger than the binding energy of the electrons. The rest energy of the photon in this case is transfered to the electron in the form of kinetic energy according to.

$$h\nu = E_{binding} + E_{kinetic} \tag{2.6}$$

Another type of interaction is the Compton effect. Here the X-ray photons give a part of their energy to an electron, without ejecting it from the atom. The energy of the electrons is converted to heat while the X-ray wavelength is increased and the direction of the radiation is changed. This process is known as incoherent scattering and it can be compared to an inelastic collision. When only the direction is changed, whereas the energy of the radiation is not changed, no energy is transferred to the electron and one speaks of coherent Rayleigh-scattering. This third effect can be compared to an elastic collision. The absorption coefficient μ comprises parts due to photoelectric absorption, incoherent Compton scattering and coherent Rayleigh scattering. The total absorption coefficient μ decreases in general with the energy of the radiation and shows sharp edges at energies, which equal the binding energy of an electron. Here the photoelectric effect is the reason for absorption. Subsequent to a photoionization, where an inner electron is ejected from the atom, an electron from a higher electron shell can replace the missing electron. As a result of this energy transition an X-ray quantum is emitted, of which the wavelength equals the energy difference between the two energy states. This process is called X-ray fluorescence. The energy difference can also be transfered to an other electron of an outer shell, which than is ejected from the atom as an Auger electron[63].

According to IUPAC recommendations the fluorescence lines are named according to the electron shell to which the transition occurs (K, L or M). A second index indicates from where the electron stems[73]. The types of transitions and the selection rules are resumed in Figure 2.8.

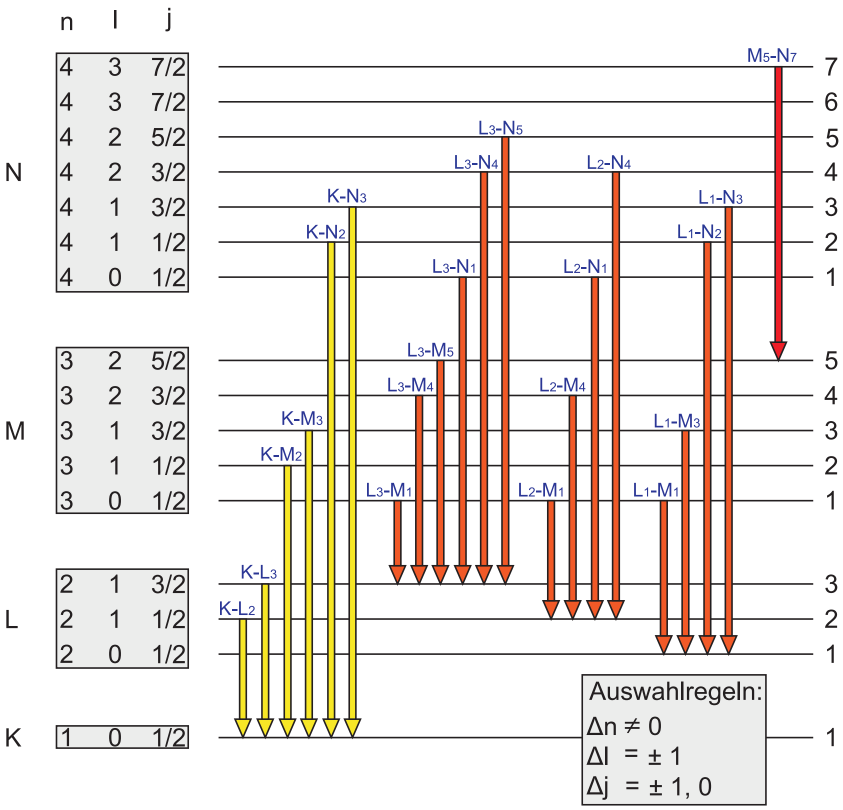

Figure 2.8: Transitions and selection rules in XRF[74].

2.3.1 Total reflection X-ray fluorescence

In total reflection X-ray fluorescence (TXRF) the exciting X-ray beam is directed under grazing incidence conditions onto a flat sample carrier. As sample carriers typically quartz or acryl glass carriers are used but also Si wafers are smooth enough for total reflection work. As a result of the total reflection conditions the beam does not penetrate into the carrier, by which the Rayleigh and Compton scattering is kept low. Secondary absorption effects within the sample can also be avoided, when very thin layers of sample are used.

Accordingly, matrix effects are reduced and low absolute detection limits as compared to conventional XRF can be achieved[63]. In Figure 2.9 the excitation of a sample under total reflection conditions is shown.

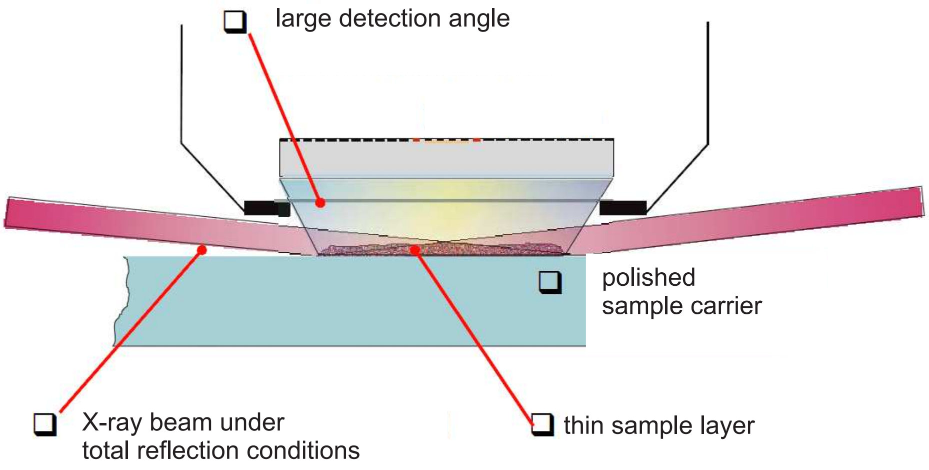

Figure 2.9: Total reflection X-ray fluorescence[72].

Silicon Drift Detector for XRF

The silicon drift detector (SDD) consists of n-doped Si crystal. On top of the Si crystal a collecting anode in the form of a ring is provided. A negative voltage with respect to the anode is applied to the Si block. On the top p-doped ring shaped strips and on the back a p-doped contact are present. The negative voltage is applied to the back contact and to the ring electrodes on top. The voltage difference with respect to the anode increases to the outermost ring electrode so that the potential energy for electrons falls diagonally to the anode. Each electron, which is generated inside the detector will therefore drift to the anode[75].

2.3.2 Extended X-ray absorption fine structure and X-ray absorption near edge structure principles

Interactions of the ejected electron with the electron shells of surrounding atoms can be seen in so-called extended X-ray absorption fine structure (EXAFS) scans. The ejected electron, which can be considered as a wave with a wavelength depending on E_{kin}, is scattered by the neighboring atoms. Positive or negative interferences occur as a result of the scattering at the absorbing atom. When the energy of the X-ray beam is changed around the absorption edge the kinetic energy of the ejected electron changes accordingly, and oscillations in the spectrum can be observed. The energy range between 50 eV below the absorption edge to 50 eV above the absorption edge informs in XANES. It can be divided in the pre-edge region, where transitions to an unoccupied level of the atom can be seen, and the post-edge region, where multiple scattering processes of the emitted electron and the absorbing atom can be observed. In the EXAFS regions higher energy oscillations between the emitting atom and its direct neighbors can be found. The shorter the distance to the neighbors the higher is the energy, at which the first oscillation will occur. With the first oscillation the absorption edge will shift to higher energies when a highly oxidized central atom is excited[76]. In Figure 2.10 the different processes, and energy regions around an absorption edge, which are relevant for XANES and EXAFS are shown.

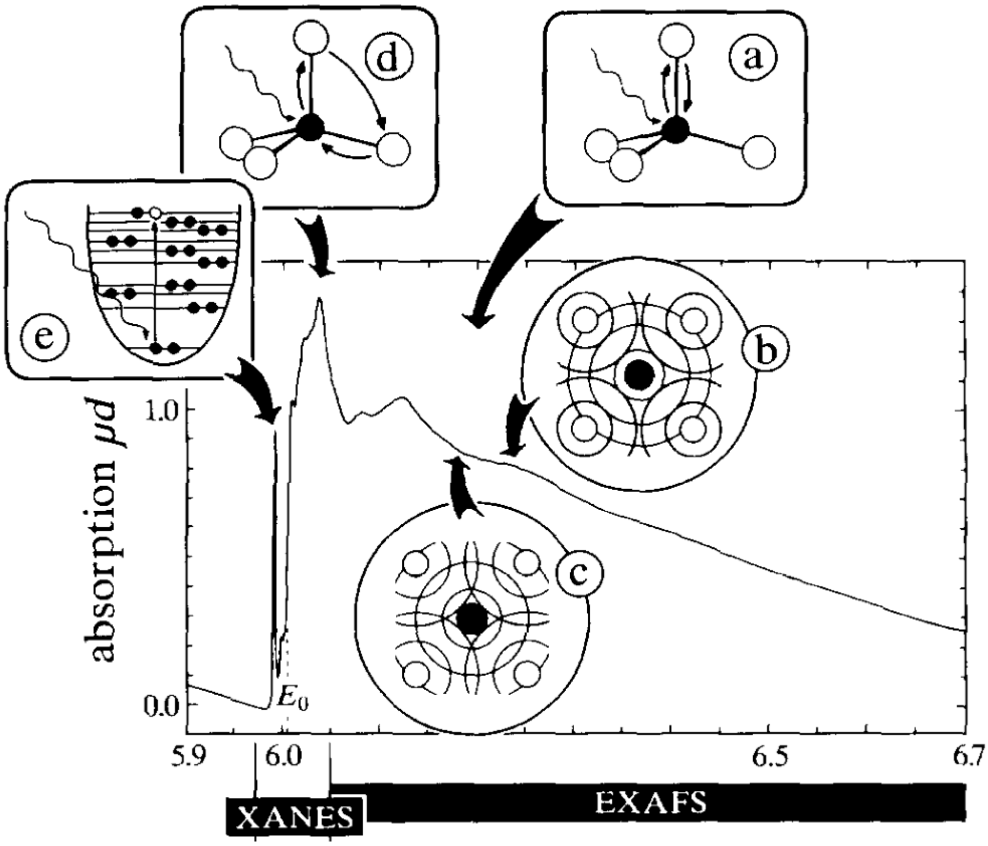

Figure 2.10: Cr K edge X-ray absorption spectrum of K_2CrO_4. The physical processes yielding to the different features of an X-ray absorption spectrum are given and the XANES and EXAFS regions are indicated. A scattering process of the ejected electron with one neighbor (A) and (B), a scattering process of the ejected electron with more than one neighbor (C) and (D), a pre-edge transition of an electron to the lowest unoccupied energy level (E)[76].

2.4 Structural characterization with X-ray powder diffraction

X-ray powder diffraction is a routinely used method to investigate the crystal structures of solid materials. The form of the diffraction pattern is based on the Bragg equation (2.7) Here it is expressed that an X-ray beam is reflected at a crystal plane as a function of the lattice plane distance (d), the incidence angle (θ) and the X-ray wavelength (λ).

$$2d\sin\theta = n\lambda \tag{2.7}$$

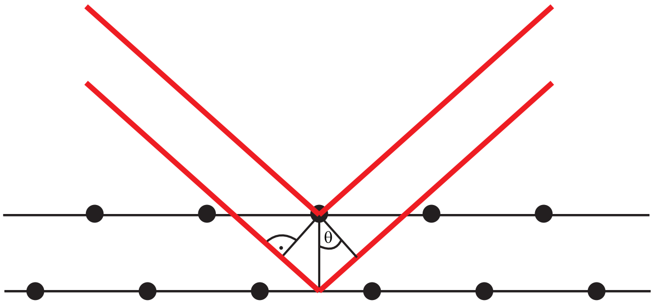

Figure 2.11: Reflection of X-rays according to Bragg.

Reflections occur at different layers and interferences of the reflected beams appear. In dependence of the lattice plane distance positive interferences will occur between parallel layers, when the Bragg conditions apply. For measurements in the Bragg-Brentano geometry an X-ray tube and a detector are moved around the sample over an angle θ so that reflexes at 2θ are detected. The reflexes are indexed in this work according to database entries.

The cell constants a_{lat} and c_{lat} for a rombohedral lattice system (compare Section 1.3.2) can be calculated form the reflex positions after reflex indexing according to Equation 2.8.

$$\frac{1}{d^2} = \frac{4}{3}\left(\frac{h^2+hk+k^2}{a_{lat}^2}\right) + \left(\frac{l^2}{c_{lat}^2}\right) \tag{2.8}$$

Here h, k and l are the Miller indices, a_{lat} and c_{lat} are the cell constants and d is the lattice plane distance, which is calculated from the Bragg's law (Equation 2.7). The angle θ is known from the diffractogram, the wavelength λ in the case of a Cu anode containing X-ray tube as radiation source is 1.54 Å and n is an integer number

Furthermore, the Debeye-Scherrer equation (2.9) enables it to calculate of the crystallite size D from the full width at half maximum ($FWHM$) of a reflex in the diffractogram.

$$FWHM = 0.9\frac{\lambda}{D\cos\theta} \tag{2.9}$$

2.5 Potential Seebeck microprobe

The Seebeck coefficients were determined with the aid of a potential Seebeck microprobe (PSM) system (Panco GmbH, Mühlheim, Germany[46]). The set-up is shown in Figure 2.12.

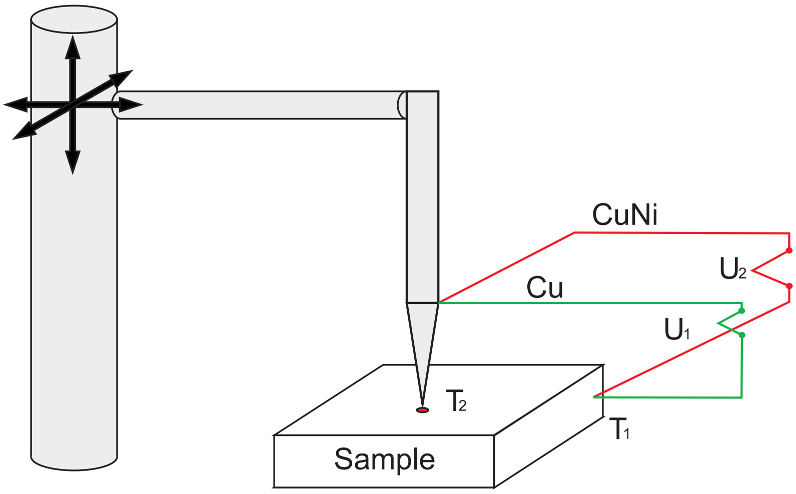

Figure 2.12: Set-up of the Seebeck microprobe[46].

The sample is heated through the probe tip and a temperature gradient is induced in the sample. With two thermocouples the temperatures T_1 and T_2 are measured. The corrected Seebeck coefficient for the sample can be determined[5] as reflected by Equation 2.12:

$$U_1 = (T_2 - T_1) \cdot \left(S_{Sample} - S_{Cu}\right) \tag{2.10}$$

$$U_2 = (T_2 - T_1) \cdot \left(S_{Sample} - S_{\mathrm{CuNi}}\right) \tag{2.11}$$

$$S_{Sample} = \frac{U_1}{U_2 - U_1} \cdot (S_{Cu} - S_{\mathrm{CuNi}}) + S_{Cu} \tag{2.12}$$

2.6 Atomic absorption spectrometry

The first analytical use of atomic absorption spectrometry (AAS) dates back to 1955, when Alan Walsh described the application of atomic absorption spectra to chemical analysis[77]. In AAS primary radiation source is used to emit element specific radiation. The primary resonant radiation is absorbed by analyte atoms, which are contained in an atom reservoir and atomized. This absorption is highly element-selective. Several ways of producing the primary radiation are known. Line sources such as hollow cathode lamps (HCL) and electrodeless discharge lamps (EDL) but also a continuum radiation source can be used[36].

Line sources should emit an element specific line spectrum with line widths smaller than the widths of the absorption lines of the atoms in the atom reservoir. In common atom reservoirs the line width of an atomic spectral lines are of the order of 1-5 pm. Narrower spectral lines can be found in the case of discharges under reduced pressure. The resolving power of common optical spectrometers in the case of line sources is not high enough. Commonly used spectrometers in Czerny-Turner or Ebert geometry (compare Section 2.1), indeed also only allow it to achieve a spectral bandpass of 0.1 nm at the best. Continuum sources emit a spectrum over several hundred nm. Therefore, a high spectral resolving power ($R = \frac{\lambda}{\Delta\lambda}$) of at least of the order of 500000 for a 2 pm line at $\lambda = 400\,\text{nm}$ is needed. Here spectrometers with Echelle grating can be used successfully[36].

High resolution continuum source graphite furnace atomic absorption spectrometry (HR-CS GF AAS) has recently been made commercially available[78]. The set-up of a such instrument (ContrAA700, Analytik Jena, Jena, Germany) is shown in Figure 2.13. The spectrometer has been developed at ISAS (Dortmund, Germany) by Heitmann et al.[79] and was first used to correct for spectral interferences, which could not be resolved with the Zeeman background correction. With some modifications[80] the presently commercially available system is now working as described below.

The spectrometer contains of a double Echelle monochromator (DEMON) with a grating and a prism in a Littrow arrangement. The double monochromator, consisting of a 300-mm prism predisperser and a 400-mm Echelle monochromator offers a high resolving power of $\lambda/\Delta\lambda = 110000$ and covers the complete spectral region of analytical interest from 190 nm to 850 nm. It requires an active wavelength stabilization, which was accomplished via an internal neon lamp, with patented design, that provides for a wavelength correction with a precision better than $< 0.3 pm/pixel$[78,80,81].

As primary radiation source a high-pressure Xe short-arc lamp is operated in a so-called "hot-spot" mode is used, which emits an intense radiation especially in the UV region. Position fluctuations of the hot-spot are compensated for with the aid of a two-axis piezoelectric mirror drive[80].

A linear CCD array with 512 pixels is used as detector. Only a few pixels are used to measure the atomic absorption signal. The rest of the pixels can be used to correct for all spectral events that occur simultaneously on all pixels, such as lamp flicker noise and changes in the transmission of the atomizer which are independent of wavelength. This kind of correction was referred to as simultaneous double beam correction[81].

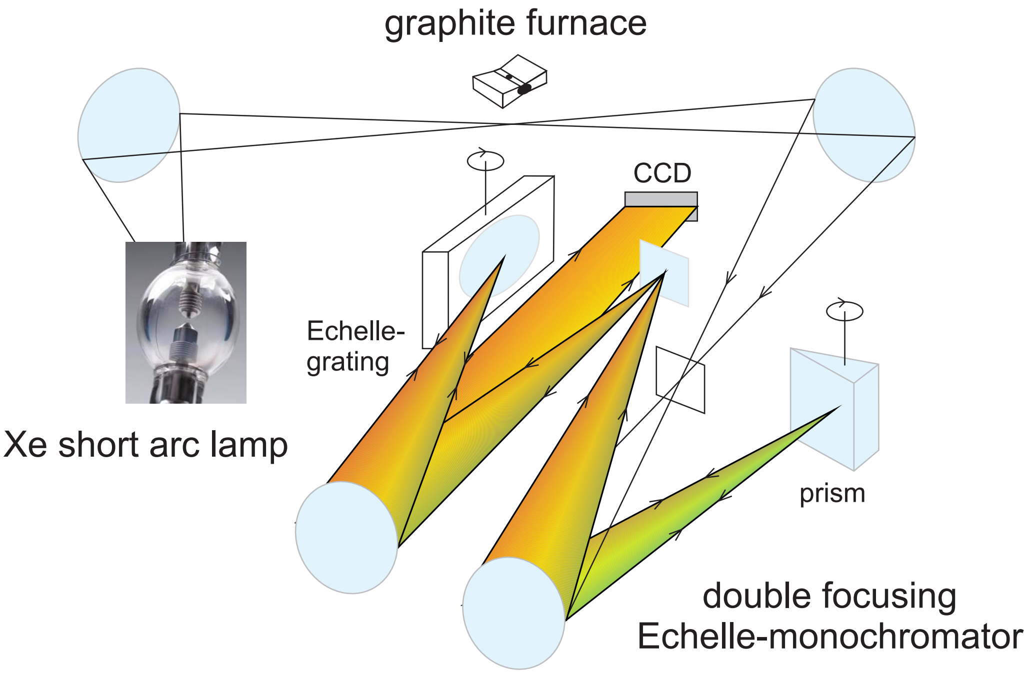

Figure 2.13: Set-up for high resolution continuum source graphite furnace atomic absorption (HR-CS-GF-AAS)[79].

2.7 ICP-Mass spectrometry

In ICP-MS the same plasma as in ICP-OES (Section 2.1) is used to excite and ionize the analyte atoms. In ICP-MS, however, ions are sampled from the plasma and after separation with respect to charge to mass ratio they are detected. The plasma operates in the same way as in ICP-OES, however, in ICP-MS it is necessary to shield the plasma form capacitive coupling with the electric field of the rf coil. Otherwise the ions created inside the plasma will feel an external field giving rise to a kinetic energy spread, which at any case should be avoided in mass spectrometry.

In the ICP-MS used here[82] a cooled spray chamber is used to reduce the solvent vapor load of the plasma, which is easily extinguished at a too high vapor content. Especially for organic solvents it is useful to cool the spray chamber. Here a carbon entry into the plasma could cause a carbon deposition on the plasma torch, the skimmer and the sampler cones of the ion interface. A second benefit from a reduced solvent vapor input in the case of H_2O is the reduced oxidation of analyte species.

In the instrument used, a high matrix introduction (HMI) kit is installed so as to enable the introduction of high matrix containing sample solutions into the plasma. Effectively, a further Ar stream is used so as to dilute the tertiary aerosol coming from the spray chamber. By the dilution of the aerosol with Ar an external dilution of the sample can be avoided, which reduces risks of contamination and errors in sample preparation.

From the upper regions of the plasma the ions are extracted from the plasma through a sampler and a skimmer cone. A roughing vacuum is applied behind the sampler cone with the aid of a rotary vacuum pump and a high vacuum is applied behind the skimmer cone. The ion optics include a beam stop between the skimmer and the mass spectrometer so as to prevent photons from passing through the system to the detector.

In ICP-MS mass interferences from polyatomic species are common and arise from the plasma gas Ar, the O from the solvent H_2O, and the acids used for sample digestion and stabilization such as HCl, HNO_3 or H_2SO_4. In this work interferences stemming form HCl and HNO_3 are due to the sample digestion process (compare chapter 3.2) Especially for Se only the ^{82}Se isotope is likely not to be interfered. In Table 2.2 some interferences, which are often encountered in ICP-MS are listed. The list is far from complete and better lists can be found in the literature[83].

Table 2.2: Examples of polyatomic interferences in ICP-MS[83].

Isotope	Abundance	Interferences
^{39}K	93.08	$^{38}Ar^{1}H^{+}$
^{40}Ca	96.97	$^{40}Ar^{+}$
^{56}Fe	91.66	$^{40}Ar^{16}O^{+}$; $^{40}Ca^{16}O^{+}$; $^{38}Ar^{18}O^{+}$; $^{38}Ar^{17}O^{1}H^{+}$; $^{37}Cl^{18}O^{1}H^{+}$
^{59}Co	100.	$^{43}Ca^{16}O^{+}$; $^{42}Ca^{16}O^{+1}H^{+}$; $^{36}Ar^{23}Na^{+}$; $^{40}Ar^{18}O^{1}H^{+}$; $^{40}Ar^{19}F^{+}$
^{75}As	100.	$^{40}Ar^{35}Cl^{+}$; $^{36}Ar^{38}Ar^{1}H^{+}$; $^{38}Ar^{37}Cl^{+}$; $^{36}Ar^{39}K^{+}$; $^{43}Ca^{16}O_2^{+}$
^{74}Se	0.87	$^{37}Cl^{37}Cl^{+}$; $^{36}Ar^{38}Ar^{+}$; $^{38}Ar^{36}S^{+}$; $^{40}Ar^{34}S^{+}$
^{76}Se	9.02	$^{40}Ar^{36}Ar^{+}$; $^{38}Ar^{38}Ar^{+}$
^{77}Se	7.58	$^{40}Ar^{37}Cl^{+}$; $^{36}Ar^{40}Ar^{1}H^{+}$; $^{38}Ar_2{}^{1}H^{+}$; $^{12}C^{19}F^{14}N^{16}O_2^{+}$
^{78}Se	23.52	$^{40}Ar^{38}Ar^{+}$; $^{38}Ar^{40}Ca^{+}$
^{80}Se	49.82	$^{40}Ar_2^{+}$; $^{32}S^{16}O_3^{+}$
^{82}Se	9.19	$^{12}C^{35}Cl_2^{+}$; $^{34}S^{16}O_3^{+}$; $^{40}Ar_2{}^{1}H_2^{+}$

Polyatomic interferences can be removed through the use of a collision or reaction cell. In the determination of Se^{+} H_2 and O_2 are often used. A mass shift due to a reaction can either be achieved through the reaction of the ion of interest[84] (see Equation 2.13) or of the interferent (see Equations 2.14 and 2.15) with the gas added[85].

$$Se^{+} + O_2 \rightarrow SeO^{+} + O \tag{2.13}$$

$$Ar_2^{+} + H_2 \rightarrow ArH^{+} + Ar + H \tag{2.14}$$

$$Ar_2^{+} + H_2 \rightarrow ArH_2^{+} + Ar \tag{2.15}$$

A simpler and more general approach is to use a collision cell where He is entered. Based on the principle of kinetic energy discrimination (KED) polyatomic interferents can be removed from the ion of interest and compared to the reaction mode no possible new interferences here can occur from other elements in the sample, which are isobaric to the generated new analyte masses. In the KED mode one makes use of the fact that polyatomic species have a larger collision cross section than monoatomic ions. In the collision cell the analyte and the isobaric species enter with the same kinetic energy distribution. With each collision the kinetic energy of the ions is equally reduced for the polyatomic and monoatomic species but due to the collision cross section polyatomic species collide more often with the He atoms than the monoatomic species on their way through the collision cell. At the end of the cell only the monoatomic species with the higher kinetic energy will make it over an applied potential barrier. As mentioned before a narrow kinetic energy distribution is necessary for this type of separation and a capacitive coupling of the rf electric field of the coils to the plasma has to be avoided.

The mass separation in the instrument used is taking place in a quadrupole mass filter. In a quadrupole two pairs of electrode rods are each connected to a direct current source with opposite polarity. In addition a variable high frequency is superimposed. This set-up allows ions to pass the mass filter in dependence on their mass and the applied high frequency field brings them on stable transition paths.

$$\frac{m}{z} = 5.7\frac{U}{\omega^2 r^2} \tag{2.16}$$

m is the ion mass, r is the quadrupole radius, V is the alternating current, ω is the frequency and z is the charge.

The mass resolution depends on the frequency of the field (f), the length of the quadrupole (L) and the kinetic energy of the ions when entering the quadrupole (V_Z), as given in Equation 2.17

$$\frac{\overline{m}}{\Delta m} = 0.05\left(fL\sqrt{\frac{m}{2V_Z}}\right)^2 \tag{2.17}$$

3 Experimental

3.1 Chemicals

For sample digestion and dilution of the standard solutions, HNO_3 and HCl of analytical grade available from Merck (Darmstadt, Germany) were used. They were additionally purified by subboiling distillation. All standard solutions were obtained from Merck (Darmstadt, Germany) in ICP purity grade and a concentration of 1 $g{\cdot}L^{-1}$. They were diluted with water to give an matrix matched standard solution with an appropriate concentration range for the analysis with the instruments used throughout this work.

Bi_2Te_3 (99.98%) and Sb_2Te_3 (99.999%) reference materials were purchased from Alfa Aesar (Karlsruhe, Germany). $Bi(NO_3)_3$ was purchased from Sigma Aldrich (Seelze, Germany) in 99.999% purity grade.

Doubly distilled water was used for dilution of the standard solutions and the solutions of the digested samples. Alternatively high purity water, purified by a Labo Star 7TWF-DI/-UV (Siemens, Berlin, Germany), with a maximum conductivity of 0.055 $upmu S{\cdot}cm^{-1}$ was used.

3.2 Sample dissolution

All samples were weighed with a Sartorius MC-5 micro-balance (Data Weighing Systems INC, Chicago, IL, USA). After weighing the Si wafer with deposited sample, Bi_2Te_3 samples were digested in an open vessel by adding 0.65 mL HNO_3 20% (v/v). The Sb_2Te_3 and $Bi_{2-x}Sb_xTe_3$ samples were digested in an open vessel by adding a mixture of 0.65 mL HNO_3 20% (v/v) and 0.1 mL HCl 35% (v/v). $Bi_2Te_{3-y}Se_y$ samples were digested in an open vessel by adding 0.2 mL HNO_3 65% (v/v). The digestion time required was found to be typically less than one hour. All types of sample solutions after digestion were diluted with water to an apropriate concentration range for the analysis with the respecitve instrument. For ICP-OES analysis they were diluted to 10 mL. The Si wafer, on which the Bi_2Te_3 and Sb_2Te_3 layers were deposited, was dried after digestion and weighed back to quantify the sample amount deposited on it.

Of the Bi_2Te_3 and Sb_2Te_3 reference materials 10 mg were weighed and digested with the same procedure as described for the wafer samples before. After digestion the samples were diluted with water in two steps to a concentration of 10 mg L^{-1}, which equals the concentration for a small amount of sample deposited on the wafer.

Nano-structured samples, which are supplied as slurries in water, were not dissolved for HR-CS-GF-AAS analysis but diluted only with water where it was necessary to obtain an appropriate concentration range for analysis.

3.3 Inductively coupled plasma optical emission spectrometry

The analysis by inductively coupled plasma optical emission spectrometry (ICP-OES) was carried out with a Spectro Cyros$^{CCD®}$ (Spectro Analytical Instruments, Kleve, Germany). This apparatus is equipped with 22 charge coupled devices (CCDs) covering a spectral range from 120 nm to 710 nm. In Table 3.1 the experimental settings used are listed. The necessary minimal sample consumption for a six-fold measurement was found to be 7.2 mL, which means for many samples that only one measurement is possible.

3.4 Data processing software

For computation of the PCR for the analysis results obtained with the ICP-OES, an algorithm was written in Scilab 5.2.2 for Windows 7, 64 bits (Consortium Scilab, Le Chesnay, Cedex, France).

Table 3.1: Experimental conditions of ICP-OES.

Parameter	Setting
Nebulizer type	Modified Lichte nebulizer
Spray chamber	cyclone spray chamber
Power	1400 W
Outer gas flow	13 L min^{-1}
Intermediate gas flow	0.8 L min^{-1}
Nebulizer gas flow	0.7 L min^{-1}
Sample uptake	1.6 mL min^{-1}
Total time of data aquisition	4.5 min

3.5 X-ray powder diffraction

XRD measurements were carried out with a Stoe Stadi P instrument (Stoe, Darmstadt, Germany). Diffraction patterns were recorded as a function of the diffraction peak intensities in an angle from 10° to 80°. A step width of 0.1° and a measurement time of 60 s/step for samples obtained with pulsed deposition and up to 400 s/step for samples obtained with a deposition under the use of a direct current were applied.

Samples were removed from the sample carrier with a razor blade and positioned between two pieces of a adhesive tape. The tape was then fixed on the sample holder of the diffractometer so that the diffractogram could be recorded in transmission. For the production of X-ray radiation an X-ray tube with a Cu target was used. The emitted Cu K-L_3 line with has a wavelength of 1.54 Å was applied.

3.6 Glow discharge time-of-flight mass spectrometry

The glow discharge time-of-flight mass spectrometry (GD-TOF-MS) system (HORIBA Jobin Yvon, France) used consists of an rf GD plasma source, ablating the sample and delivering ions to a extraction time-of-flight mass spectrometer in an orthogonla geometry. A similar system has been described described by Lobo[86,87] and Pisonero[88]. The GD was operated with high purity (6 N) argon at a pressure of approximately 6 mbar, leading to sample ablation and ionization of the sputtered ,species. The ions produced then were transferred through an interface to the time-of-flight mass analyzer equipped with a 70 cm long flight tube and a double stage reflectron operated at a pressure of $5 \cdot 10^{-7}$ mbar. The sample was pressed against an O-ring to secure vacuum tightness of the plasma chamber. A ceramic ring between the sample and a grounded 4 mm diameter anode tube was used to obtain a spacing of 0.15 µm, which proved to be appropriate. A metal block cooled with water to a temperature of 10 °C was pressed by a piston to the back of the sample. It also transferred the rf power from an rf-generator operated at 13.6 MHz and with a maximum power of 150 W, to the sample. The rf-generator was operated in the pulsed mode at a frequency of 250 Hz. The pulses had a length of 2 ms, so that the entire period of interest including the afterglow is 4 ms. Within this time frame full mass spectra were acquired at a frequency of 27.5 kHz. The interface included a quadrupole filter, which allows it to blank out up to four mass ranges in order to prevent overloading of the detector and to increase the dynamic range of the system. Due to the relatively weak adhesion of the thermoelectric layer to the Au substrate a low GD operation power of 30 W was used to ablate the samples. The detection was carried out in the positive ion mode.

3.7 Secondary ion mass spectrometry

For secondary ion mass spectrometry (SIMS) measurements a CAMECA IMS 4550 instrument (CAMECA, Genevilliers, France) was used. The source made use of Cs^+ primary ions at an energy of 5 keV.

3.8 µ-X-ray fluorescence, µ-X-ray powder diffraction

At the Beamline L of the Hamburger Synchrotronstrahlungslabor (HASYLAB) at the "Deutsche Elektronen Synchrotron" (DESY) µ-XRF and µ-XRD experiment, were performed[89,90], which allowed it to scan a sample and to measure the XRF and XRD patterns simultaneously with a X-ray beam spot diameter of 15 µm. Step sizes between the spots were chosen according to the sample size they were between 210 µm and 294 µm in the case of a mapping of the complete sample and 15 µm when performing a closer examination of smaller areas. A single bounce capillary (XOS, NY, USA) was used for the combined µ-XRD and µ-XRF measurements at 30 keV. To achieve better statistics, also µ-XRF -only-measurements were made under the use of polycapillary optics at 17.4 keV. Here the sample was mounted on a movable sample holder in the focal plane of the X-ray beam under an angle of 45°. In the energy dispersive spectrometer a Si drift detector (SDD) (Vortex, SII NanoTechnology USA Inc., Northridge, CA, USA) was mounted under a 90° angle with respect to the incoming beam at the side of the sample. The diffracted X-rays produced a pattern on a 16.5 cm diameter MAR CCD165 detector (Marresearch, Norderstedt, Germany), which was mounted behind the sample and the detected signal intensities in this diffraction pattern were integrated as a function of to the diffraction angle so as to obtain a powder diffractogram.

The set-up at beamline L is shown in Figure 3.1 and 3.2.

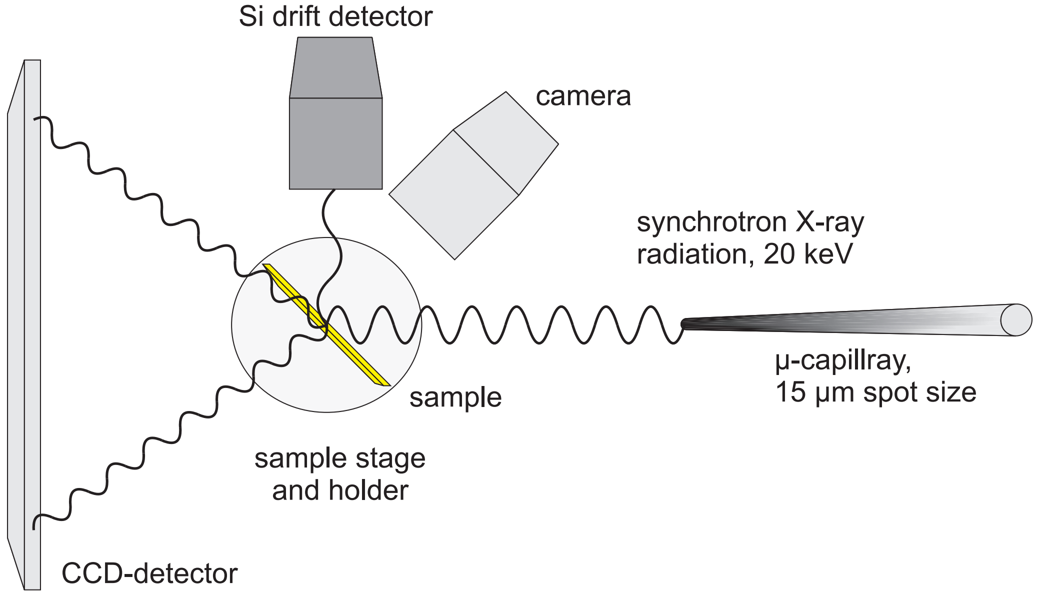

Figure 3.1: Set-up for simultaneous XRF and XRD measurements with the synchrotron at DESY Hasylab beamline L.

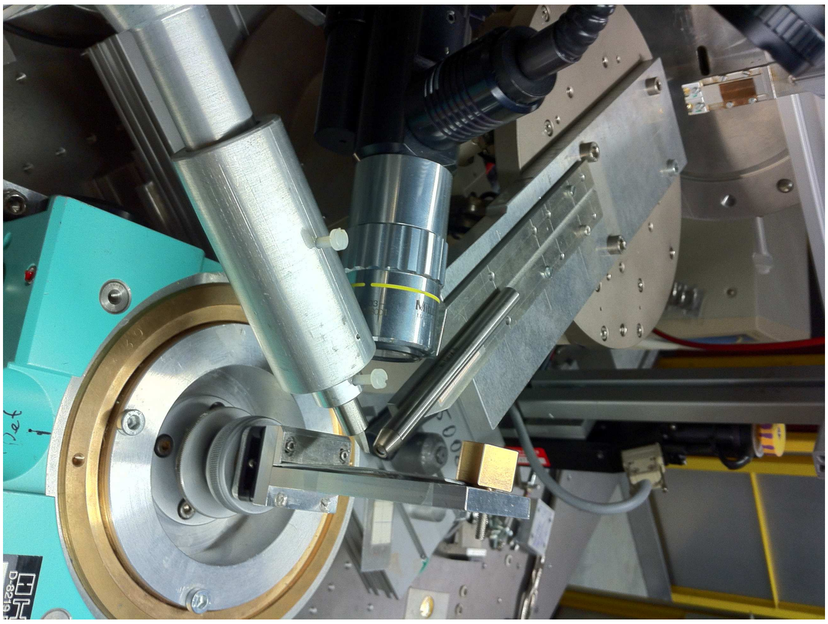

Figure 3.2: Photograph of the set-up for simultaneous XRF and XRD measurements at the synchrotron, DESY Hasylab, beamline L. (A courtesy of Dipl.-Chem. M. Menzel.)

3.9 μ-X-ray abosorption near edge structure

μ-X-ray abosorption near edge structure (μ-XANES) analyses were also performed at beam line L in fluorescence mode, using the SDD-detector and scanning the excitation energy by using the Si111 crystal monochromator available at beam line L. The polycapillary optics described above were used for the experiments. The spectra were processed using the program ATHENA[91], basing on the library IFEFFIT[92].

3.10 High resolution continuum sours graphite furnace atomic absorption spectrometry

High resolution continuum source graphite furnac atomic absorption spectrometry (HR-CS-GF AAS) measurements were carried out with the ContrAA700 instrument (Analytik Jena, Jena, Germany). Graphite tubes with a L'vov platform were used. Samples and standard solutions were pipetted into the tube with the automatic sampling system. The elements Bi, Sb and Te were determined under the use of graphite furnace atomization and a mixture of matrix modifiers. As modifiers $Pd(NO_3)_2$ and $Mg(NO_3)_2$ were used[93]. For all measurements 5 µ L of a 3 g· L^{-1} solution of Pd and 5 µL of a 2 g· L^{-1} solution of Mg were added to 10 µL of the respective calibration standard solutions, which were acidified with 2% HNO_3.

For the temperature program optimization the pyrolysis and atomization curves for 10 µL aliquots of the standard solutions containing 100 µg·L^{-1} and of slurries, which were diluted so that approximately 1 ng per element is contained in 10 µL of slurry were compared. The optimized temperature programs for Bi, Te and Sb are given in Table 3.2, 3.3 and 3.4.

Table 3.2: Optimized temperature program for the determination of Bi.

Step	Temperautre [°C]	Ramp [°C·s^{-1}]	hold time [s]	Gas flow
drying	80	6	20	max
drying	90	3	20	max
drying	110	5	10	max
pyrolysis	350	50	20	max
pyrolysis	1100	300	10	max
gas flow adjustment	1100	0	5	stop
atomization	1100	0	5	stop
atomization	1900	1500	4	stop
cleaning	2450	500	5	max

In Figure 3.3 the pyrolysis and atomization of dry residues of standard solutions and of slurry samples are compared. As expected it was found that a calibration with standard solutions in the case of slurry samples is possible, since the atomization and pyrolysis temperatures well agree[94].

For the determination of the linear dynamic ranges the calibration standard solutions were prepared by a dilution of ICP grade standard solutions (Merck, Darmstadt, Germany). The concentration range of 0.1 µg· L^{-1} to 300 mg· L^{-1} for the elements Bi, Sb and Te could be covered by a single calibration curve for each element. The linear dynamic range could be expanded by measuring the absorbances at different pixels, namely at the line maximum and

Table 3.3: Optimized temperature program for the determination of Te.

Step	Temperautre [°C]	Ramp [°C·s^{-1}]	hold time [s]	Gas flow
drying	80	6	20	max
drying	90	3	20	max
drying	110	5	10	max
pyrolysis	350	50	20	max
pyrolysis	1100	300	10	max
gas flow adjustment	1100	0	5	stop
atomization	1100	0	5	stop
atomization	2100	1500	4	stop
cleaning	2450	500	5	max

Table 3.4: Optimized temperature program for the determination of Sb.

Step	Temperautre [°C]	Ramp [°C·s^{-1}]	hold time [s]	Gas flow
drying	80	6	20	max
drying	90	3	20	max
drying	110	5	10	max
pyrolysis	350	50	20	max
pyrolysis	900	300	10	max
gas flow adjustment	1300	0	5	stop
atomization	1500	0	5	stop
atomization	2100	1500	4	stop
cleaning	2450	500	5	max

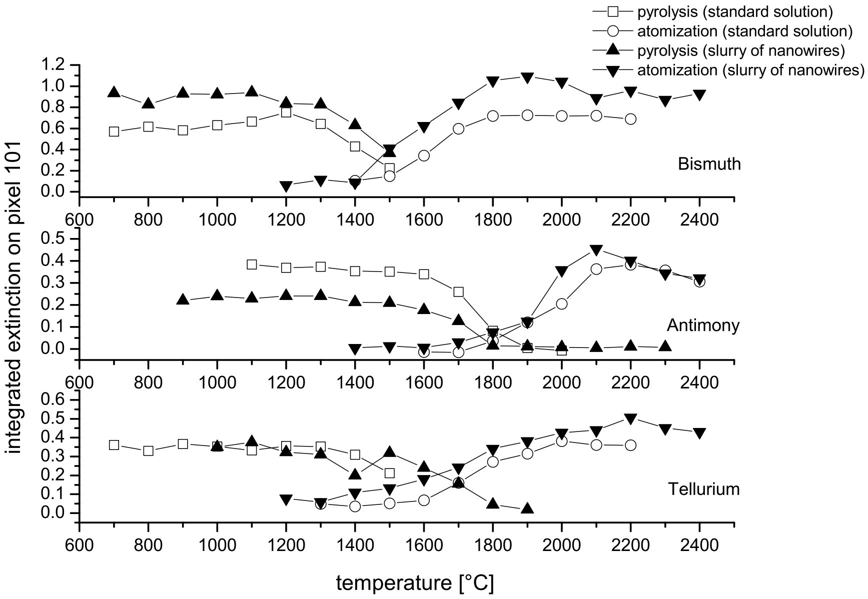

Figure 3.3: Pyrolysis and atomization curves for the determination of Bi, Sb and Te in the case of dry residues of both standard solution and slurry samples containing Bi, Sb and Te concentrations of 1 ng per element in 20 µL of standard solution and approximately 1 ng per element in 20 µL of slurry, respectively.

aside the peak maximum in the case of the analytical line. In the latter case usually two pixels at the same distance away from the pixel with the peak maximum were selected.

3.11 Total reflection X-ray fluorescence

For total reflection X-ray fluorescence (TXRF) analyses quartz glass carriers were used. They were rinsed with analytical grade petroleum ether so as to remove nonpolar contaminations or mechanically removable contaminations in a first step. In a second step the carrier was cleaned with an alkaline cleaning solution RBS 50. This was diluted to 5% (Fluka, now part of Sigma Aldrich, Seelze, Germany). The solutions were used at 80 °C and the carriere were cleaned thoroughly with high purity water. In a third step the carrier was submerged into HNO_3 (5%) heated to 80 °C and cleaned thoroughly with high purity water. Sample preparation in TXRF requires a siliconization of the quartz glass carrier used. Therefor 5 µL of a silicon solution (Serva silicon solution in isopropanol, Serva, Heidelberg, Germany) were pipetted on the carrier. To make the solid sample stick to the treated surface, grease (Vaseline®) was provided as a thin film on the siliconized sample carrier. For this purpose 5 µL of a 1 $g\cdot L^{-1}$ solution of grease dissolved in petroleum ether were dried on the surface before dispensing 5 µ L of the slurry sample on the carrier. In the case of the analysis of nanowires the samples were presented as slurries and the slurry sample was not homogenized as the nanowires are contained in a 5 µ L sampling volume. Measurements were done with a Picofox (Bruker, Berlin, Germany) instrument using a W X-ray tube. Triplicate analyses with a 1000 s integration of the fluorescence signals were made for every sample.

3.12 Inductively coupled plasma mass spectrometry

Inductively coupled plasma mass spectrometry (ICP-MS) analyses were carried out with a Agilent 7700X (Agilent Technologies, Palo Alto, CA, USA) equipped with a He collision cell. As nebulizer a Micromist (G3266-8003, Glass expansion, Melbourne, Australia) in combination with a double pass Scott type spray chamber was used. The experimental settings used are listed in Table 3.5 .

The selected masses were ^{82}Se, ^{121}Sb, ^{130}Te and ^{209}Bi.

Table 3.5: Experimental conditions of ICP-MS.

Parameter	Setting
Nebulizer type	Micromist nebulizer
Spray chamber	Scott double pass (peltier cooled) spray chamber
Spray chamber temperature	12.0 °C
Power	1550 W
Outer gas flow	15.00 L min^{-1}
Intermediate gas flow	0.90 L min^{-1}
Nebulizer gas flow	0.72 L min^{-1}
Nebulizer make up gas flow	0.40 L min^{-1}
Sample uptake	0.6 mL min^{-1}

With the instrument used a tuning of the ion lenses in the interface and the detector voltages is done automatically in the software auto tuning mode. In this procedure use was made of a multi-element tuning solution (concentrations of Li, Mg, Y, Ce, Tl, Co: 1 $\mu g \cdot L^{-1}$).

3.13 Potential Seebeck microprobe

Measurements of the Seebeck coefficient (S) were performed with a potential Seebeck microprobe instrument (compare Section 2.5). Here under the mounting of a probe tip to a movable sample stage the determination of spatially resolved S-coefficient values were possible. Resolutions in the µm range can be obtained[5]. In this work a resolution of 200 µm was selected. The applied temperature difference between the heated tip and the sample was selected to be 1.8 K for Bi_2Te_3 and to 2.6 K for Sb_2Te_3, respectively.

4 Bulk analysis of thermoelectric layers

4.1 Introduction

As stated in chapter 1.1 precise main component determinations in the field of thermoelectrics are often omitted, or their precision is not carefully evaluated. On the other hand it is clear that the material properties strongly depend on the composition[2,34]. Here not only main components have to be considered but also contaminations, which can easily be intercalated[23,53]. All this necessitates precise and accurate determinations of the main components and of possible contaminants, as it is possible with ICP-OES.

In Section 4.2 a procedure for the precise determination of the main components with ICP-OES will be described, which makes use of multiple emission line regression procedures for calibration. For the structural characterization of a material XRD measurements were used. In Section 4.3 it will be shown, that the deposited samples have the expected crystal structures and the results of an investigation on the dependence of the crystal quality on the deposition parameters will be reported. The possibility to determine impurities with ICP-OES will be evaluated in Section 4.4. It will be discussed in Section 4.5 how the analytical results can be very informative to improve the material quality with respect to the Seebeck coefficient values and comparisons with other research will be made.

The results presented in this chapter were the subject of two publications[48,95] and were the topic of a Bachelor thesis[96].

4.2 Improvements of the precision in inductively coupled plasma optical emission spectrometry

For the determination of elements in a sample, calibration with synthetic standard solutions can be used. Here the line intensities for a series of standard solutions with known concentrations are measured. The limit of quantification (LOQ) depends on the desired precision of the results and the chosen confidence level. The LOQ determined from the standard deviation of the blank ($10\,\sigma$ criterion) will expectedly be smaller but not result in the same precision, which will in this work be defined by the use of confidence intervals (CI) rather than the typically used relative standard deviations (RSD). This definition is used to emphasize the importance of the reliability of the results rather than just the precision. To decrease the confidence intervals for the analysis results, the principal component regression (PCR) using the results of determinations with a multitude of analyte emission lines and a pooled regression, which uses a summation of the line intensities from a multitude of emission lines, is applied. It will be shown that a lower LOQ with respect to calibration with a single emission line can be achieved when using a multitude of emission lines under the application of PCR and pooled regression. Accordingly, the confidence interval of the quantification for the case of the same amount of sample can be improved.

4.2.1 Data analysis

PCR was described as a popular and intuitive technique for use in atomic spectrometry[97]. A good explanation for how to use multiple emission lines in optical emission spectrometry for quantitative analysis in ICP-OES with CCD detection can be found in the literature[98,99]. Each of L detected emission lines shows a sensitivity S, which is expressed as a count rate at the detector per unit of concentration c. For each element all sensitivities can be summarized as a sensitivity vector $\mathbf{s}$.

$$\mathbf{s} = \begin{pmatrix} S_1 \\ S_2 \\ \vdots \\ S_L \end{pmatrix} \tag{4.1}$$

For a calibration the background corrected signal, obtained for N calibration standard solutions with the concentrations C are measured, which can be expressed as a vector **c**.

$$\mathbf{c} = \begin{pmatrix} C_1 \\ C_2 \\ \vdots \\ C_N \end{pmatrix} \tag{4.2}$$

All intensities are than expressed by the intensity matrix **I**.

$$\mathbf{I} = \mathbf{c} \cdot \mathbf{s^T} + \mathbf{E} \tag{4.3}$$

The next step of the procedure is to find the Eigenvectors **x** of the **I** matrix and the associated Eigenvalues λ. The first Eigenvector λ_1 then gives the transformation from the spectral line intensities to the first principal component pc_1. The main components of **I** can be deduced by solving Equation 4.4

$$\mathbf{A} \cdot \mathbf{x} = \lambda \mathbf{x} \tag{4.4}$$

Here **x** is the Eigenvector of the mean centered variance-covariance matrix **A** and λ the Eigenvalue. **A** can also be expressed as

$$\mathbf{A} = \frac{\sum_{\mathbf{i=1}}^{\mathbf{M}} (\mathbf{c_i} - \bar{\mathbf{c}})}{\mathbf{M}} \mathbf{s} \cdot \mathbf{s^T} + \mathbf{E} \tag{4.5}$$

In Equation 4.5 **E** represents a matrix associated with the noise of the measurement of the emission line intensity.

The first Eigenvector λ_1 is the trace of matrix **A**

$$\lambda_1 = \frac{\sum_{i=1}^{M}(c_i - \bar{c})^2}{M} \times \|s\|^2 = tr(A) \tag{4.6}$$

The first principal component should only be associated with the concentration of the calibration standard samples, but may also include a small part of concentration dependent noise. The first Eigenvector and the Eigenvalue are also mostly independent of the noise matrix **E**. By the omission of **E** a noise reduction is induced.

$$\mathbf{pc_1} = \mathbf{I} \cdot \mathbf{x_1} \tag{4.7}$$

A composite calibration is then possible by substituting Equation 4.3 into Equation 4.7 and plotting the scores of the first principal component against the concentration of the calibration standard samples.

$$\mathbf{pc_1} = \mathbf{c} \cdot \mathbf{s^T} \cdot \mathbf{x_1} \tag{4.8}$$

The gradient $\mathbf{b_1}$, which is the same as the sensitivity, for this calibration will be

$$\mathbf{b_1} = \left\| \mathbf{s^T} \cdot \mathbf{x_1} \right\| \tag{4.9}$$

A quantification is possible by finding the first principal component $pc_{1,sam}$ of the **I** matrix for the sample $\mathbf{I_{sam}}$ and the concentration of the sample is given by

$$c_{sam} = \frac{1}{b_1} \cdot pc_{1,sam} \tag{4.10}$$

4.2.2 Results

For elemental determinations in a sample, a calibration is required so as to be able to quantify the elements of interest. The use of an emission line, which is free of spectral interferences, and therefore has a high sensitivity is adequate for this purpose. To increase the accuracy and the precision of the determination, samples can be analyzed many times over a working day. Limitations for this approach are the amounts of sample available and the measurement time consumed by multiple measurements. These limitations can be circumvented by the use of a multitude of emission lines of which the intensities can be measured simultaneously in ICP-OES with a CCD based spectrometer. The average concentration determined with all detected emission lines is more likely to deliver the accurate analysis result than the concentration determined with one emission line. In Figure 4.1 a multitude of calibration curves for the elements Bi and Te is shown and the figures of merit for all used emission lines of the elements Bi, Sb and Te are listed in Table 4.1, where the data for the line with the lowest LOD (limit of detection) and LOQ are in bold. For all calibration curves a correlation coefficient r^2 higher than 0.999 is obtained and mostly the correlation coefficient is even higher than 0.9999. The LOD was determined from the blank value by Equation 4.11

$$LOD = \frac{\sigma_b}{s} t_{f,\alpha} \sqrt{\frac{1}{\hat{N}} + \frac{1}{N}} \tag{4.11}$$

For a sixfold measurement of the blank value ($\hat{N}$), N separate blank solutions and a significance level a of 99% the student t factor with four degrees of freedom f is 3.747. N is the number of different samples, σ_b is the standard deviation for the blank measurements and s is the sensitivity of the emission line.

Under the assumption of concentration independent standard deviations and with a necessary confidence interval of 1% the LOQ is given by

$$LOQ = \frac{\sigma_b}{s} t_{f,\alpha} \frac{100\%}{1\%} \tag{4.12}$$

When using the PCR instead of line intensities, scores of the first principal component were used for analogue calculations. Since a multitude of emission lines was detected $\hat{N}$ was chosen to represent the number of individual results instead of only a sixfold measurement. The t factor is 2.4 in this case.

Table 4.1: Analytical figures of merit.

Emission line	LOD $[mg\,L^{-1}]$	LOQ $[mg\,L^{-1}]$	r^2
Te 170.000	0.021	1.9	0.99993
Te 170.800	0.35	32	0.99982
Te 175.100	0.086	8.0	0.99994
Te 182.240	0.036	3.3	0.99995
Te 208.116	0.12	11	0.99993
Te 214.281	**0.012**	**1.1**	**0.99994**
Te 214.725	0.065	6.1	0.99989
Te 225.902	0.080	7.5	0.99997
Te 238.570	0.069	6.3	0.99996
Te PCR	**0.0071**	**0.70**	**0.99995**
Te pooled	**0.011**	**1.1**	**0.99996**
Bi 153.317	0.022	2.1	0.99991
Bi 159.179	0.51	47	0.99942
Bi 190.241	0.026	2.5	0.99995
Bi 206.170	0.077	7.1	0.99962
Bi 211.026	0.24	22	0.99996
Bi 222.825	0.032	3.0	0.99998
Bi 223.051	**0.014**	**1.3**	**0.99999**
Bi PCR	**0.0074**	**0.73**	**0.99999**
Bi pooled	**0.0062**	**0.61**	**0.99999**
Sb 151.257	0.095	8.8	0.99996
Sb 172.115	0.27	25	0.99960
Sb 187.115	0.029	2.6	0.99974
Sb 206.833	0.012	1.1	0.99998
Sb 217.581	**0.0073**	**0.67**	**0.99994**
Sb 231.147	0.022	2.0	0.99998
Sb 252.852	0.036	3.4	0.99999
Sb PCR	**0.0061**	**0.60**	**0.99996**
Sb pooled	**0.0057**	**0.57**	**0.99995**

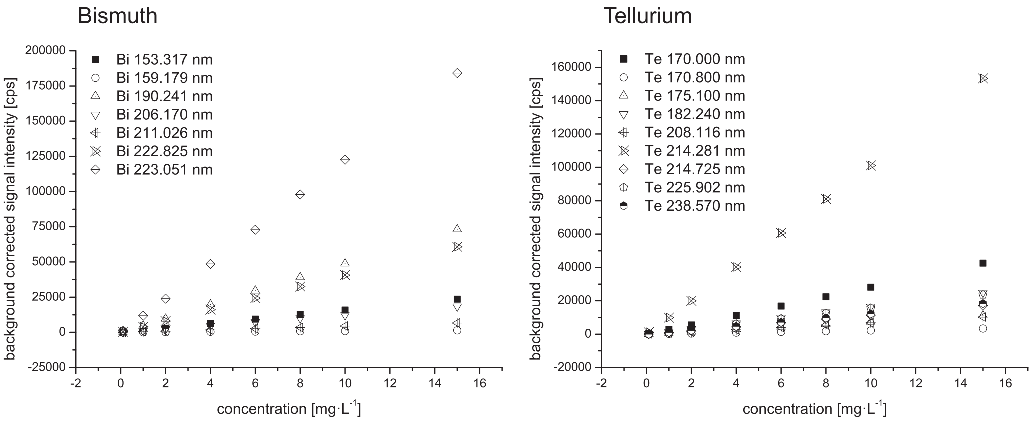

Figure 4.1: Calibration curves for Bi and Te using different atomic emission lines.

In Figure 4.2 it is shown that the abundance of the concentrations found with all emission lines used (Figure 4.3) fitted well with a normal distribution curve, which indicates the absence of spectral interferences.

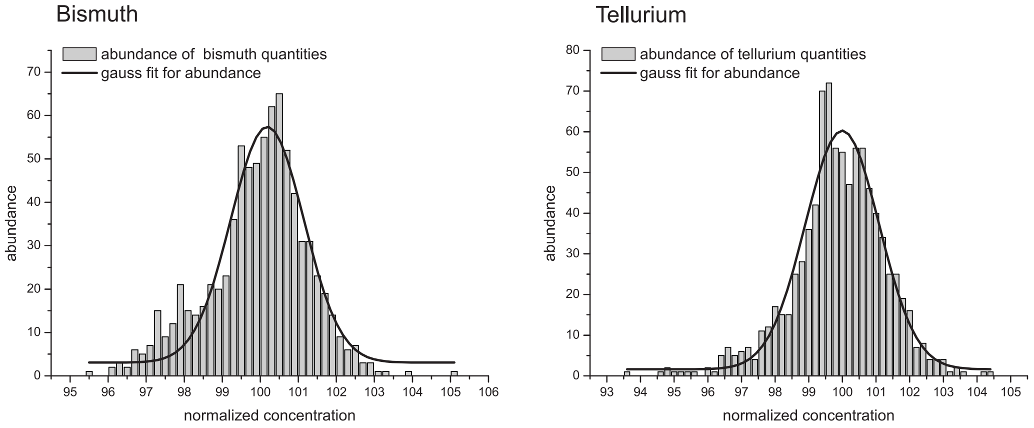

Figure 4.2: Distribution of the analyte concentrations, normalized to their average value, calculated with different analyte emission lines.

To reduce the noise level for the concentrations found, several strategies can be used. If fluctuations in sample delivery or plasma conditions constitute the major part of the signal fluctuations, the use of an internal standard is considered as being promising. Another advantage of the use of an internal standard is the possibility to correct for sample preparation steps, which is obsolete for a small amount of sample since digestion and dilution are car-

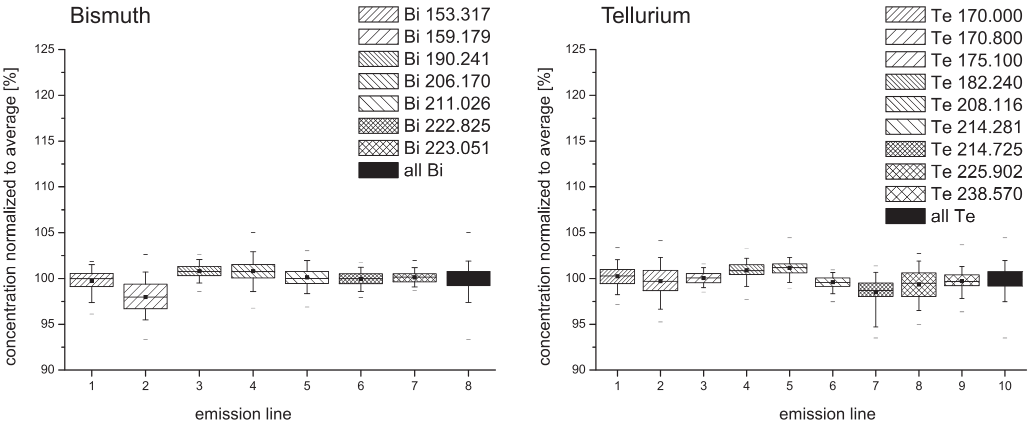

Figure 4.3: Standard deviations of the concentrations for a combination of the results for all emission lines to one dataset and those for the use of single emission lines.

ried out in one vessel for each individual sample and no transferring steps, where losses can occur, have to be considered. In the present case, it was found that an internal standard did not improve the precision, due to the fact that signal fluctuations mostly are not correlated.

Long term drifts are traditionally corrected for by the use of an external standard containing all analytes, which is analyzed in regular intervals. In this case, a drift function is derived and the emission signals are corrected with this function. Salit et al.[100] proposed a superior way to correct for signal drifts. Since the external standard must contain all analytes and is analyzed repeatedly, the result for every sample which is analyzed repeatedly can be used to derive a drift function after normalization to the mean analyte concentration found in that sample.

In Figure 4.4 all results from a measurement series, which extends over a complete working day, are shown. The average drift function derived from them is given in Figure 4.5. An individual drift function for every emission line can be determined and one should take into account that a shift in plasma conditions could easily result in a change in emission line sensitivity ratios. In our study, drift correction improved the precision. All further calculations were therefore done with drift corrected values.

After drift correction, there remains another reason for noise, namely the shot noise, which arises from counting statistics. This kind of noise is truly statistical and cannot be corrected for by an internal standard or a drift correction[101]. The statistical error can only be reduced

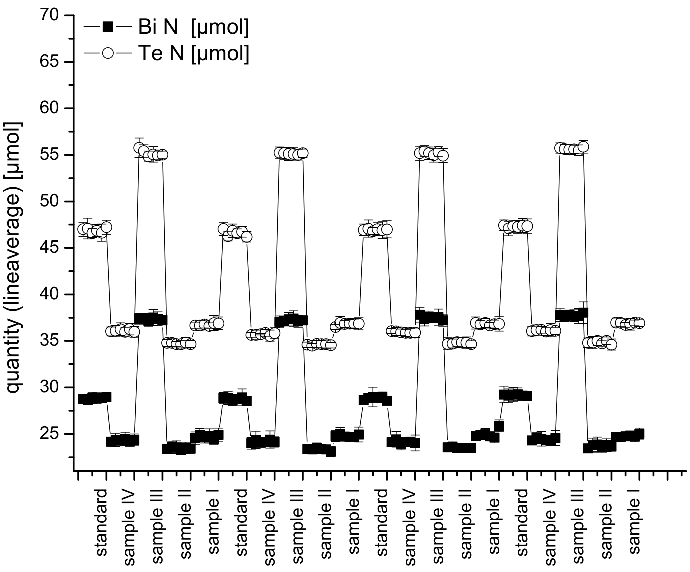

Figure 4.4: Summary of the calculated analyte quantities on the Si wafer. Every sample was analyzed four times (x-axis) with six repetitions (filled squares for Bi and open circles for Te). For every repetition nine emission lines were used (error bars on the symbols). The analyte quantities in total were determined 216 times for every sample.

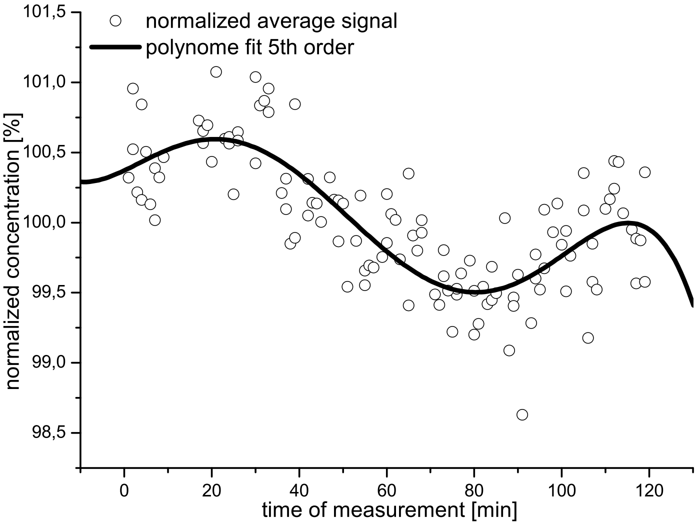

Figure 4.5: Drift function derived from external standardization.

by increasing the number of data points (e.g. by repeating the measurements). Here, the amount of sample limits this approach. However, the detection of multiple emission lines is an alternative. Then a smaller confidence interval for the result is obtained in the case that the concentrations are calculated for different emission lines. The possibility for a systematic error caused by spectral interferences is avoided by only using lines for which the analytical results do not significantly differ from one another. To truly use all emission lines at once, PCR was implemented for data processing and thereby a noise reduction was obtained as explained in the section on principal component regression (compare Section 4.2.1). Another possibility to use all emission lines at once is the summation of all signals. By this the noise should be averaged out and the precision can therefore be improved. Table 4.1 lists the analytical figures of merit.

Application to reference materials

Four Bi_2Te_3 and five Sb_2Te_3 reference samples were dissolved by acid digestion and analyzed. For Bi_2Te_3, a four-fold repetition of the determination of the main components was carried out so as to evaluate the applicability of internal and external standardization as well as of PCR. Due to mostly uncorrelated noise, the internal standardization did not lead to a decrease of the fluctuations. An internal standard is known to facilitate the correction for flicker noise, which is a short term fluctuation of the signal caused by deviations in sample uptake and aerosol generation or transport[101]. These fluctuations apply for every detected signal. To correct fluctuations in energy transfer to the analytes in the plasma, it is recommended that the internal standard element behaves comparable to the analytes[102]. Since a multitude of emission lines and elements is used, this requirement is difficult to fulfill. Accordingly, the applicability of an internal standard hereby may be limited[103]. Small drifts were detected and the correction for drifts therefore brought an increase in the precision. The data treatment with PCR showed a significant effect. The pooled regression brought a comparable large effect, therefore both methods, noise reduction by pooling and by PCR according to Equation 4.3 brought an increase in the precision. In Figure 4.6 an overview is given of the overall confidence intervals for the Bi and Te concentrations determined for the reference materials. In Tables 4.2 and 4.3 the results, which are in good agreement with the expectations for the compositions, and recovery rates (under “untreated” for the line with the lowest LOD and under "PCR" for all lines measured for the respective elements) are shown. The confidence intervals shown in Tables 4.2 and 4.3 are calculated according to Equation 4.13 at a confidence level of 99%.

$$CI = \frac{\sigma t_{f,\alpha}}{\sqrt{N}} \tag{4.13}$$

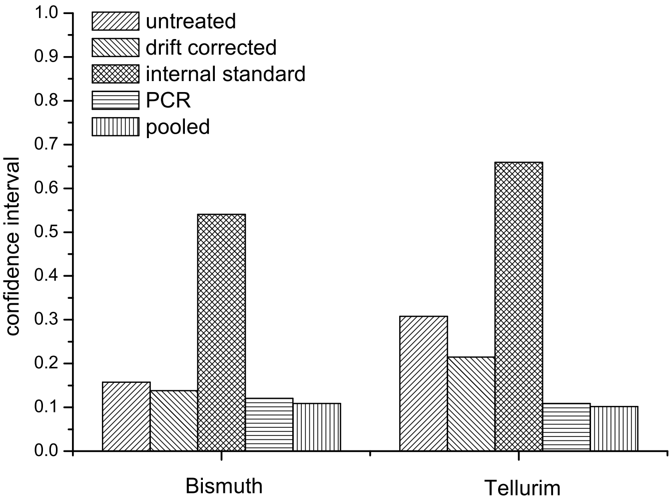

Figure 4.6: The confidence intervals after ratioing to the intensity of the Y 224.306 nm line as the internal standard. Drift correction, internal standardization, principal component regression and pooled regression for Bi 223.051 nm and Te 170.000 nm clearly show that the increase of precision is only achievable with a composite calibration technique. Included in the calculation were all emission lines and all sample measurements.

Application to samples

As described in Section 1.3.3, Bi_2Te_3 and Sb_2Te_3 were electrochemically deposited onto a Si wafer. For technical reasons, it was necessary to sputter a Cr and Au layer onto the Si wafer before the electrochemical deposition was done. By digestion of the samples, these additional layers were also brought into the solutions (Figure 1.5). Therefore, the emission line Bi 206.170 nm can no longer be used because of a spectral interference with a Cr line.

Table 4.2: Composition of Bi_2Te_3 calculated from untreated data, PCR and pooled regression, relative confidence intervals for each value of concentration (Rel. CI) and Recovery rates (Rec.).

	Untreated					PCR					Pooled				
	% Bi	Rel. CI	% Te	Rel. CI	Rec.	% Bi	Rel. CI	% Te	Rel. CI	Rec.	% Bi	Rel. CI	% Te	Rel. CI	Rec.
I	40.2	0.3	59.8	0.7	97.5	40.2	0.2	59.8	0.3	96.6	40.3	0.2	59.7	0.2	97.9
II	40.4	0.3	59.6	0.8	98.1	40.1	0.3	59.9	0.3	97.5	40.3	0.2	59.7	0.3	98.4
III	40.3	0.4	59.7	0.7	98.3	40.2	0.3	59.8	0.2	98.0	40.3	0.2	59.7	0.2	98.7
IV	40.2	0.6	59.8	0.7	97.9	40.2	0.3	59.8	0.2	96.9	40.3	0.3	59.7	0.2	98.2
Average	40.3	0.4	59.7	0.7	97.9	40.2	0.3	59.8	0.2	97.3	40.3	0.2	59.7	0.2	98.3

Table 4.3: Composition of Sb_2Te_3 calculated from untreated data, PCR and pooled regression, relative confidence intervals for each value of concentration (Rel. CI) and Recovery rates (Rec.).

	Untreated					PCR					Pooled				
	% Sb	Rel. CI	% Te	Rel. CI	Rec.	% Sb	Rel. CI	% Te	Rel. CI	Rec.	% Sb	Rel. CI	% Te	Rel. CI	Rec.
I	37.7	1.3	62.3	1.2	96.7	37.8	0.8	61.9	1.0	97.2	37.1	0.8	62.9	0.8	99.8
II	37.5	0.5	62.5	0.7	94.4	38.1	0.5	62.0	0.4	95.0	37.0	0.9	63.0	0.5	97.5
III	37.6	0.9	62.4	0.9	100.5	38.0	0.6	62.1	0.6	100.7	37.0	1.3	62.9	0.8	103.4
IV	36.4	0.9	63.6	0.8	99.2	36.8	0.8	63.2	0.7	99.5	35.9	1.2	64.1	0.8	102.2
V	37.8	1.3	62.2	1.6	100.7	38.0	0.9	62.0	0.9	100.8	37.2	1.1	62.8	0.9	101.2
Average	37.4	1.0	62.6	1.0	98.3	37.7	0.7	62.3	0.7	98.6	36.9	1.1	63.9	0.7	100.8

In order to optimize the deposition, the used potential was varied so as to identify the optimum conditions. From the results in Figure 4.7 the stoichiometries obtained for different deposition potential for the case of Bi_2Te_3 and Sb_2Te_3 are shown and the optimum deposition potential can easily be identified. For Bi in Bi_2Te_3 the theoretical composition could be obtained whereas for Sb in Sb_2Te_3 slightly higher Sb concentrations were found. More details about the deposition conditions are described by Schumacher et al.[95].

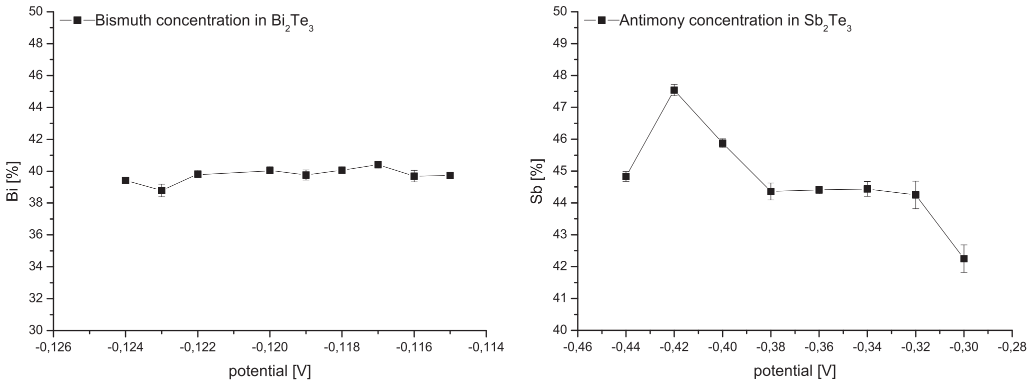

Figure 4.7: Determination of Bi and Sb in electrodeposited $Bi_2Te_3$and Sb_2Te_3 films. The data were treated with PCR, as described for the reference materials.

4.3 X-ray powder diffraction

In order to determine the structure of the deposited samples XRD measurements were performed. Reflex indexing can be done according to database entries, but details of the set-up have to be taken into account to match the database entries with the obtained diffractograms. A detailed indexing of diffraction reflexes with the aid of a Rietveld analysis was performed.

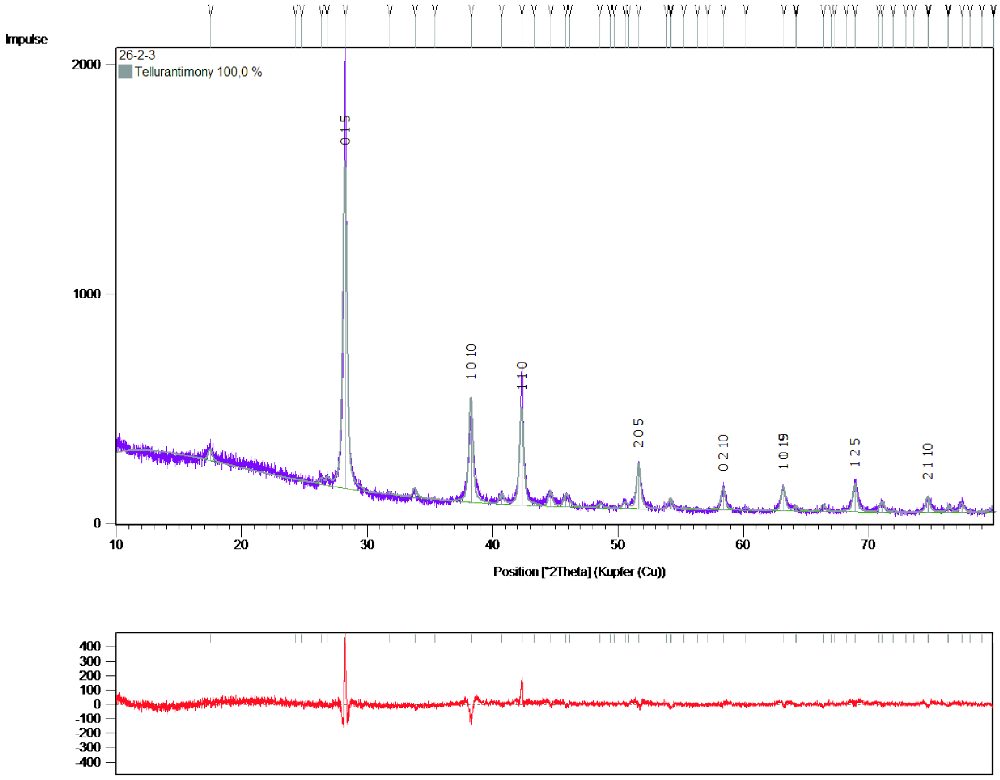

Figure 4.8: Superimposed Rietvelt plot and difference diagram for the Rietveld refinement for an Sb_2Te_3 sample.

The best agreement between database entries and the measured diffractogram is found for Sb_2Te_3 (PDF-Nr.: 00-015-0874). Deviations of the reflex positions from the database entries indirectly indicate deviations from the stoichiometry. Deviations of the reflex intensity pattern indicate preferred crystal orientations in the deposited samples.

From the reflexes (015) and (110) at 28° and 42° the cell constants can be calculated according to Equation 2.8 and the (015) reflex is used for the calculation of the crystallite size according to Equation 2.9.

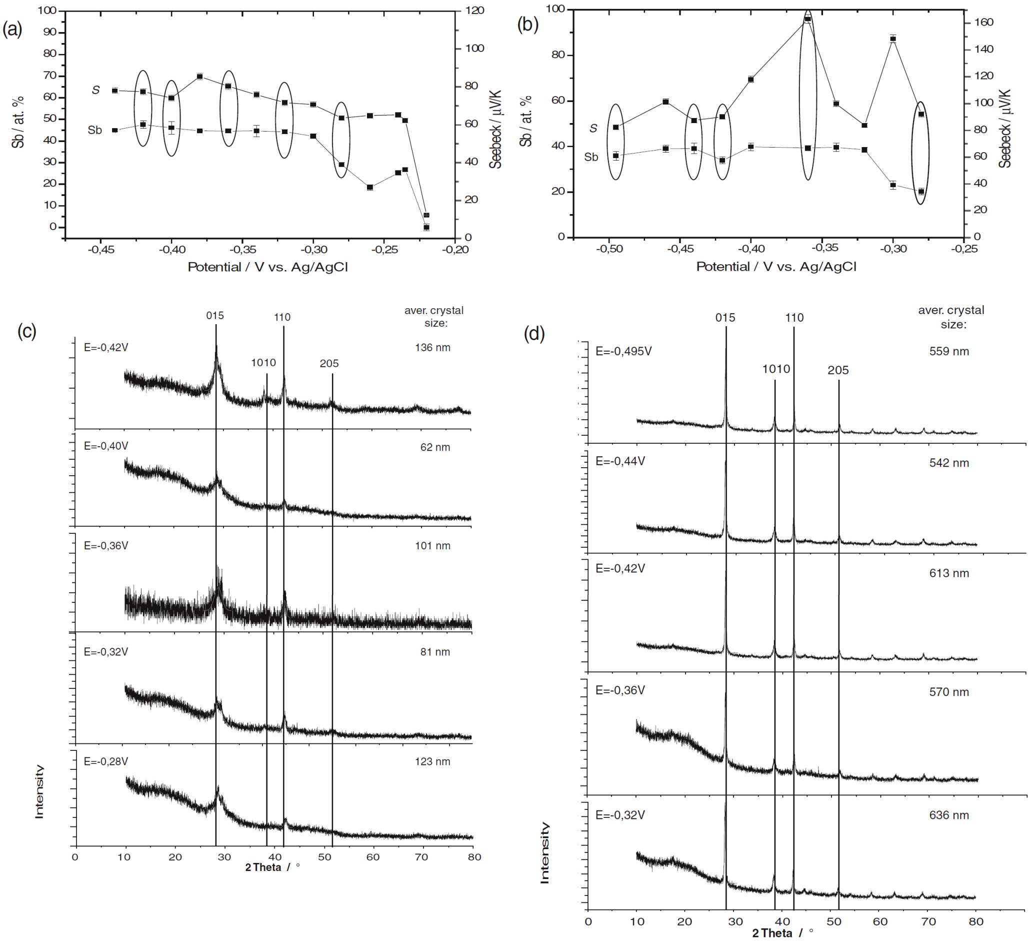

Figure 4.9: Composition (at.% Sb) and Seebeck coefficient [µV K^{-1}] of dc-deposited Sb_2Te_3 (a) and Sb_2Te_3 layers obtained by pulsed deposition (b). XRD graphs of dc-deposited thin films (c) and pulse-deposited thin films(d)[95].

Sb_2Te_3 films deposited under a constant potential show large deposited grains, which are irregularly distributed on the sample surface. In contrast herewith Sb_2Te_3 deposited under pulsed potential conditions show needle-like crystal structures as reported in the literature[104]. Furthermore the films deposited under a dc potential show rough surfaces compared to the layers deposited under a pulsed potential. For both types of deposition the dependence of the stoichiometries on the potential dependence was investigated under the use of ICP-OES analyses. To securely identify the deposited material as the Sb_2Te_3 crystallites, XRD measurements were performed. Both sets of data are shown in Figure 4.9. From the data it can be seen that the films obtained under a constant dc potential show smaller crystallites than those deposited under pulsed deposition. The calculation was done according to formula 2.9 from the (015) reflex. In Table 4.4 the dependency of the composition, the cell constants a_{lat} and c_{lat} and the crystallite size on the deposition potential is shown.

Films deposited under a constant dc potential and those deposited under pulsed conditions differ also in the crystal plane sizes a and c. It is worth to note that the values for the films deposited under a pulsed potential are considerably closer to the expected values[105].

The interpretation and an explanation of the processes taking place is out of the scope of this work and was given in the publication associated with the data presented in this chapter[95].

Table 4.4: Sb concentration [at.%] results from XRD measurements: lattice parameter a_{lat} [Å] with standard deviation of 0.4%, c_{lat} [Å] 0.9% crystal size [nm] ±2.5%[95].

	U_{dep} [V]	Sb [at.%]	a_{lat} [Å]	c_{lat} [Å]	crystalite size [nm]
Literature[105]			4.262	30.450	
Deposited at	-0.42	46.41	4.271	28.730	137
constant dc potential	-0.40	46.06	4.269	29.084	62
	-0.36	45.24	4.271	28.242	102
	-0.32	46.38	4.273	28.729	81
	-0.28	51.37	4.280	28.715	123
Deposited at	-0.495	35.85	4.261	30.363	560
pulsed potential	-0.440	39.08	4.265	30.218	543
conditions	-0.420	33.81	4.263	30.323	613
	-0.360	39.33	4.263	30.339	570
	-0.320	20.25	4.265	30.314	637

4.4 Determination of impurities in thermoelectric materials with inductively coupled plasma optical emission spectrometry

Impurities in thermoelectric materials may influence the materials properties severely. Investigations revealed that the intercalation of Cu into Bi_2Te_3 changes the mode of conduction from p-type to n-type. The intercalation of Cu occurs along one axis of the crystal between $Te - Te$ layers, which are bonded by Van-der-Waals forces. The intercalation of Au and Ag was also discovered to be relatively fast[53]. After the desired compound has been deposited not only the main components but also present of trace impurities therefore have to be determined.

Spectra for a series of randomly selected samples were recorded and the detection limits for the elements found were determined. The detection limits LOD in the case of several emission lines were determined according to DIN 32 645 with the student factor $t(f = 2, P = 95\%) = 2.920$, where P is the probability level of 95%.

The detection limits for Au, Cu, Fe, K, Ni, Zn were found to be in the low $\mu g \cdot L^{-1}$ range and beyond these concentrations they can be determined with ICP-OES. For the elements Mg, Ca and Na the determined limits of detection are comparable but here lower values might be achieved by working under clean room conditions.

After calibration low absolute and relative method standard deviations were obtained. The calibration alone can be assumed to be precise and accurate. The high absolute standard deviation for Au can be explained through the large range of the calibration. Indeed the relative method standard deviation is in the same range as for all the other elements, which is between 0.6 and 2.3%. The higher value for Na again has to be explained by the high risk of sample contamination under the experimental conditions. All calibrations were found to be linear according to a Mandel outlier test.

$Bi_{2-x}Sb_xTe_3$

All samples were dissolved in HNO_3 and HCl. In the solutions of the dissolved $Bi_{2-x}Sb_xTe_3$ samples the elements Ca, Cu, Fe, K, Mg, Na and Zn were found in addition to Au and

Table 4.5: Limits of detection for trace elements in thermoelectric materials

Element	Linie [nm]	LOD [$\mu g \cdot L^{-1}$]
Au (I)	242.795	0.59
Au (I)	267.595	0.77
Ca (II)	393.366	1.2
Ca (II)	396.847	1.1
Cr (II)	205.552	0.35
Cu (I)	324.754	1.01
Cu (I)	327.396	1.6
Fe (II)	238.204	0.35
Fe (II)	259.941	0.35
K (I)	766.491	1.3
Mg (II)	279.553	0.10
Mg (II)	280.270	0.13
Na (I)	589.592	1.3
Ni (II)	221.648	0.31
Ni (II)	231.604	0.47
Zn (II)	206.191	0.94
Zn (I)	213.856	0.28

Table 4.6: Residual standard deviation s_y, method standard deviation s_{x0}, relative method standard deviation and coefficient of variation r^2 for the trace element determination with the aid of ICP-OES.

Element	Linie [nm]	$s_y[counts \cdot s^{-1}]$	s_{x0} $[\mu g \cdot g^{-1}]$	$V_{x0}[\%]$	r^2
Au	242.795	439	15.6	0.60	0.9999
	267.595	562	17.8	0.68	1.0000
Ca	393.366	3610	0.284	1.09	0.9999
	396.847	1040	0.182	0.67	0.9998
Cr	205.552	11.3	0.111	0.85	1.0000
Cu	324.754	164	0.495	0.76	0.9999
	327.396	104	0.794	1.21	0.9999
Fe	238.204	29.3	0.283	2.16	0.9998
	259.941	26.0	0.141	1.08	0.9999
K	766.491	56.5	0.301	2.30	0.9998
Mg	279.553	1130	0.111	0.85	1.0000
	280.270	635	0.112	0.86	0.9999
Na	589.592	1040	0.551	4.21	0.9997
Ni	221.648	24.0	0.199	1.52	0.9999
	231.604	17.8	0.157	1.20	0.9998
Zn	206.191	17.2	0.211	1.61	0.9999
	213.856	28.4	0.137	1.05	0.9998

Cr, which were determined. The latter indeed were deposited on the Si wafer before the electrochemical deposition of the thermoelectric layers. Some elements, such as K, Mg and Ca can be assumed to be contaminations on the surface of the deposited layers. This could be proved by rinsing the samples with doubly distilled water before dissolution of the thermoelectric layer. Indeed, a decrease of their concentration below the detection limit was found for the series of samples which were rinsed opposed to the series for samples which were not rinsed.

Table 4.7: Concentration range of trace elements in $Bi_{2-x}Sb_xTe_3$-samples and the relative standard deviations.

Element	c [$\mu g \cdot g^{-1}$]	RSD [%]
Au	10000-750000	0.5
Ca	<20-4600	2.9
Cr	10-1500	2.0
Cu	<17-1200	2.8
Fe	<6-1700	2.0
K	<22-570	11
Mg	<2-100	2.3
Na	<23-150	1.5
Ni	<5-160	7.2
Zn	<16-170	7.4

Most elements could be determined with a standard deviation below 3%, which is an acceptable value for trace element determinations. Elements, for which higher standard deviations were found (such as Fe, Ni and Zn) proved to be present at low concentrations only and therefore their relative standard deviations were higher. Au is almost a main component of the samples and it could be determined with very low standard deviations of 0.5% only.

4.5 Physical properties of Sb_2Te_3

Under the aid of the results of precise main component determinations in thermoelectric layers the electrochemical deposition processes have been optimized. An insight in the success of the optimization of the thermoelectric behavior of Sb_2Te_3 is given by a comparison of the Seebeck coefficient values obtained from pulsed deposited samples as a function of dependence of their stoichiometry. It can be clearly seen in Figure 4.10 that the highest Seebeck coefficient values were achieved at or near the optimum stoichiometry of 40% Sb. A decrease of 1% in the Sb concentration already leads to a decrease of the Seebeck coefficient by 60%.

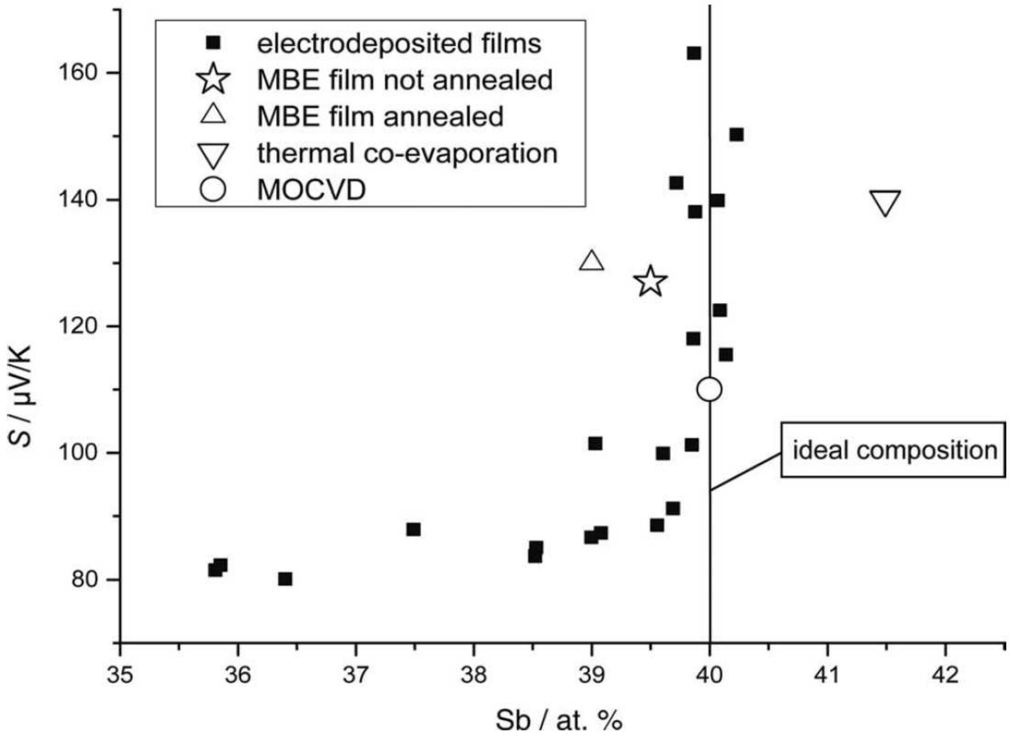

Figure 4.10: Distribution of Seebeck coefficients of Sb_2Te_3 deposited at pulsed potential films (10/50 ms) with a stoichiometry around the ideal composition of 40 at.% Sb. Sb_2Te_3 films before and after annealing obtained by molecular beam epitaxy (MBE)[106], films deposited by thermal co-evaporation[107], films deposited by metal organi chemical vapor deposition (MOCVD)[95,108].

4.6 Conclusions

A procedure based on ICP-OES was developed for the determination of the main components of electrochemically deposited samples. The procedure was validated by the determination of the same elements in commercially available reference materials. Recovery rates and compositions proved to be in good agreement with the expected values. To decrease the confidence intervals, the use of external and internal standards has been tested and found to be not a suitable mean to correct for signal fluctuations. The use of several emission lines as possible with ICP-OES using a simultaneous CCD detection enables the application of PCR for a composite calibration technique. It was shown that the confidence intervals of the results could be decreased by a factor of 2 to 3 as shown in Tables 4.2 and 4.3. Accordingly, the LOQ could be decreased by the composite calibration technique. The principal component regression as well as the calibration with pooled intensities showed superior in terms of the analytical figures of merit (Table 4.1) as compared to the results with the most suitable spectral line only (e.g. Te 170.000 nm, Bi 223.051 nm, Sb 217.581 nm) and it is thereby obvious that due to the increased number of signals the confidence intervals of the results can be decreased. The absence of obvious outliers among the results is a strong indication that the emission lines used are free of spectral interferences. This is an additional information, which cannot be obtained when using only one emission line. Additionally, the developed procedures show superior over the one with repeated measurements using one emission line in terms of time and sample consumption.

By the use of the developed procedures, the deposition conditions for thermoelectric films can be improved systematically. Samples were analyzed to determine optimum parameters and a potential range for the deposition of materials with the desired compositions can be found. The developed procedures are applicable to Bi_2Te_3 and Sb_2Te_3 samples. (Fig. 4.7), as proven by the analysis of a reference material (Tables 4.2 and 4.3) using PCR.

The use of ICP-OES with CCD detection and PCR data processing was shown to be suitable for the determination of the main components in small sample amounts of thermoelectric materials. The procedure is fast and reliable and will be tested also for other samples with a low number of constituents, when a multitude of uninterfered spectral lines can be used. It generally should be possible to improve the precision in the case of statistical noise limited measurements as shown here.

With the aid of the results of main component determinations the choice of deposition conditions for optimized thermoelectric materials is possible as shown for the example of Sb_2Te_3. The structural properties could be changed by the use of a pulsed deposition procedure in contrast to a direct current procedure[5]. The improvements were proven with XRD measurements and crystallite size calculations derived from the reflexes, which were recorded. In addition at the example of Sb_2Te_3 the strong influence of the composition on the materials properties was shown. Crystallite sizes were found to be increased from 100 nm for dc deposited to 600 nm for pulsed deposited samples (compare Table 4.4).

Further improvements of the deposition process can be expected with respect to the contaminations found. Up to now not all samples are free of contaminations and they might influence the thermoelectric performance. With the knowledge of the elements found sources for contaminations can be detected and excluded from the procedures. Up to now samples were analyzed and only contamination free samples could be used for further thermoelectric characterization. Detection limits in thermoelectric materials in the form of electrochemically deposited samples were found to range from 0.10 $\mu g \cdot L^{-1}$ for Mg to 1.59 $\mu g \cdot L^{-1}$ for Cu.

At the example of Sb_2Te_3 materials, quality improvements with respect to the Seebeck coefficient are documented by the results shown in figure 4.10. A relatively small deviation of 1 at.% from the optimum composition was shwon to decrease the Seebeck coefficient by 60%. As shown with this example an optimization of the electrochemical deposition and the materials properties strongly depends on the precise concentration values of the main components as they can be determined with ICP-OES.

5 Homogeneity control

5.1 Introduction

GD-TOF-MS

GD-TOF-MS is a suitable method to gain depth-profile information in the case of electrically conducting as well as of electrically non-conducting samples. The so-called "source profile" generated from the transient signals of the pulsed rf plasma can be divided into three different time windows, namely the prepeak, the plateau and the afterglow time windows. In the prepeak time window the plasma is formed by the action of an electric field. In this time window only plasma gas ions are detectable as sample sputtered species are not yet present in the plasma to be ionized[86]. In the plateau region, the discharge reaches a stationary state, where the production of electrons and ions is balanced by their loss through diffusion to the chamber walls. In this time window the ionization is known to be mainly the result of electron impact (approximately 90%) and collision with metastable atoms[109]. After the electric field has been switched off the electrons are no longer accelerated to the anode. By collisions with atoms they quickly loose their initial energy and it comes to a thermal equilibrium with the surrounding gas. By this thermalization process the electron number density is expected to sharply increase by several orders of magnitude, as described by Bogaerts[110]. Due to the thermalization a dissociative recombination process between electrons and Ar_2^+ ions is induced during the afterglow and the number of highly excited Ar species reaches a maximum in the afterglow. Therefore this ionization process qualitatively explains the intense Ar signals during the afterglow. Analyte signal increases during the afterglow may be explained in a similar way or by enhanced Penning ionization (ionization by Ar metastables)[110]. One can easily imagine that every element will behave differently in response to well-defined afterglow conditions depending on its energetic properties. Therefore, the source profiles for the signals for the isotopes ^{209}Bi and ^{130}Te were studied by GD-TOF-MS in the case of thermoelectric layers of Bi_2Te_3 deposited on Si substrates. The results presented in this section have been published recently[49].

μ-XRF, μ-XRD and μ-XANES

The Seebeck coefficient (S) is well known to be dependent on the stoichiometry of a material and it is related to the crystal structure and grain sizes of the material, because of the influence of scattering processes of charge carriers at the grain boundaries[2]. To achieve a deeper understanding of the deposition process, which is important for a later upscaling for industrial production, and to investigate the origin of variations in the Seebeck coefficient, the homogeneity in terms of the crystal structure and chemical composition of the sample has to be determined. With inductively coupled plasma optical emission spectroscopy (ICP-OES) the determined bulk composition of three samples of Bi_2Te_3 and Sb_2Te_3 each, which are similar to those analyzed here, proved that the electrochemical deposits have an ideal stoichiometry with variances between 0.1 and 0.6 at%. To determine the microscopic stoichiometry a medium spatial resolution (several micrometers) is preferred, to be able to monitor representative parts of the sample in an acceptable time. X-ray microprobe experiments allow for a characterization of the material not only with respect to the chemical composition but also to the crystal structure and valence either simultaneously or consecutively. The applied microprobe techniques are namely micro-X-ray fluorescence (μ-XRF), micro-X-ray diffraction (μ-XRD) and micro-X-ray absorption near edge structure (μ-XANES) analysis. Under the use of capillary optics, a spatial resolution of 15 μm can be obtained, which is sufficient to identify a correlation of the Seebeck coefficients with the inhomogeneity found and it is possible to detect also smaller inhomogeneities. Compared to electron microprobe analysis (EMPA) and X-ray photo electron spectrometry (XPS) the applied methods provide an information depth of several tens of micrometers covering the entire depth of the thermoelectric deposits analyzed here. Accordingly, in this study the lateral homogeneity of the thermoelectric deposits with the aid of synchrotron μ-XRF and μ-XRD) as well as of μ-XANES was investigated and the results presented in this section have also recently been published[50].

5.2 Depth-profile analysis with glow discharge time-of-flight mass spectrometry

GD-TOF-MS “Source Profiles”

In Figure 5.1 a typical source profile is shown. As expected in the afterglow region (once rf potential is turned off) ion signals strongly increase, due to the effects described before. Three integration time windows have been selected to generate depth-profiles: the full source profile, a period during the plateau and a period in the afterglow regime, in which peaks exhibit a maximum. The most “interesting” part of the glow discharge operation is certainly the afterglow region in which higher signal-to-noise ratios are observed. It was found that the behavior of ^{130}Te greatly differs from the behavior of ^{209}Bi in the afterglow region. While for Te one peak maximum occurs in the afterglow region two peaks are observed for ^{209}Bi.

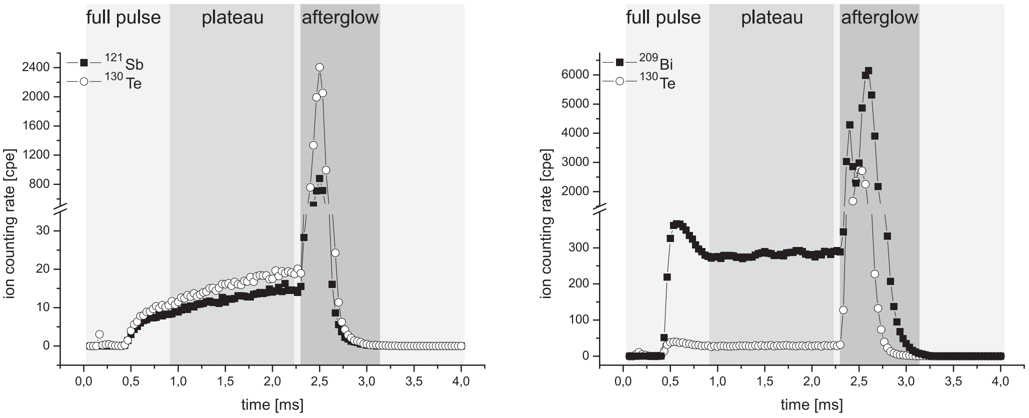

Figure 5.1: Source profiles obtained for Sb_2Te_3 (left) and Bi_2Te_3 (right). Source profile data shown here are acquired for both samples 100 s after the glow discharge was started so that variations seen cannot be attributed to surface effects. The ion counting rates for the most abundant isotopes of the elements of interest are shown.

Time to depth conversion

The exact thickness of the thermoelectric layer was determined by scanning electron microscopy (SEM) as a complementary method. SEM measurements were performed on cross sections of the craters obtained by PP-TOFMS analysis. The thickness determined with

SEM-EDS was used to convert the sputtering time to the depth for the thermoelectric layer. To perform a time to depth conversion within the Au, Cr and Si layers of the sample the thickness of each of the Cr and Au layers was assumed to be 20 nm, which is known from the deposition rates for the Au and Cr layers during the production process of the samples. To perform a time to depth conversion within the thermoelectric layer for the PP-TOFMS analysis the occurrence of the half value of the maximum intensity of the Au peak was considered to indicate the end of the sample film. To perform a time to depth conversion within the sputtered Au and Cr layers and for the Si part of the sample the depth between the occurrence of the half of the maximum intensity for the ^{197}Au peak and the occurrence of the half of the maximum intensity for ^{30}Si is accepted to have a thickness of 40 nm. For the calculations in the case of SIMS analyses the crater depths were measured with the aid of a profilometer and all other calculations were done as in GD-TOF-MS. A schematic representation of the time to depth conversion is given in Figure 5.2.

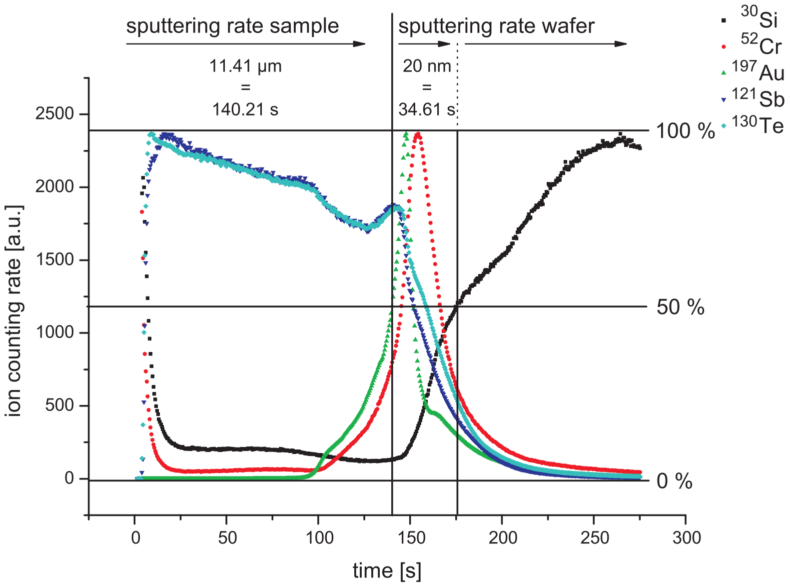

Figure 5.2: Time to depth conversion for Sb_2Te_3. Two sputtering rates, one for the Sb_2Te_3 layer and one for the Au, Cr and Si part of the sample. SEM was also used to study the crater shape.

Qualitative analysis of the samples

The peak maxima in the afterglow pulse period for all isotopes measured, namely ^{121}Sb, ^{209}Bi, ^{130}Te, ^{52}Cr and ^{197}Au were used for the depth-profile measurements with PP-TOFMS. For the isotopic measurements a mass resolving power R of 2700 (measured on $m/z = 197$) under the experimental conditions used was found. From the comparison of the results in Figures 5.3 and 5.4 it can be concluded that the layers were rather homogeneous. With both SIMS and PP-TOFMS, however, small deviations from perfectly flat profiles for the signals of ^{130}Te and ^{121}Sb or ^{130}Te and ^{209}Bi, are found. PP-TOFMS and SIMS profiles are not identical as SIMS is extremely sensitive to matrix changes, whereas PP-TOFMS is much less matrix dependent. For both methods and both sample types the expected order of layers, as it can be seen in Figure 1.5, was found. The thermoelectric layer, consisting of Sb_2Te_3 or Bi_2Te_3, is followed by the Au and the Cr layer and the Si wafer is located below all others. It can be seen that sputtering changes the surface morphology of the sample around the crater and produces rounded crater edges. Particles from the sample are deposited onto the surrounding sample surface. In Figure 5.5 sample morphologies and crater shapes are shown.

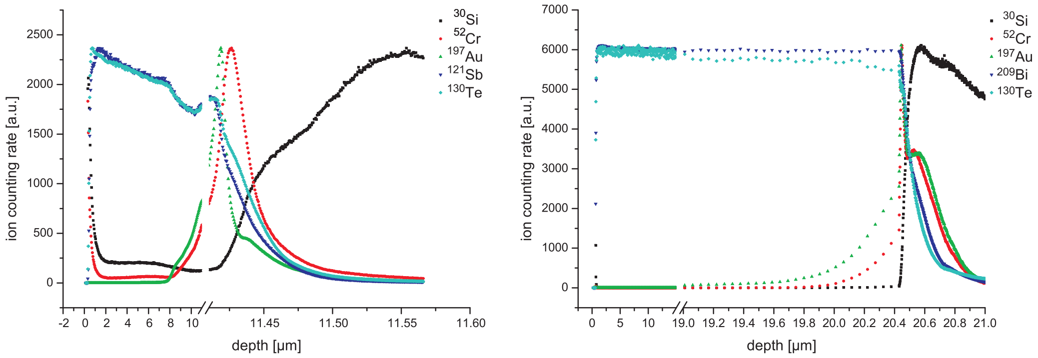

Figure 5.3: Depth-profiles obtained with GD-TOF-MS for Sb_2Te_3 (left) and Bi_2Te_3 (right). For a better overview the ion counting rates have been normalized to their maxima.

Comparison of the sputtering performances in GD-TOF-MS and SIMS

Depth resolution is defined as the distance between 84% and 16% of the depth-profile and it relates to interface sharpness[111]. Depth resolutions were calculated accordingly making

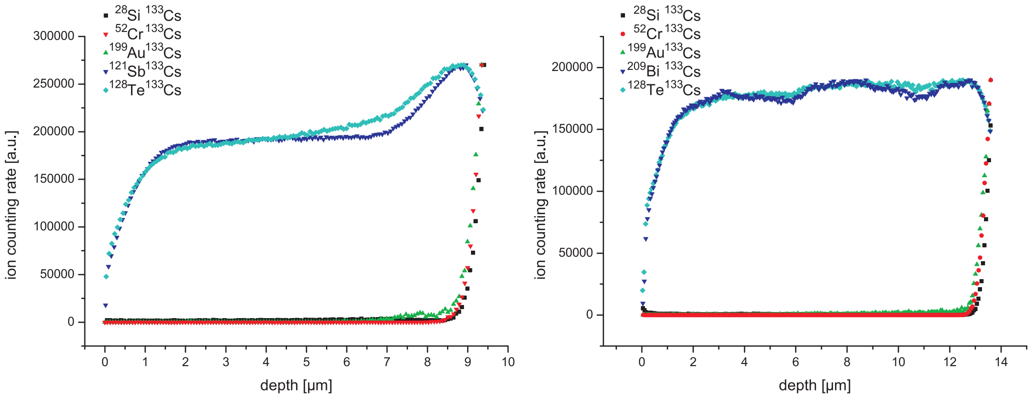

Figure 5.4: Depth-profiles obtained with SIMS for Sb_2Te_3 (left) and Bi_2Te_3 (right). For a better overview the ion counting rates have been normalized to their maxima.

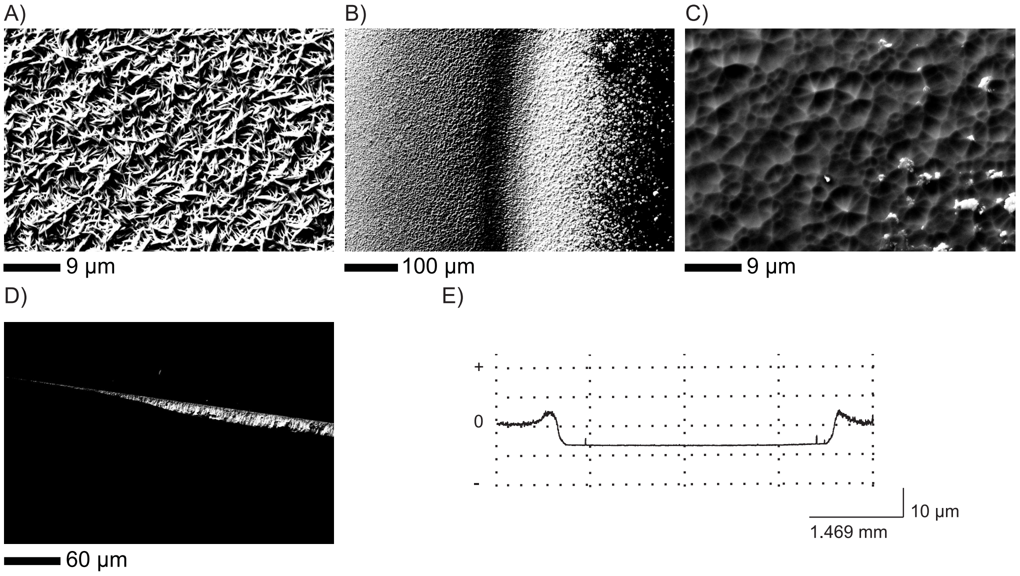

Figure 5.5: Typical crater shapes and sample surfaces after GD sputtering. Needle like structure of a sample area, which was unaffected by the GD (A). Crater rim: the unaffected area is on the left side and the crater is on the right side (B). Crater area (C). Cross section of the sample cut through a crater rim (D). Depth-profile as measured with a mechanical profilometer and confirming the crater shape, which is shown in D (E).

use of the depths, for which the calculation was explained above, and they are given in Table 5.1. The sputtering rates, which were calculated from the measured depth and the sputtering time can be found in Table 5.2. The standard deviations for the sputtering rates and the depth resolutions in the case of the GD measurements are calculated from measurements at three samples. In the case of the SIMS measurements only one sample of each type was analyzed.

Table 5.1: Depth resolution at the different interfaces.

	Depth resolution [nm]									
	GD-TOF-MS					SIMS				
Sb_2Te_3	^{121}Sb	^{130}Te	^{197}Au	^{52}Cr	^{30}Si	^{121}Sb	^{130}Te	^{197}Au	^{52}Cr	^{30}Si
Increasing signal	-	-	1700	1000	81	-	-	250	110	61
Decreasing signal	3400	3700	34	31	-	67	67	41	55	-
Bi_2Te_3	^{209}Bi	^{130}Te	^{197}Au	^{52}Cr	^{30}Si	^{209}Bi	^{130}Te	^{197}Au	^{52}Cr	^{30}Si
Increasing signal	-	-	320	170	53	-	-	-	-	-
Decreasing signal	210	190	350	310	-	-	-	-	-	-

Table 5.2: Sputtering rates obtained with GD-TOF-MS and SIMS.

	Sputtering rate [nm s^{-1}]	
Sample type	GD-TOF-MS	SIMS
Sb_2Te_3	79 ± 0.6	3.37
Bi_2Te_3	82 ± 2.6	2.65

The depth resolution can be calculated from the decrease of the signals for ^{209}Bi, ^{121}Sb or ^{130}Te at the interface with the Au layer, from the increase of the signal for ^{197}Au at this interface or from the decrease of the signal for ^{197}Au at its interface with the Cr layer, from both the increase of the signal for ^{52}Cr and the decrease at the Au or the Si interface and from the increase of the signal for ^{30}Si at the Cr interface (see Figure 1.5). Since the sample morphology significantly changes at the interfaces mentioned the depth resolution also may vary dramatically, which is shown by the calculated depth resolutions reported in Table 5.1. It can be seen clearly that the depth resolution in the case of GD-TOF-MS strongly depends on the sample morphology. Also one has to consider that for the GD-TOF-MS a large sample area is sputtered (4 mm diameter) and so the depth resolution is clearly related to the layer roughness. For the porous thermoelectric layer of Sb_2Te_3 the resolution is therefore poor. At the Au, Cr and Si interfaces this seems to be no longer the case.

In terms of analysis time and sample throughput, GD-TOF-MS is clearly more advantageous, since the sputtering rate is higher by a factor of 26 than in SIMS. For both methods the adhesion of the sample to the Si wafer under the experimental conditions is crucial. For both sample types there were indications from unsuccessful test runs that parts of the sample may peel off from the surface of the Si wafer. This clearly leads to a deterioration of the depth resolution. Therefore, the calculated depth resolutions measured in this work are significantly worse than those, which can be found in the literature for perfectly flat samples[112].

Stoichiometry

The Sb/Te and Bi/Te concentration ratios were determined with a high precision by ICP-OES after wet chemical digestion[48] and with scanning electron microscopy energy dispersive X-ray fluorescence spectrometry (SEM-EDS). Both methods give rather constant values over the whole sample series. The relationship between the ion counting rates in GD-TOF-MS and the concentration was obtained by assigning the average of the ICP-OES results to the average ion counting rates. The isotopic ratios obtained for $^{130}Te/^{121}Sb$ and $^{130}Te/^{209}Bi$ with GD-TOF-MS were constant and, after a calibration to the average, in good agreement with ICP-OES and SEM-EDS data. Since the isotopic distribution is constant the isotopic abundance is proportional to the elemental abundance and no further correction is necessary for the calibration. The results obtained with the three methods are compared in Figure 5.6. The precision obtained with GD-TOF-MS was found to be not as good as in ICP-OES and worse than the results cited in the literature, where relative standard deviations between 0.1% and 1% were found for bulk concentrations larger than 1%[113]. However, having the source profiles in mind it is easy to imagine that the standard deviations for the elemental concentration ratios for Sb and Te as well as for Bi and Te, respectively, depend on the choice of the integration time window within the source profile measured, as it is shown in Figure 5.1. It must be mentioned, however, that the precision could not be increased significantly by the choice of one of the indicated measurement time windows. For Bi_2Te_3 the plateau time window seems to be the best choice so as to obtain low standard deviations, whereas for Sb_2Te_3 a data acquisition over the full pulse duration gives a lower standard deviation. Together with the relative standard deviations for measurements of different samples the relative standard deviations for the $^{130}Te/^{121}Sb$ and $^{130}Te/^{209}Bi$ isotopic signal ratios obtained with one sample only are given in Table 5.3. As mentioned above the isotopic abundance is considered as being proportional to the elemental abundance and no further correction was needed. The standard deviations for measurements at different samples both for Bi_2Te_3 and Sb_2Te_3 are larger than those obtained at the same sample.

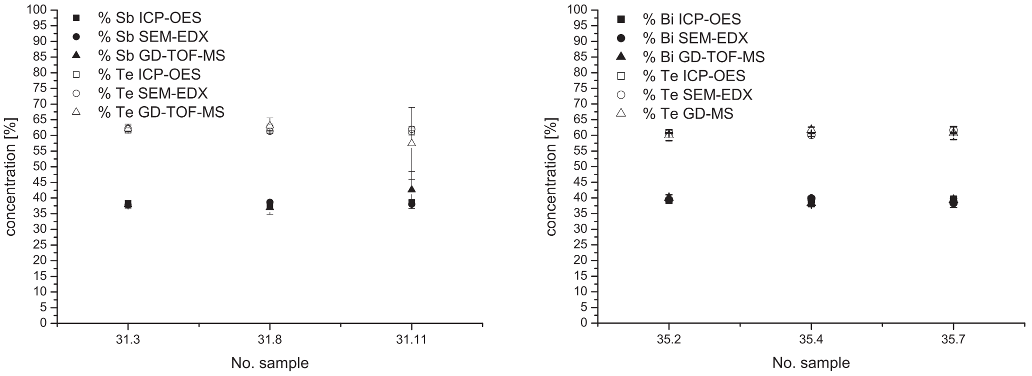

Figure 5.6: Determination of the composition of Sb_2Te_3 (left) and Bi_2Te_3 (right) layers with different methods. For GD-TOF-MS the integration time zone (in the source profile) giving the best precision was selected, i.e. for Sb_2Te_3 the full profile and for Bi_2Te_3 the plateau region.

Table 5.3: Precision obtained in GD-TOF-MS for Bi_2Te_3 and Sb_2Te_3.

No. sample	$^{130}Te/^{121}Sb$ (full pulse)	No. sample	$^{130}Te/^{209}Bi$ (plateau)
31.3	1.7	35.2	1.7
31.8	2.5	35.2	1.9
31.11	4.2	35.2	1.1
Sb_2Te_3	1.7	Bi_2Te_3	3.6

5.3 Lateral homogeneity

5.3.1 Sample thickness calculation

The sample thickness d was determined by optical profilometry and by making use of the extinction of the fluorescence for the L_α line of Au according to the Lambert-Beer law (Equation 5.1).

$$d = \frac{-ln\left(\frac{I}{I_0}\right)}{\left(\frac{\mu}{\rho}\right)_{sample}}\frac{1}{c} \tag{5.1}$$

I is the intensity of the fluorescence for Au with a layer of sample covering it. I_0 is the intensity of the fluorescence for Au without a layer of sample covering it, c is the space concentration of the sample and the mass absorption coefficient of the sample, which are given by according to Equation 5.2

$$\left(\frac{\mu}{\rho}\right)_{sample} = \left(\frac{\mu}{\rho}\right)_{E_0}\frac{1}{\sin\phi} + \left(\frac{\mu}{\rho}\right)_{E_{Au(L)}}\frac{1}{\sin\phi} \tag{5.2}$$

This equation includes the sum of the elemental cross sections for the incoming X-ray beam $\left(\frac{\mu}{\rho}\right)_{E_0}$ multiplied by the inverse sinus of the angle between beam and sample surface and the same product for the Au(L) fluorescence radiation $\left(\frac{\mu}{\rho}\right)_{E_{Au(L)}}$, which is absorbed by the sample.

5.3.2 X-ray fluorescence and X-ray powder diffraction using synchrotron radiation

In Figure 5.7 a typical XRF spectrum acquired from a Sb_2Te_3 sample with 1 s data acquisition time is shown. A good correlation between the fit and the original data could be found.

Analysis of inhomogeneous samples

To demonstrate the suitability of spatially resolved µ-XRF measurements to detect stoichiometric variances of the main components in electrochemically deposited thermoelectric materials a $Bi_{(2-x)}Sb_xTe_3$ sample is analyzed. This has a bulk composition of $Bi_{0.1}Sb_{0.7}Te_{0.2}$

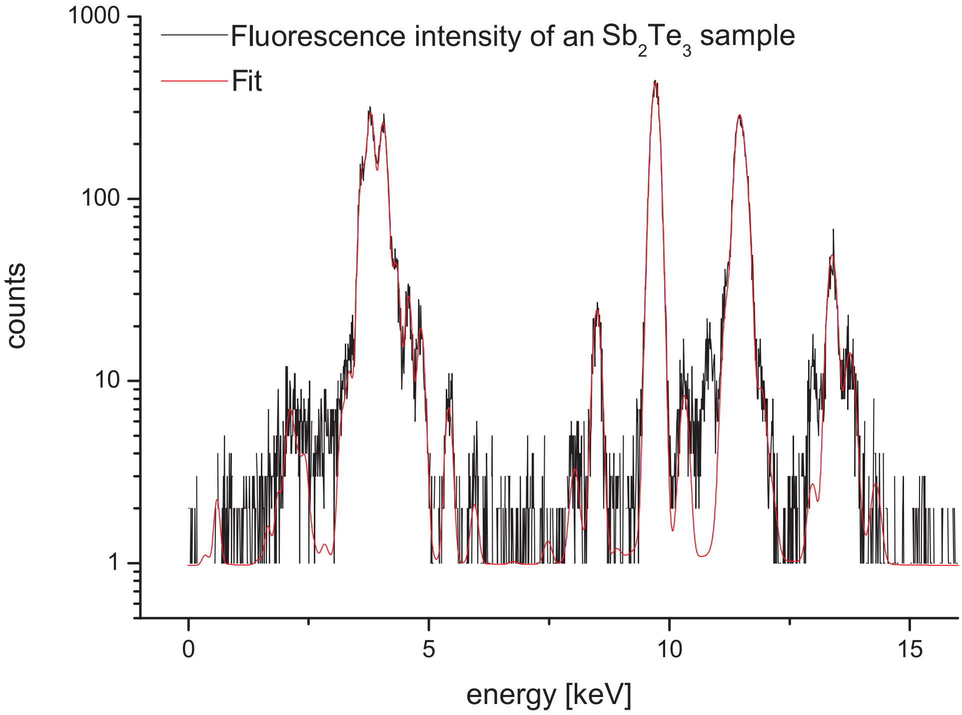

Figure 5.7: Typical XRF-spectrum and the corresponding fit.

instead of the optimized value of $Bi_{1.5}Sb_{0.5}Te_3$. For such a system indication for non-homogeneous depositions have been given in the literature[14,35]. A scan of the sample surface reveals inhomogeneities in the distribution of the main components Bi, Sb and Te, as it is shown in Figure 5.8. Additionally µ-XRD results are presented in Figure 5.8. Here only little variations could be found, which means that structural variances are most certainly found only at relatively large stoichiometric deviations from the targeted product. Since the analysis of optimized samples, in terms of bulk compositions, is much more useful for the development of thermoelectric materials, further measurements concentrated on the bulk composition in the case of optimized samples with respect to.

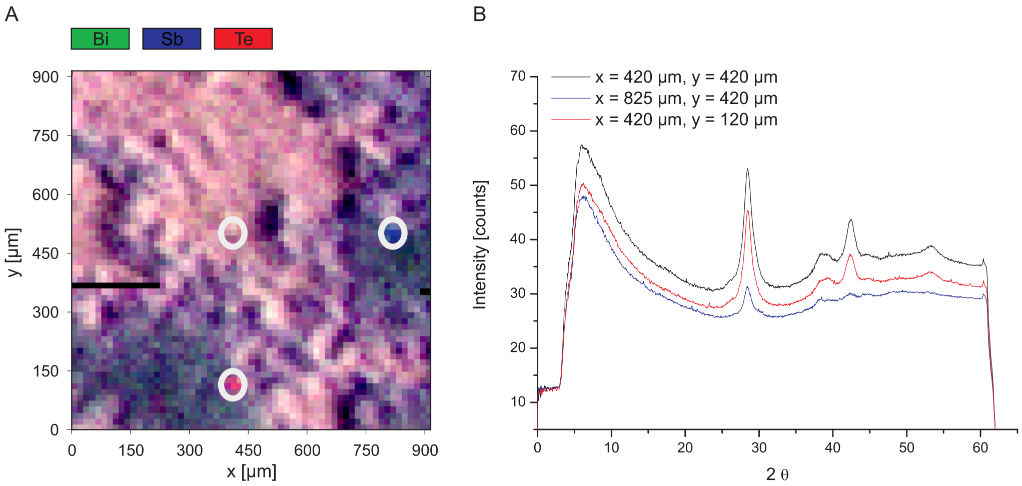

Figure 5.8: µ-XRF mapping and µ-XRD scans of a $Bi_{(2-x)}Sb_xTe_3$ sample analyzed with an X-ray radiation energy of 30 keV. Three color image of the sample with the fluorescence intensities for the Bi(M) line in green, the fluorescence intensities for the Sb(L3) line in blue and the fluorescence intensities for the Te(L3) line in red. Two distinctive spots, where the stoichiometry significantly differs form the one in the rest of the sample, and one spot with average stoichiometry are highlighted in gray (A). µ-XRD of the three highlighted spots (B).

Analysis of homogeneous samples

The thermoelectric material studied here is produced under optimized and reproducible electrochemical synthesis conditions. Here a Seebeck coefficient of up to 160 µV K^{-1} for Sb_2Te_3 and -40 µV K^{-1} for Bi_2Te_3 was obtained. Analyses by ICP-OES showed that deviations of less than 0.3 at.% from the optimal composition for the bulk material for similar samples were obtained. Nevertheless, the S values for this type of electrochemical deposits are good. PSM analyses indicated differences in the Seebeck coefficient S of approximately 40 µV K^{-1} for Sb_2Te_3 and 20 µV K^{-1} for Bi_2Te_3 between locations at the center and in the adjacent area for and Sb_2Te_3 and Bi_2Te_3 (Figure 5.9).

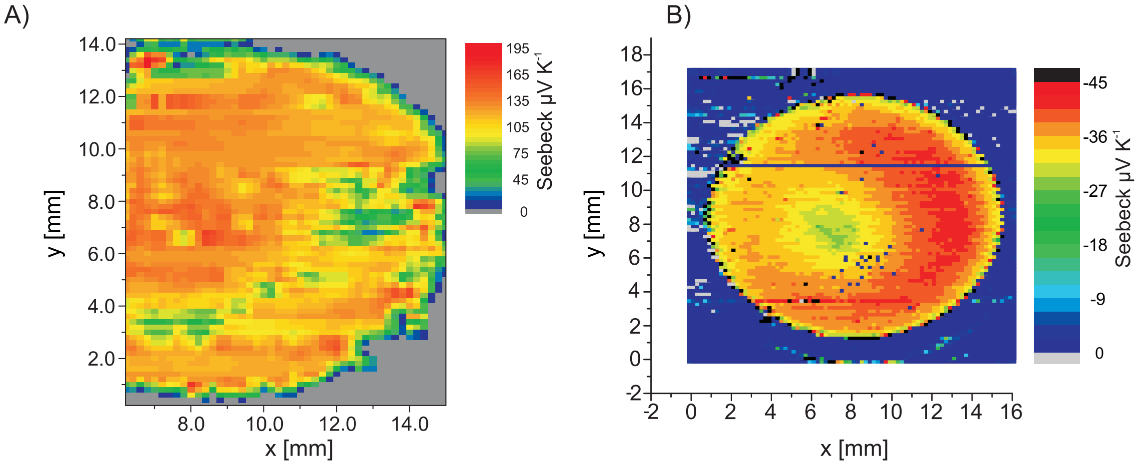

Figure 5.9: Mappings for the Seebeck coefficients S of a Sb_2Te_3 sample (A) and a Bi_2Te_3 sample (B).

µ-XRF was applied to study the micro-stoichiometry of the deposits as described in section 3.8. The ratio of the fluorescence signal for Te(L3) to the fluorescence signal of Sb(L3), which can be found in Figure 5.7, was calculated to determine the stoichiometric homogeneity and a mapping for the sample which is shown in Figure 5.10. The absence of a clear anisotropy indicates that the deposition product has a homogeneous lateral distribution of the main components Sb and Te over the sample. The ratio of the fluorescence for the Te(L3) line to the fluorescence of the Sb(L3) line was found to be 1.9 ± 0.015 over almost the whole deposit except at the rim of the deposit, where there is an increase of the ratio to 2.9 ± 0.110 for the outer spot of 15 µm. The next spot was located at a distance of 294 µm. The errors are expressed as confidence intervals rather than standard deviations to account for the large number of measurements over the sample area. It can be concluded that stoichiometric variations, which were found to be around 0.8% in the middle of the sample, should not significantly affect the Seebeck coefficient. Only a stoichiometric variation of 2 at. % (rel.: 5% for Bi and 3.3% for Te) can be accepted to lead to a considerable decrease of the S values in the materials[95].

Beside the stoichiometry changes in the structure change the thermoelectric properties of the materials and lead to a variation in the Seebeck coefficient S. Experiments with µ-XRD were performed so as to elucidate the micro-homogeneity with respect to the thermoelectric properties. For none of the analyzed specimens a significant difference between the properties in the center and in the other areas was found. A µ-XRD line scan on a Sb_2Te_3 deposit is shown in Figure 5.10 B. For a complete description of the specimen in Figure 5.10 C a comparison of the XRD-patterns for three individual points with a database (PDF 15-874)[114] entry for Sb_2Te_3 is shown. The position of the reflexes match well with the tabulated values. The variation of the reflex positions is 0.015° for the position of the (015) reflex at 28.231° and 0.011° for the position of the (110) reflex at 42.600°. This is of the same order of magnitude as the variation found in the literature for three Sb_2Te_3 diffraction patterns. Here the mean reflex positions are 28.304° ± 0.109° for the (015) reflex and 42.388° ± 0.024° for the (110) reflex (PDF 15-874, PDF 71-393 and PDF 72-1990)[114].

Despite the thermoelectric deposits are homogeneous with respect to the µ-XRF and µ-XRD results, the sum of the µ-XRF intensities shows distinct differences between the center region and the adjacent areas, as it is shown for a Sb_2Te_3 deposit in Figure 5.11A. The Sb_2Te_3 deposit shows higher sum intensities in the center than elsewhere and the opposite was found for Bi_2Te_3 deposits. Here the sum intensity in the center was lower (Figure 5.12A).

The changes in the overall intensity could be ascribed to variations of the thickness of the specimens. The thickness was calculated from the extinction of the fluorescence for Au obtained from the underlying 20 nm Au film, as described in the experimental section and determined with profilometry (supporting information). In Figure 5.11 a line profile of a Sb_2Te_3 deposit is shown. The absolute results have to be treated carefully. They do not represent an accurate thickness because the exact density ρ of the deposits is unknown and was calculated from the deposited elemental mass (determined by ICP-OES) and the volume determined roughly from the dimensions obtained by scanning electron microscopy (SEM) ($1.4\,gcm^{-3}$). Nonetheless, profilometry and absorption data give results in the same order of magnitude and show that the thickness of the areas is approximately 15 µm in the center of Sb_2Te_3 deposits and approximately 5 μm in other areas (for Bi_2Te_3 vice versa). With

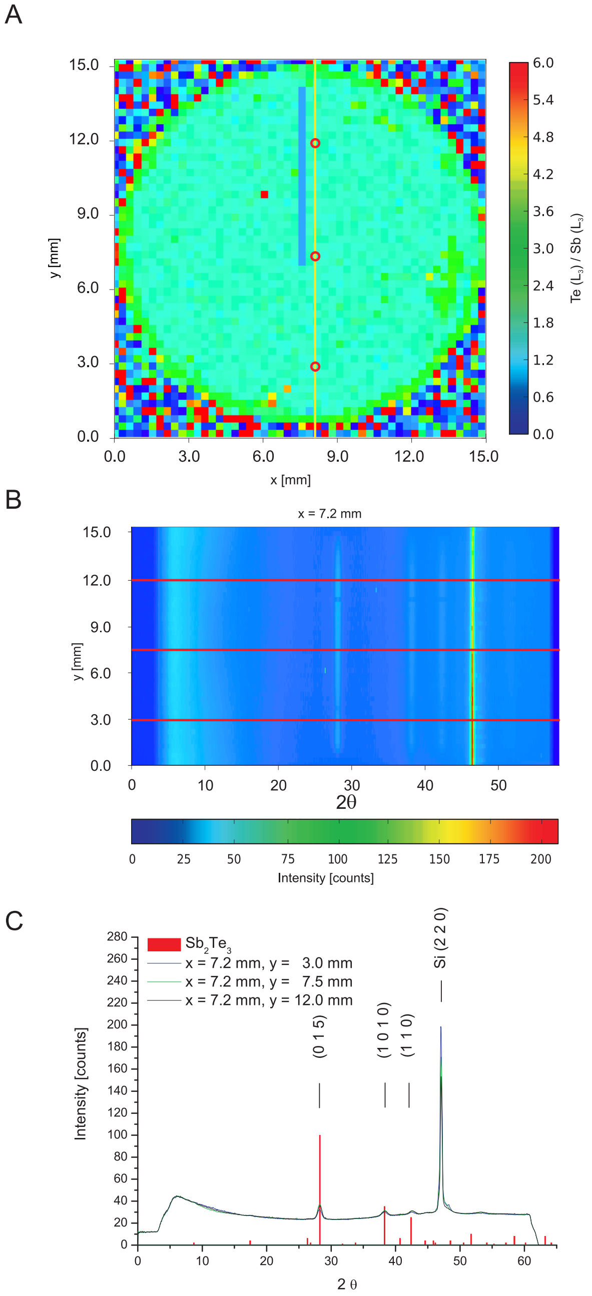

Figure 5.10: The ratio of the fluorescence for the Te(L3) line to the fluorescence of the Sb(L3) line at the surface area of an Sb_2Te_3 film on Au substrate. The blue line in the middle is due to a synchrotron refill time (A). µ-XRD line scan, which is marked in yellow in A and three individual spots are marked in red (B). µ-XRD of the three individual spots, marked in B (C)

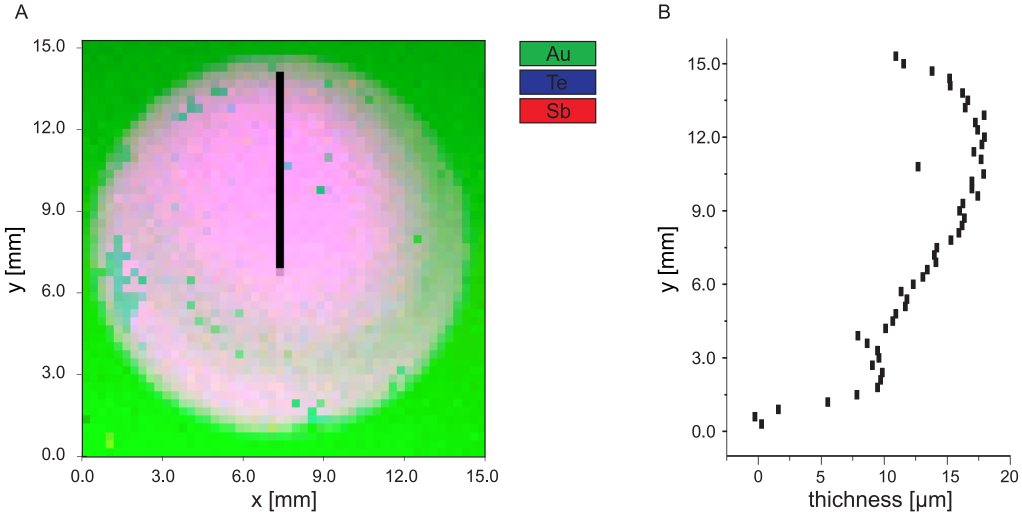

Figure 5.11: The sum of the Te(L3) and Sb(L3) fluorescence line intensities as distribution of the surface area over an Sb_2Te_3 film on Au substrate (A) (The black line in the middle is the result of a synchrotron injection time). Sample thickness line scan calculated from the Au(L) fluorescence absorption at a synchrotron radiation energy of 30 keV (B).

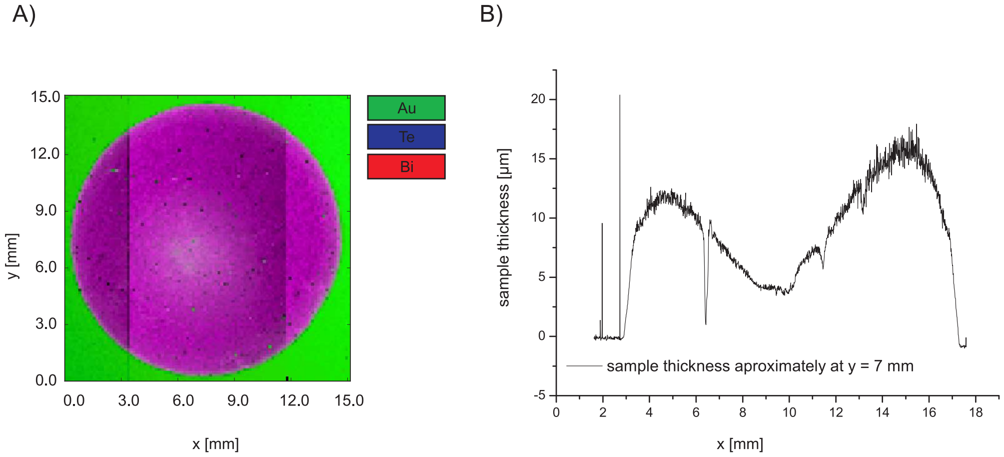

Figure 5.12: Homogeneous distribution of Bi and Te in Bi_2Te_3 (sample pon) and thickness calculation from the fluorescence for Au.

respect to the homogeneity similar results are found for a Bi_2Te_3 thermoelectric material. μ-XRF and μ-XRD analyses showed that the elements are homogeneously distributed over the surface, which was reflected by the measurements of the Te(L) and Bi(M) fluorescence line intensities and the structure data. In Figure 5.12 the mapping (5.12A) of the μ-XRF results and the calculated sample thickness for the Bi_2Te_3 sample (5.12B) are shown.

The ratio of the fluorescence for the Te(L3) line to the fluorescence of the Sb(L3) line was found to be 1.01 ± 0.004 (0.4%) over almost the whole deposit except at the rim of the deposit, where a decrease of the ratio to 0.8 ± 0.053 (6.6%) for the outermost $50\,\mu m$ was found (Figure 5.13).

As for the Sb_2Te_3 deposits the anisotropy with respect to the Seebeck coefficient matches the morphological profile of the sample. Thicker areas give a higher absolute value of the Seebeck coefficient S.

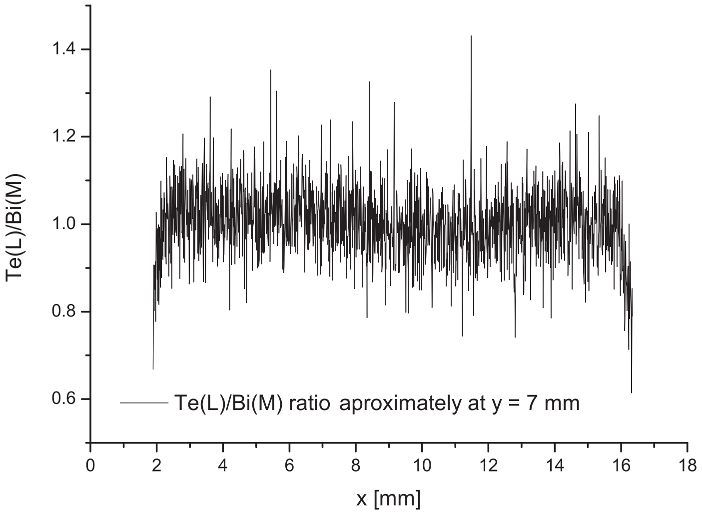

Figure 5.13: Homogeneous distribution of Bi and Te in Bi_2Te_3, as shown by the comparison of the Bi(M) and Te(L) fluorescence line intensity scans.

For completeness the findings on $Bi_{1.5}Sb_{0.5}Te_3$ and $Bi_2Te_{2.5}Se_{0.5}$ are presented in Figure 5.14. These materials were deposited on Pt substrates and the fluorescence lime intensities for the main components and the Pt(L3) fluorescence intensity are shown in the figures. For the $Bi_{1.5}Sb_{0.5}Te_3$ material variations of the sample thickness are obvious from the surface mapping in Figure 5.14A, where isolated regions of a strongly increased fluorescence for Pt can be found. Apart herefrom the distributions for the main components for both materials were found to be homogeneous.

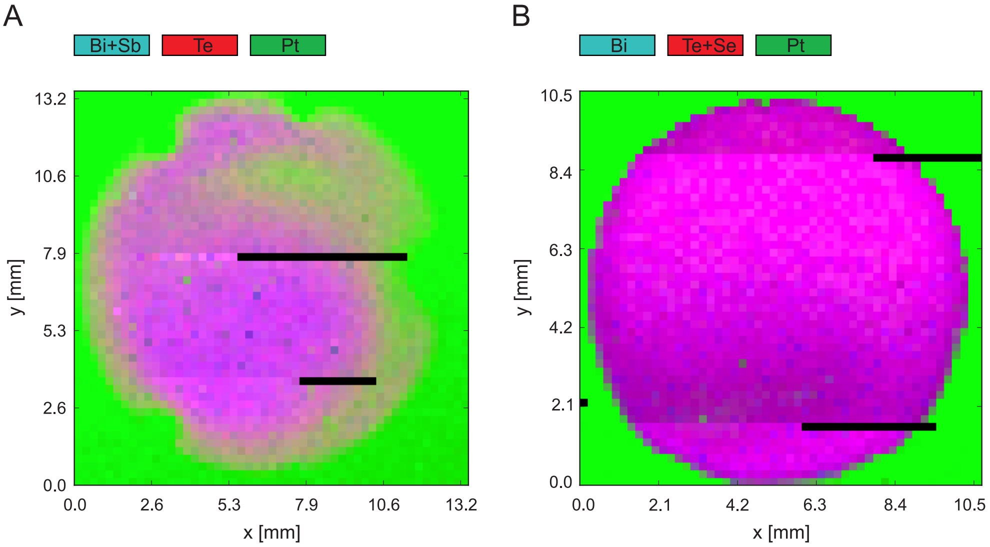

Figure 5.14: Mappings of the fluorescence line intensities for $Bi_{2-x}Sb_xTe_3$ and $Bi_2Te_{3-y}Se_y$ samples. The inhomogeniety can be attributed to variations of the thickness as it was found for the Bi_2Te_3 and Sb_2Te_3 samples.

For all samples it easily can be imagined that variations in the thickness of the deposits may be the result of the stirring of the solution during the deposition process. This could be changed by the use of a rotating disc electrode for stirring the solution, by which a laminar flow pattern could be obtained.

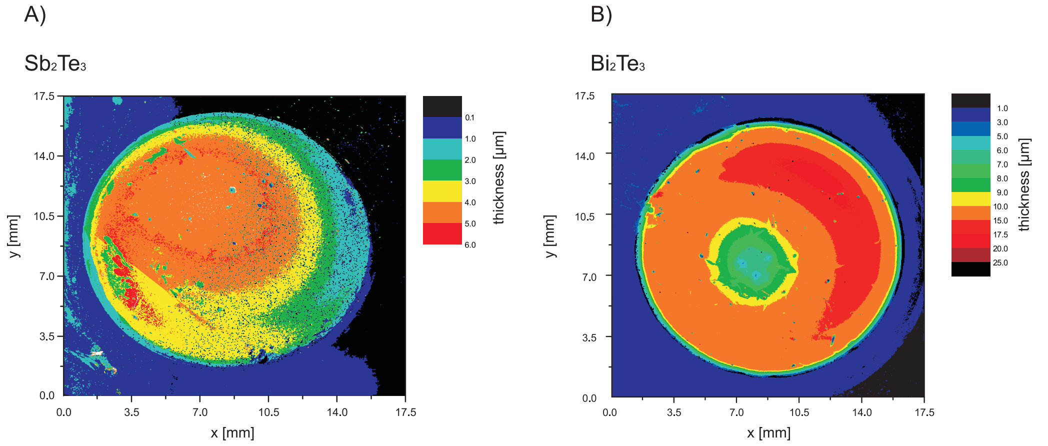

Figure 5.15: Sample thickness map determined with an optical profilometer of A: Sb_2Te_3 (sample 4910) and B: Bi_2Te_3 (sample pon).

5.4 X-ray absorption near edge structure using synchrotron radiation

In the case of the Bi_2Te_3 deposits µ-XANES experiments were performed at the edge of the Bi(L3) line so as to monitor possible anisotropies with respect to the valence of the main components in the material. As indicated in Figure 5.16, five XANES scans, were made at five locations on the sample and the results are given in Figure 5.16. The results show that the thinner part in the middle is slightly more oxidized than the thicker rim of the sample. It can be assumed that this is caused by an oxidized surface layer having constant thickness but of which the portion is of course larger in the thinner part of the deposit.

As references a bulk Bi_2Te_3 reference sample and $Bi(NO_3)_3$ were analyzed. The results show that despite Bi formally has a valence of III in both materials the edge of the nitrate is shifted significantly to higher energies because of the higher electro negativity of the NO_3^- ion. A comparison of the results for the electrochemically deposited material with the bulk Bi_2Te_3 shows that in the latter a slightly higher shift occures at the edge. As this material is less dense than the bulk, it is assumed that the oxidized surface layer is thicker than in the bulk which explains the shift. The larger shift for thinner sample areas can be explained by the constant oxide layer thickness, which is responsible for a higher amount of Bi atoms bound to O as compared to the Bi atoms bound to Te atoms in thinner regions of the sample. This contrasts with the thicker regions.

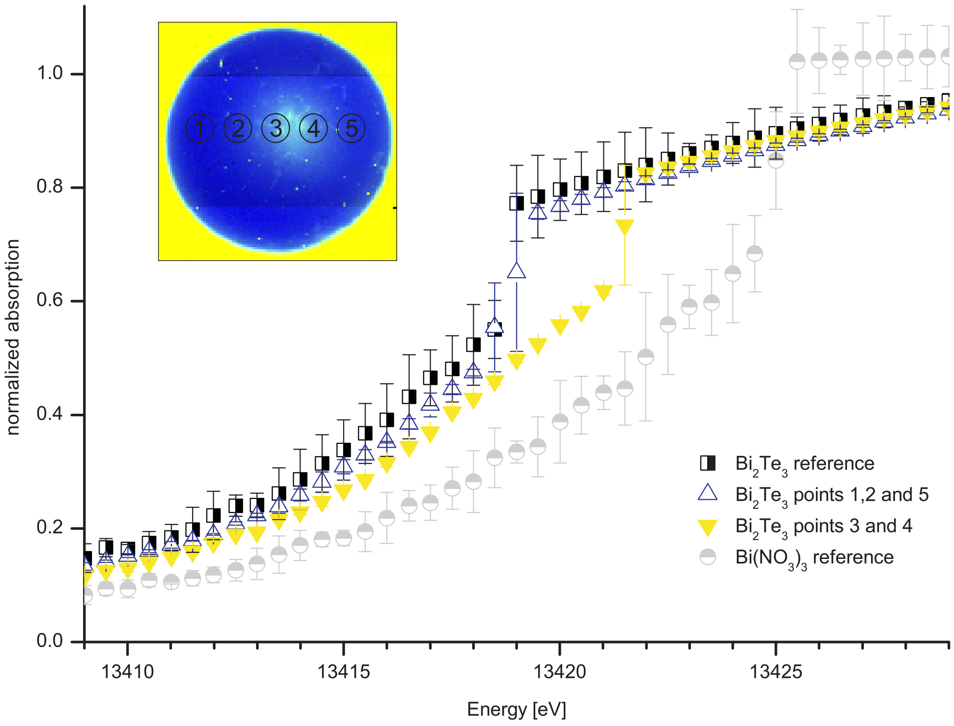

Figure 5.16: XANES measurements for the Bi_2Te_3 sample. The thinner part is slightly more oxidized.

5.5 Conclusions

GD-TOF-MS

GD-TOF-MS has been shown to be useful to determine the homogeneity of the deposition of thermoelectric materials based on Bi, Sb and Te deposited on Au and Cr coated Si wafers. The results were validated by a comparison with the results obtained with SIMS measurements at the same samples. With both methods it could be shown that the deposition was homogeneous. For the GD-TOF-MS and SIMS analyses depth resolutions have been determined and were found to strongly depend on the substrate and the measurement mode. While for the Sb_2Te_3 layers, depth resolutions of 3 µm were found with PP-TOFMS, the depth resolution within the Au, Cr and Si layers for the same sample was found to be below 80 nm. For the same sample the depth resolutions determined with SIMS were found to be between 250 nm and 40 nm. This may be attributed to the respective measured areas in the case of both methods, which is an essential parameter for relatively rough samples. For a Bi_2Te_3 sample all calculated depth resolutions obtained with GD-TOF-MS were between 530 nm and 200 nm. The large deviations are attributed to the relatively fragile character of the samples. For GD-TOF-MS and SIMS the sputtering rates have been found to be approximately 80 nm s^{-1} and 3 nm s^{-1}, which makes the use of GD-TOF-MS clearly more advantageous than to SIMS for the samples to be investigated. The precision of GD-TOF-MS has been investigated and found to be within 1.1% and 1.9% for measurements at one sample of Bi_2Te_3. This is lower than the standard deviation from measuring at three samples of the same material, which was found to be 3.6%. The same trend was found for the Sb_2Te_3 samples, for which the standard deviations in the case of one sample were found to be between 1.7% and 4.2%. The standard deviation for measurements at three Sb_2Te_3 samples was found to be 5.3%. From this result it can be concluded that the homogeneity within one sample is superior to the variability from one sample to another.

Syn-XRF, Syn-XRD, Syn-XANES

From the presented micro-analytical results the following conclusion can be drawn: the deposits are homogeneously distributed on the entire area with respect to their stoichiometry and structure. On deposits distinct height profiles with a thinner area in the middle of the sample were found in. In the case of the Bi_2Te_3 deposit and just the other way round for Sb_2Te_3. The thickness varies from approximately 15 µm at the highest point to ca. 5 µm at the lowest point. A higher valence of Bi was detected compared with the bulk material which is attributed to a slightly larger amount of surface oxidation layer of the less dense electrochemical deposits. The higher valence for Bi at the thinner parts of the specimens could be explained with the oxidized surface layer which contributes more to the overall valence at the thinner parts than at the thicker parts of the specimen.

Generally, the electrochemically deposited thermoelectrics can be characterized as homogeneous in stoichiometry and structure, being approximately 5 µm to 15 µm thick and having an oxidized surface layer deposited on a 20 nm Au layer.

With respect to these results it can be concluded that the variance of the Seebeck coefficient S is due to the layered structure of the specimen of the material. It can be assumed that in general all layers of the deposit including the 20 nm Au layer influences the Seebeck coefficient S. When a layer in a certain depth influences the Seebeck coefficient S, the latter will depend on the penetration depth of the heat applied by the PSM. The correlation of the Seebeck coefficient S with the thickness of the specimens indicates that the information depth of the PSM is close to the thickness of our specimens. This is supported by a calculation of the information volume of the S-probe analysis[115]. It was found that the areas with strong temperature gradient (5 K) penetrate more than 6 µm deep in the for bulk in the case of Bi_2Te_3 material. With such a penetration depth the influence of the Au layer would only be detectable in the thinner parts of the sample.

The higher amount of oxidation in the thinner parts of the sample and the possible Au influence of the Au layer in the same region indicate that the horizontal variations of the thickness are responsible for the lateral changes of the Seebeck coefficient S.

6 Stoichiometric characterization of thermoelectric nano-structures

6.1 Introduction

For the investigation of the composition of nanowires commonly SEM-EDS or TEM-EDS are used. Both have significant drawbacks. With TEM-EDS the accuracy for the analysis of deposited layers and nanowires was found to be in the range of 2 to 5 %[5]. Furthermore small amounts of nanowires have to be analyzed with TEM-EDS, for which the sample preparation is timeconsuming[43]. Both methods are not capable of realizing high-throughput analysis. They offer high resolution and therefore can be used for homogenety control purposes. Alternative methods are HR-GF-AAS and TXRF, which are both theoretically capable of performing direct solids sampling. Also ICP-MS, can be applied but this generally requires sample dissolution.

In Section 6.2 the applicability of HR-GF-AAS and TXRF to the analysis of nanowires after a preparation of slurry samples will be presented. In Section 6.3 the analysis of dissolved samples with ICP-MS will be described and the results compared with those of ICP-OES. Since the ICP-OES procedure was validated (compare Section 4.2) for layer samples and enabled the determination of concentrations in the low mg$\cdot$L^{-1} range after dissolution, this comparison will be used to show the applicability of ICP-MS analyses to samples with concentrations in the low µg$\cdot$L^{-1} range.

6.2 High resolution continuum source graphite furnace atomic absorption spectrometry

High resolution continuum source graphite furnace atomic absorption spectrometry (HR-CS-GF-AAS offers a series of possibilities over the classical line source atomic absorption spectrometry (LS AAS). Whereas in conventional LS AAS the absorbance only can be measured at the analytical wavelength as a function of time, the use of a CCD detector in HR-CS-GF-AAS adds the wavelength as a third dimension, which has several important advantages.

Under the use of a Xe short arc lamp as continuum primary radiation source a flexible correction for structured molecular background at freely chosen wavelengths is possible. Signals, which are simultaneously measured with the analytical line signal can be subtracted because of a high spectral resolution[80].

An increase of the linear dynamic ranges as a result of the widely differing element sensitivities at the respective pixels can be realized, when not only the absorbance at the line maximum but also the absorbance at a wavelength in the peak wing is measured[81].

Due to the fact that the Xe short arc lamp emits a continuous spectrum from 185 nm to 900 nm sequential multielement determinations are possible with a single primary radiation source instead of switching from one element selective lamp to another, as in conventional line-source AAS[81].

Simultaneous multielement determinations are possible in the cases that the analytical wavelengths of the respective elements lie within a single wavelength window of the CCD, which because of the required spectral resolution is of a few hundred pm only (400 pm at 200 nm), so that it cannot be expected to be the case for the three elements under investigation with graphite furnace atomization[116]. With the flame as atomizing unit a fast sequential determination of 10 to 15 elements per minute is possible[81].

6.2.1 Background correction

The spectral interference of the Te 214.2814 nm line with NO molecular bands in AAS is well known from the literature[117]. A correction for this spectral interference can easily be realized in HR-CS-GF-AAS. For this aim a reference absorption spectrum of blank solution is recorded and this is subtracted from the wavelength and time resolved absorption spectrum for the samples. Both spectral records are treated with a least squares algorithm, which is implemented in the software of the instrument[118].

6.2.2 Linear dynamic range

By an appropriate choice of pixels an expansion of the linear range to more than five orders of magnitude was found to be possible for Sb and Te. For Bi saturation was reached in the case of all pixels at a concentration of $3\,\mathrm{mg}\cdot\,\mathrm{L}^{-1}$. In Figure 6.2 the calibration curves for measurements with pixels, in which the signal is maximum, and curves for the case of pixels located at wavelengths in the wings of the line profiles for the elements determined are shown. In Table 6.1 the linear dynamic ranges and the correlation coefficients for the related calibrations are given. For trace analysis mostly the 100-102 pixel range, which is located at ±1 pixel away from the peak maximum (set at 101), is chosen for a calibration, since here the sensitivity obtained is maximum. In order to measure at a lower sensitivity an addition of pixels at the left and right side of the absorbance peak maximum is usually made (e.g. 99+103 or 98+104), by which the working range is expanded. In Figure 6.3 the absorbance signal for the Sb 217.5815 nm line in the case of a solution of $100\,\mathrm{mg}\cdot\,\mathrm{L}^{-1}$ of Sb is shown. It was found that the linear dynamic range could be increased by a summation of pixels located further in the wings of the absorbance signal, as it is described in the literature[116,117]. However, the calibration curves get broader error bars and this might ultimately limit the possibility of a linearization of the calibration curves by making use of signals from those pixels.

6.2.3 Comparison of high resolution continuum source graphite furnace atomic absorption spectrometry and total reflection X-ray fluorescence results

In order to investigate the accuracy of the results of HR-CS-GF-AAS for the determination of Bi, Sb and Te in slurries of nanowires the samples also have been analyzed with the aid of TXRF, which is known to need little sample preparation and to have a very low sample consumption.

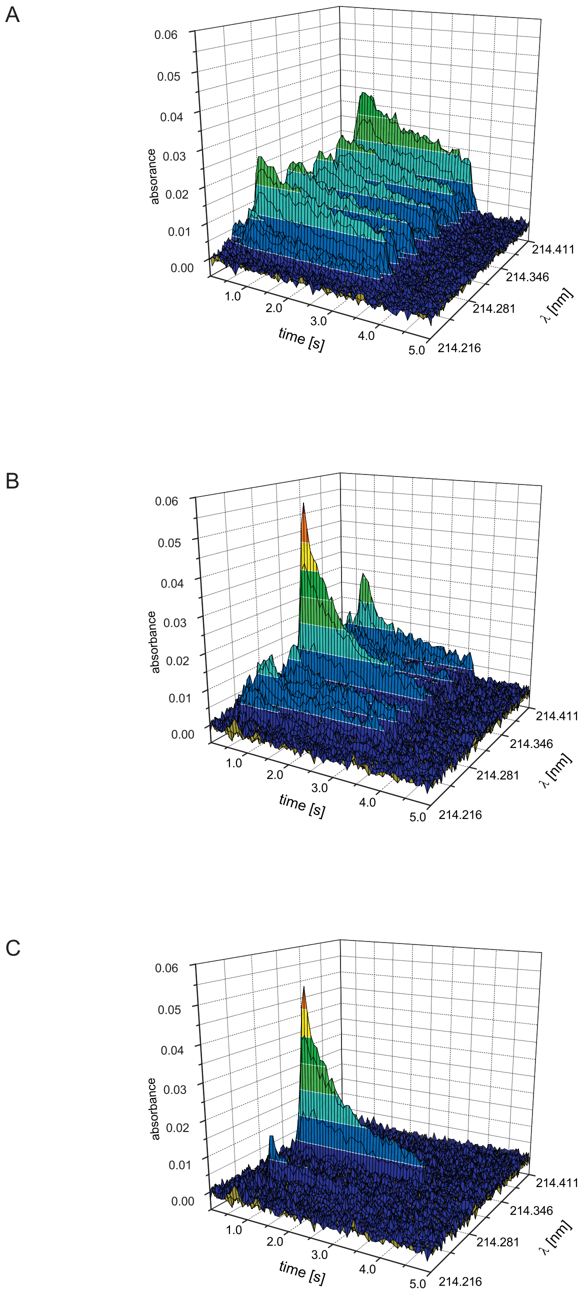

Figure 6.1: Background correction for the Te 214.2814 nm line. A: Time resolved background absorbance spectrum, B: Time resolved absorbance for a sample containing 1.5 ng of Te. C: Time resolved absorbance for a sample containing 1.5 ng of Te after background correction.

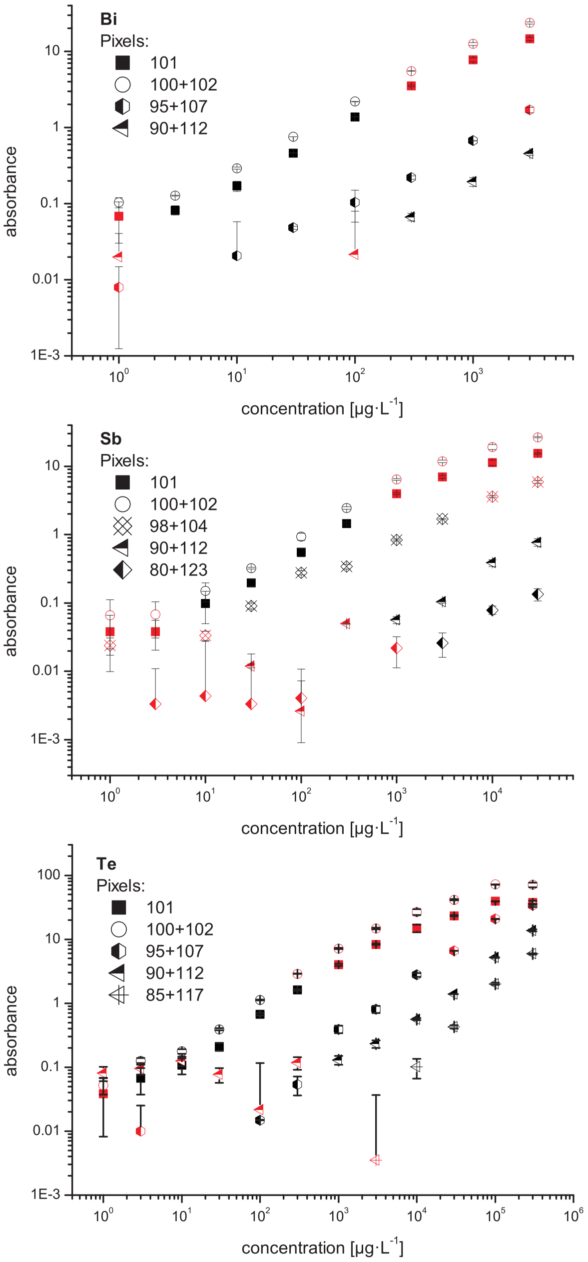

Figure 6.2: Linear dynamic ranges in HR-CS-GF-AAS for Bi, Sb and Te in the case of an optimized selection of measurement pixels and pixel areas.

Table 6.1: Linear dynamic ranges and sensitivities obtained in HR-CS-GF-AAS using standard solutions for Sb, Te and Bi when measuring at optimized pixels or with optimized pixel areas.

Element	Pixel	Linear dynamic range	R^2	Sensitivity $[E/\mu g\,L^{-1}]$
Sb	101	$10\,\mu g\,L^{-1}$ - $0.3\,mg\,L^{-1}$	0.9993	$4.68 \cdot 10^{-3}$
	100+102	$10\,\mu g\,L^{-1}$ - $0.3\,mg\,L^{-1}$	0.9991	$7.95 \cdot 10^{-3}$
	98+104	$30\,\mu g\,L^{-1}$ - $3\,mg\,L^{-1}$	0.9809	$5.18 \cdot 10^{-4}$
	90+112	$1\,mg\,L^{-1}$ - $300\,mg\,L^{-1}$	0.9962	$3.34 \cdot 10^{-5}$
	80+122	$3\,mg\,L^{-1}$ - $300\,mg\,L^{-1}$	0.9860	$8.45 \cdot 10^{-6}$
Te	101	$3\,\mu g\,L^{-1}$ - $0.3\,mg\,L^{-1}$	0.9952	$5.22 \cdot 10^{-3}$
	100+102	$3\,\mu g\,L^{-1}$ - $0.1\,mg\,L^{-1}$	0.9996	$1.04 \cdot 10^{-3}$
	95+107	$0.1\,mg\,L^{-1}$ - $10\,mg\,L^{-1}$	0.9972	$2.79 \cdot 10^{-4}$
	90+112	$0.3\,mg\,L^{-1}$ - $30\,mg\,L^{-1}$	0.9982	$4.58 \cdot 10^{-5}$
	85+117	$3\,mg\,L^{-1}$ - $300\,mg\,L^{-1}$	0.9992	$2.01 \cdot 10^{-5}$
Bi	101	$3\,\mu g\,L^{-1}$ - $0.1\,mg\,L^{-1}$	0.9996	$1.77 \cdot 10^{-4}$
	100+102	$3\,\mu g\,L^{-1}$ - $0.1\,mg\,L^{-1}$	0.9994	$3.06 \cdot 10^{-4}$
	95+107	$10\,\mu g\,L^{-1}$ - $0.1\,mg\,L^{-1}$	0.9989	$1.23 \cdot 10^{-5}$
	90+112	$30\,mg\,L^{-1}$ - $0.3\,mg\,L^{-1}$	0.9945	$1.06 \cdot 10^{-5}$

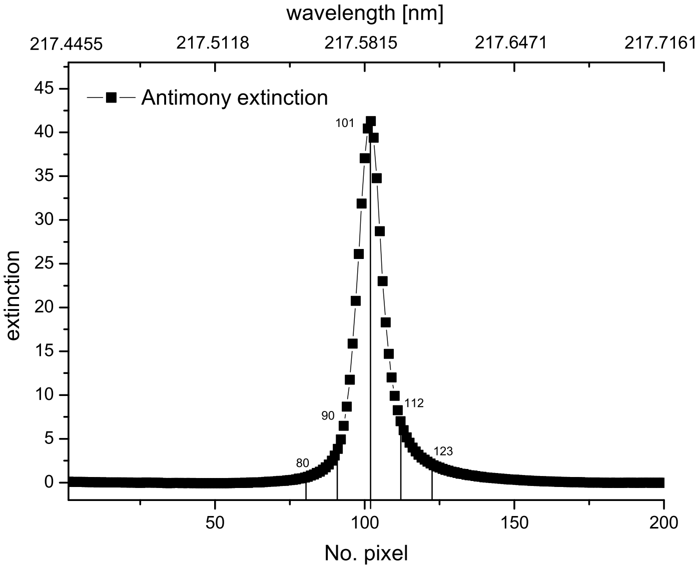

Figure 6.3: Selection of pixels for line and spectral background absorption measurements at the example of the Sb217.5815 nm line.

Only for three of the five samples the results of analysis for the nanowire slurry samples obtained by HR-CS-GF-AAS could be compared with those of TXRF. This is due to the limits of detection of TXRF (6.2) and the amounts of material in the sample slurries. It was found that the results of analysis of both methods well agree with each other for samples 1 and 2 but not for sample 3. This might be due to an overlap of the Sb and Te signals in X-ray fluorescence and to a possible interference with the Ca fluorescence signal as well. Only for higher concentrations the Ca interference, which presumably stems from a contamination of the solvent for the nanowires, is negligible. For the lowest concentrations the Ca interference rules out any quantification.

Table 6.2: Comparison of the results of HR-CS-GF-AAS and TXRF in the analysis of nanowire samples.

	HR-CS-GFAAS			TXRF		
No. (Type)	% Bi	% Sb	% Te	% Bi	% Sb	% Te
1. (Bi_2Te_3)	52.7 ± 2.1	-	47.3 ± 2.2	48.9 ± 0.2	-	51.1 ± 0.2
2. (Bi_2Te_3)	36.4 ± 1.1	-	63.6 ± 2.6	37.2 ± 0.1	-	62.8 ± 0.1
3. (Sb_2Te_3)	-	34.0 ± 0.5	66.0 ± 1.8	-	25.3 ± 0.2	74.7 ± 0.1
4. (Sb_2Te_3)	-	30.2 ± 0.5	69.8 ± 2.5	-	n.d.	n.d.
5. (Bi_2Te_3)	83.3 ± 5.7	16.7 ± 4.4	-	n.d.	n.d.	-

6.3 Inductively coupled plasma mass spectrometry

Also the possibilities to analyze nano-structured samples with inductively coupled plasma mass spectrometry (ICP-MS) were evaluated. For testing layer samples were dissolved according to the procedure applied in ICP-OES (compare 3.2). The dilution of the samples were, where necessary, adjusted to fit in the calibration range of ICP-MS, being from 10 $\mathrm{ng \cdot L^{-1}}$ to 100 $\mathrm{\mu g \cdot L^{-1}}$

Since a precise determination of the main components with standard deviations lower than 1% for nano-structured materials is necessary as it is for layer samples (compare 4.2) the standard LOD for the isotopes ^{82}Se, ^{121}Sb, ^{130}Te and ^{209}Bi were determined according to Equations 4.11.

Table 6.3: LOD for ICP-MS.

Isotope	LOD [$\mathrm{ng \cdot L^{-1}}$]
^{82}Se	29
^{121}Sb	5.5
^{130}Te	23
^{209}Bi	8.8

Since the LOD values are roughly a factor 1000 lower than those obtained for ICP-OES under optimized conditions the ICP-MS appears to be more suitable for the quantification of the main components in nanowire samples, where the sample amount is the limiting factor.

To compare the accuracy of the ICP-OES and ICP-MS methods measurements with layer samples were carried out and the correlation of the results investigated.

A good agreement between the main component concentrations determined with ICP-OES and ICP-MS for the samples was found. The linear regression of the results obtained with ICP-MS versus the results of ICP-MS is presented in Figure 6.4 and the correlation coefficients are 0.989 for Sb, 0.992 for Te and 0.998 for Bi. Taking into account that the detection limits for ICP-MS are considerably lower then those obtained with ICP-OES (compare table 4.1 the quantification of main components in nanowires is most certainly possible with ICP-MS after dissolving the samples.

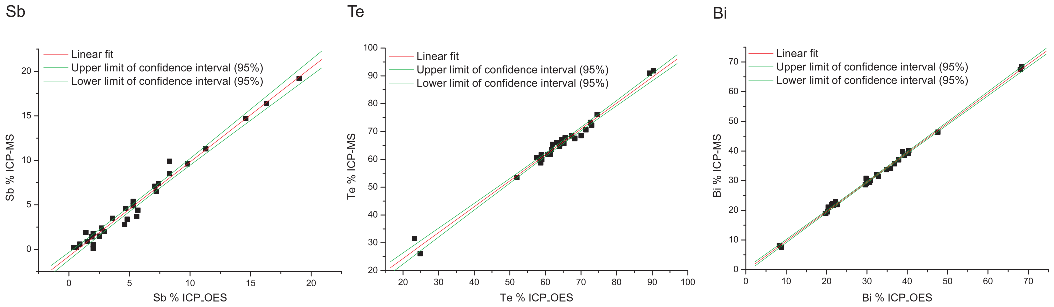

Figure 6.4: Correlation of ICP-MS and ICP-OES results for the determination of main components in $Bi_{2-x}Sb_xTe_3$.

6.4 Conclusions

The results of HR-CS-GF-AAS and TXRF well agree but the analytical errors were larger than the standard deviation intervals. This is certainly due to the low number of measurements, namely only two for HR-CS-GF-AAS and three for TXRF. A larger number of measurements might improve the agreement but the low amounts of sample available for this study were the limiting factor. As both methods rely on different physical phenomena for the quantification, systematical errors widely can be ruled out, keeping in mind that both methods involve almost no sample preparation and that therefore they are relatively free of risks of contamination.

As it was found that the TXRF suffers from matrix effects and therefore the LODs are high in many cases it was found to be not a suitable method for the analysis of nano-structured samples. Further HR-CS-GF AAS was found to suffer from quite high standard deviations, such as values up to 2.6 at.% for the main components. (see Table 6.2). Although this is a good standard deviation for nano-structured samples, when comparing to values reported in the literature[30] for nano-stuctured samples (compare chapter 1.1) from an analytical point of view lower standard deviations should be obtainable. An analysis with dissolved samples and ICP-MS was therfore evaluated and shown to be capable of precise analyses with standard deviations below 1% above a concentration of 0.48 $\mu g \cdot L^{-1}$ for Sb and above 2.6 $\mu g \cdot L^{-1}$ for Se. With a sample consumption of 2.5 mL this means that absolute limits of detection are in the range of 0.02 to 0.1 ng, which is as good or better than in HR-CS-GF-AAS.

Although sample dissolution involves the risk of contaminations the dissolution of nano-structured samples and analysis with ICP-MS appears to be a suitable choice for future work.

7 Summary

In this work a procedure based on ICP-OES has been developed for the precise determination of the main components of thermoelectric layer samples. Relative confidence intervals down to 0.2% have been achieved (compare Tables 4.2 and 4.3). This is low enough to detect deviations from the optimum stoichiometry, which would lead to a significant decrease in thermoelectric performance (compare Figure 4.10).

With XRD it could be shown that in dependence on the deposition conditions the material structures can be significantly improved. Crystallite sizes can be increased by a factor of 5 from 120 nm for layers deposited at direct current conditions to 600 nm for samples deposited at pulsed current conditions[5] (compare Table 4.10).

As bulk impurities the elements Ca, Cu, Fe, K, Mg, Na, Ni and Zn could be determined as contaminations in concentrations down to 0.1 μg$\cdot$ L^{-1} (compare Table 4.5). With the developed ICP-OES procedure it is accordingly possible to determine contaminations and exclude unwanted doping for the deposited samples.

To control the vertical homogeneity of deposited samples GD-TOF-MS could be used successfully. The results of GD-TOF-MS results show that the deposits are homogeneous (compare Figure 5.3) and these results were in agreement with those of SIMS (compare Figure 5.4). As expected it was found that GD-TOF-MS measurements require less measurement time for obtaining the same depth resolutions as SIMS. Depth resolutions down to 50 nm were achieved at a sputtering rate of 80 nm$\cdot$s^{-1} (compare Tables 5.1 and 5.2).

Synchrotron µXRF and µXRD revealed that the depositions laterally were homogeneous with respect to stoichiometry and structure in contrast to the results of PSM (compare Section 5.3). Here it was possible to show that the results of PSM measurements depend on the thickness of the deposited layer on the Si wafer. This was theoretically not expected and this dependence on the layer thickness was attributed to the penetration depth of the heat, which is applied for the PSM measurement (compare Section 2.5). This shows the limitations of PSM measurements and it is made clear that care must be taken for the interpretation of mappings of the Seebeck coefficient S, which are routinely used for homogeneity control purposes in the field of thermoelectrics (compare chapter 1.1). Furthermore, with XANES it could be shown that there is an oxidized surface layer on the thermoelectric layers (compare Figure 5.16). For later productions here more care should be taken concerning handling of the samples in open air.

In summary good Seebeck coefficient values of 160 $\mu V \cdot K^{-1}$ for Sb_2Te_3 and -45 $\mu V \cdot K^{-1}$ for Bi_2Te_3 could be achieved thanks to the use of a precisely controlled stoichiometry and homogeneity, as shown by the results in Figure 4.10 and Figure 5.9.

For future research nano-structured thermoelectric materials are promising. In chapter 6 the application of three methods for their characterization, namely HR-GF-AAS, TXRF and ICP-MS were evaluated. In principle all three methods are applicable although TXRF suffers from matrix effects and the low sample amounts available. HR-CS-GF-AAS enables correct determinations but the standard deviations are still high. In future ICP-MS should be the method of choice for the analysis of nano-structured samples, as here sample amounts down to 10 ng per element can be used and a standard deviation of 1% still can be reached. This is due to the fact that the limits of detection are lower than in ICP-OES by a factor of 100 (compare Table 6.3).

8 Zusammenfassung

Im Rahmen dieser Arbeit wurde ein Verfahren auf der Basis von ICP-OES für die präzise Bestimmung der Hauptbestandteile von thermoelektrischen Proben, welche elektrochemisch abgeschieden wurden, entwickelt. Reelative Vertrauensintervalle bis zu 0.2% konnten für die Analysenergebnisse erreicht werden (vergleiche die Tabellen 4.2 und 4.3). Dies ist genügend gut um Abweichungen von der angestrebten optimalen Stöchiometrie feststellen zu können. Diese Abweichungen würden zu einem signifikanten Verlust an thermoelektrischer Leistungsfähigkeit führen (vergleiche Abbildung4.10).

Mittels XRD konnte gezeigt werden, dass die Kristallstrukturen der thermoelektrischen Materialien durch Optimierung der Bedingungen der elektrochemischen Abscheidung signifikant verbessert werden können. Die Kristallitgröße konnte durch einen Wechsel von konstantem Abscheidepotential zu gepulsten Abscheidepotentialen um einen Faktor 5 von 120 nm auf 600 nm gesteigert werden[5] (vergleiche Tabelle 4.10).

Als Verunreinigungen wurden die Elemente Ca, Cu, Fe, K, Mg, Na, Ni, und Zn gefunden. Dabei konnten Konzentrationen bis hinunter zu 0.1 $\mu g \cdot L^{-1}$ (vergleiche Tabelle 4.5) bestimmt werden. Mit Hilfe eines ICP-MS Verfahrens ist es also möglich Verunreinigungen zu bestimmen und ungewollte Dotierungen der elektrochemisch abgeschiedenen Porben auszuschließen.

Um die vertikale Homogenität der elektrochemisch abgeschiedenen thermoelektrischen Materialien nachzuweisen wurden Messungen mit GD-TOF-MS durchgeführt. Die Ergebnisse der GD-TOF-MS zeigten, dass homogene Abscheidungen vorlagen (vergleiche Abbildung 5.3). Den Erwartungen entsprechend konnte gezeigt werden, dass die GD-TOF-MS Messungen weniger Zeit in Anspruch nehmen, als Messungen mit SIMS, welche vergleichbare Tiefenauflösungen zulassen. Tiefenauflösungen bis zu 50 nm hinunter konnten bei einer Sputterrate von 80 $nm \cdot s^{-1}$ erreicht werden (vergleiche die Tabellen 5.1 und 5.2).

Mit synchrotron-angeregter µXRF und µXRD Untersuchungen konnte die laterale Homogenität von elektrochemisch abgeschiedenen thermoelektrischen Materialien bezüglich ihrer Stöchiometrie und Struktur nachgewiesen werden. Dies steht im Gegensatz zu den Ergebnissen von PSM Untersuchungen (vergleiche Abschnitt 5.3). Es war möglich die Abhängigkeit der PSM Messungen von der Dicke der auf dem Si Wafer abgeschiedenen Schicht nachzuweisen. Diese theoretisch nicht zu erwartendende Tatsache wurde auf die Eindringtiefe der Hitze, welche zur Bestimmung des Seebeck Wertes auf an die Probe abgegeben wird, zurückgeführt (vergleiche Abschnitt 2.5). PSM Messungen werden häufig zur ortsaufgelösten Bestimmung des Seebeck Wertes von thermoelektrischen Materialien benutzt (vergleiche Kapitel 1.1). Die Ergebnisse dieser Arbeit zeigen die Grenzen der PSM Methode und macht deutlich, dass bei der Interpretation von PSM Messergebnissen Vorsicht geboten ist. Darüber hinaus konnte mit XANES gezeigt werden, dass sich auf der Oberfläche von elektrochemisch abgeschiedenen thermoelektrischen Schichten eine Oxidschicht bildet (vergleiche Abbildung 5.16). Daher sollte in Zukunft bei der Präparation der Schichten größere Vorsicht bei der Synthese und der Lagerung der Proben an Luft angewendet werden.

Es wurden gute Werte für die Seebeck Koeffizienten von 160 $\mu V \cdot K^{-1}$ im Falle des Sb_2Te_3 und -45 $\mu V \cdot K^{-1}$ im Falle des Bi_2Te_3 erreicht. Dies war möglich aufgrund der präzisen Kontrolle der Stöchiometrie und Homogenität. Dies zeigen die Ergebnisse, welche in den Abbildungen 4.10 und 5.9 wiedergegeben werden.

In der Zukunft werden nano-stukturierte thermoelektrische Materialien aufgrund ihrer vielversprechenden Eigenschaften sicherlich weiter erforscht werden. In Kapitel 6 wurde daher die Anwendung der Methoden HR-CS-GF-AAS, TXRF und ICP-MS zu ihrer Charakterisierung untersucht. Alle sollten anwendbar sein, obwohl die TXRF leicht von Matrixeffekten beeinträchtigt wird und die Probenmengen für die TXRF oft zu niedrig sind. Die HR-CS-GF-AAS ermöglicht die richtige Bestimmung der in den Materialen vorhandenen Hauptbestand-teilen, aber die Standardabweichungen sind verhältnismäßig hoch. In der Zukunft sollte ein ICP-MS Verfahren für die Analyse von nano-strukturierten thermoelektrischen Materialien genutzt werden. Probenmengen von bis zu 10 ng pro Element könnten dann mit Standardabweichungen von 1% bestimmt werden. Dies ergibt sich aufgrund der Tatsache, dass die Nachweisgrenzen der ICP-MS leicht um einen Faktor 100 niedriger sein können als die der ICP-OES (vergleiche Tabelle 6.3).

Bibliography

[1] Sommerlatte, J.; Nielsch, K.; Böttner, H. *Physik J.* **2007**, *6*, 35–41.

[2] Rowe, D. M., Ed. *Handbook of Thermoelectrics*; CRC Press: Boca Raton, **1995**.

[3] Magri, P.; Boulanger, C.; Lecuire, J.-M. *J. Mater. Chem.* **1996**, *6*, 773–779.

[4] Yim, W. M.; Amith, A. *Solid State Electron.* **1972**, *15*, 1141–1165.

[5] Schumacher, C. *Pulsed Electrodeposited p- and n-Doped Chalcogenide Semiconductors for Thermoelectric Applications: From Films to Nanowires*. Ph.D. thesis, Universität Hamburg, Fachbereich Physik, **2012**.

[6] Bassi, A. L.; Bailini, A.; Casari, C. S.; Donati, F.; Mantegazza, A.; Passoni, M.; Russo, V.; Bottani, C. E. *J. Appl. Phys.* **2009**, *105*, 124307.

[7] Li, M. S., S.; Toprak; Soliman, J., H. M. A.; Zhou; Muhammed, M.; Platzek, D.; Müller, E. *Chem. Mater.* **2006**, *18*, 3627–3633.

[8] Glatz, W.; Durrer, L.; Schwyter, E.; Hierold, C. *Electrochim. Acta* **2008**, *54*, 755 – 762.

[9] Glatz, W.; Schwyter, E.; Durrer, L.; Hierold, C. *J. Microelectromech. Syst.* **2009**, *18*, 763 –772.

[10] Takahashi, M.; Kojima, M.; Sato, S.; Ohnisi, N.; Nishiwaki, A.; Wakita, K.; Miyuki, T.; Ikeda, S.; Muramatsu, Y. *J. Appl. Phys.* **2004**, *96*, 5582–5587.

[11] Kim, M.-Y.; Oh, T.-S. *J. Electron. Mater.* **2009**, *38*, 1176–1181.

[12] Kim, M.-J.; Oh, T.-S. *Mater. T. JIM* **2010**, *51*, 1909–1913.

[13] Li, S.; Soliman, H. M. A.; Zhou, J.; Toprak, M. S.; Muhammed, D., M.; Platzek; Ziolkowski, P.; Müller, E. *Chem. Mater.* **2008**, *20*, 4403–4410.

[14] Li, X.; Koukharenko, E.; Nandhakumar, I. S.; Tudor, J.; Beeby, S. P.; White, N. M. *PhysChemChemPhys* **2009**, *11*, 3584–3590.

[15] Rostek, V., R.;and Sklyarenko; Woias, P. *J. Mater. Res.* **2011**, *26*, 1785–1790.

[16] Venkatasubramanian, R.; Siivola, E.; T.;, C.; O'Quinn, B. *Nature* **2001**, *413*, 597–602.

[17] Harman, T. C.; Taylor, P. J.; Walsh, M. P.; LaForge, B. E. *Science* **2002**, *297*, 2229–2232.

[18] Jin, C.; Xiang, X.; Jia, C.; Liu, W.; Cai, W.; Yao, L.; Li, X. *J. Phys. Chem. B* **2004**, *108*, 1844–1847.

[19] Prieto, A. L.; Sander, M. S.; Martín-González, M. S.; Gronsky, R.; Sands, T.; Stacy, A. M. *J. Am. Chem. Soc.* **2001**, *123*, 7160–7161.

[20] Sander, M. S.; Gronsky, R.; Sands, T.; Stacy, A. M. *Chem. Mater.* **2003**, *15*, 335–339.

[21] Jang, M. H.; Park, S. J.; Lim, D. H.; Park, S. J.; Cho, M.-H.; Ko, D.-H.; Heo, M. Y.; Sohn, H. S.; Kim, S.-O. *Appl. Phys. Lett.* **2010**, *95*, 052112.

[22] Park, K.; Xiao, F.; Yoo, B. Y.; Rheem, Y.; V.;, M. N. *J. Alloys Compd.* **2009**, *485*, 362 – 366.

[23] Qiu, W. J.; Yang, S. H.; Zhu, T. J.; Xie, J.; Zhao, X. B. *J Electron. Mater.* **2011**, *40*, 1506–1511.

[24] Kim, S. I.; Ahn, K.; Yeon, D.-H.; Hwang, S.; Kim, H.-S.; Lee, S. M.; Lee, K. H. *Appl. Phys. Express* **2011**, *4*, 091801.

[25] Lim, S.-K.; Kim, M.-Y.; Oh, T.-S. *Thin Solid Films* **2009**, *517*, 4199 – 4203, Proceedings "of the 1st International Conference on Microelectronics and Plasma Technology" (ICMAP 2008).

[26] Tittes, K.; Plieth, W. *J. Solid State Electr.* **2007**, *11*, 155–164.

[27] Xiao, F.; Yoo, B.; Lee, K.-H.; Myung, N. V. *Nanotechnol.* **2007**, *18*, 335203.

[28] Bu, L.; Wang, W.; Wang, H. *Mater. Res. Bull.* **2008**, *43*, 1808 – 1813.

[29] Del Frari, D.; Diliberto, S.; Stein, N.; Boulanger, C.; Lecuire, J.-M. *J. Appl. Electrochem.* **2006**, *36*, 449–454.

[30] Martín-González, M.; Snyder, G. J.; Prieto, A. L.; Gronsky, R.; Sands, T.; Stacy, A. M. *Nano Lett.* **2003**, *3*, 973–977.

[31] Michel, S.; Stein, N.; Schneider, M.; Boulanger, C.; Lecuire, J.-M. *J. Appl. Electr.* **2003**, *33*, 23–27.

[32] Michel, S.; Diliberto, S.; Stein, N.; Bolle, B.; Boulanger, C. *J. Solid State Electrochem.* **2008**, *12*, 95–101.

[33] Zimmer, A.; Stein, N.; Terryn, H.; Boulanger, C. *J. Phys. Chem. Solids* **2007**, *68*, 1902 – 1907.

[34] Fleurial, J.; Gailliard, L.; Triboulet, R.; Scherrer, H.; Scherrer, S. *J. Phys. Chem. Solids* **1988**, *49*, 1237 – 1247.

[35] Kuleshova, J.; Koukharenko, E.; Li, X.; Frety, N.; Nandhakumar, I. S.; Tudor, J.; Beeby, S. P.; White, N. M. *Langmuir* **2010**, *26*, 16980–16985.

[36] Broekaert, J. A. C. *Analytical Atomic Spectrometry with Flames and Plasmas*, 2nd ed.; Wiley-VCH: Weinheim, **2005**.

[37] Hill, S. J., Ed. *Inductively Coupled Plasma Spectrometry and its Applications*, 2nd ed.; Blackwell Publishing: Oxford, **2007**.

[38] Marcus, R. K., Broekaert, J. A. C., Eds. *Glow discharge plasmas in analytical spectroscopy*; Wiley-VCH: Chichester, **2003**.

[39] Cresser, M. S.; Ebdon, L. C.; Mcleod, C. W.; Buridge, J. C. *J. Anal. At. Spectrom.* **1986**, *1*, R1–R17.

[40] Brown, A. A.; Halls, D. J.; Taylor, A. *J. Anal. At. Spectrom.* **1986**, *1*, 29R–44R.

[41] Littlejohn, D.; Ellis, H. J.; Hughes, H. *J. Anal. At. Spectrom.* **1986**, *1*, 87R–106R.

[42] Hickman, D. A.; Rooke, J. M.; Thompson, M. *J. Anal. At. Spectrom.* **1986**, *1*, 169R–192R.

[43] Peranio, N.; Eibl, O. *Phys. Stat. Sol.* **2007**, *204*, 3243–3255.

[44] Bjeoumikhov, A.; Arkadiev, V.; Eggert, F.; Hodoroaba, V.-D.; Langhoff, N.; Procop, M.; Rabe, J.; Wedell, R. *X-ray Spectrom.* **2005**, *34*, 493–497.

[45] Haschke, M.; Eggert, F.; Elam, W. T. *X-Ray Spectrometry* **2007**, *36*, 254–259.

[46] PSM - Potential-Seebeck Microprobe. `http://www.panco.de/downloads/PSM_engl_LOT.pdf`, 09.03.2013.

[47] Platzek, D.; Karpinski, G.; Stiewe, C.; Ziolkowski, P.; Drasar, C.; Müller, E. *IEEE* **2005**, *International Conference on Thermoelectrics*, 13–16.

[48] Reinsberg, K.-G.; Schumacher, C.; Nielsch, K.; Broekaert, J. A. C. *J. Anal. At. Spectrom.* **2011**, *26*, 2477–2482.

[49] Reinsberg, K.-G.; Schumacher, C.; Tempez, A.; Nielsch, K.; Broekaert, J. A. C. *Spectrochim. Acta Part B* **2012**, *76*, 175 – 180.

[50] Reinsberg, K.-G.; Schumacher, C.; Zastrow, S.; Nielsch, K.; Broekaert, J. A. C.; Fittschen, U. E. A. *J. Mater. Chem. A* **2013**, *1*, 4215–4220.

[51] Pelster, R.; Pieper, R.; Hüttel, I. *PhyDid* **2005**, *4*, 10–22.

[52] Snyder, G. J.; Toberer, E. S. *Nature Mater.* **2008**, *7*, 105–114.

[53] Maclachlan, J.; Kruesi, W.; Fray, D. *J. Mater. Sci.* **1992**, *27*, 4223–4229.

[54] Martín-González, M. S.; Prieto, R., A. L.; Gronsky; Sands, T.; Stacy, A. M. *J. Eletrochem. Soc.* **2002**, *149*, C546–C554.

[55] Leimkühler, G.; Kerkmann, I.; Reineke-Koch, R. *J.Electrochem. Soc.* **2002**, *149*, C474,C478.

[56] Bicer, M.; Kose, H.; Sisman, I. *J. Phys. Chem. C* **2010**, *114*, 8256–8263.

[57] Todoli, J.-L.; Hernandis, V.; Canals, A.; Mermet, J.-M. *J. Anal. At. Spectrom.* **1999**, *14*, 1289–1295.

[58] Olesik, J. W.; Fister, J. C. I. *Spectrochim. Acta Part B* **1991**, *46*, 851 – 868.

[59] Almagro, B.; Ganan-Calvo, A. M.; Hidalgo, M.; Canals, A. *J. Anal. At. Spectrom.* **2006**, *21*, 770–777.

[60] Reed, T. B. *J. Appl. Phys.* **1961**, *32*, 821–824.

[61] Greenfield, S.; Jones, I. L.; Berry, C. T. *Analyst* **1964**, *89*, 713–720.

[62] Wendt, R. H.; Fassel, V. A. *Anal. Chem.* **1965**, *37*, 920–922.

[63] Cammann, K., Ed. *Instrumentelle Analytische Chemie*; Spektrum Akademischer Verlag: Heidelberg, Berlin, **2001**.

[64] Fassel, V. A. *Science* **1978**, *202*, 183–191.

[65] Huang, M.; Hanselman, D. S.; Yang, P.; Hieftje, G. M. *Spectrochim. Acta Part B* **1992**, *47*, 765 – 785.

[66] Boss, C. B.; Fredeen, K. J. *Concepts, Instrumentation, and Techniques in Inductively Coupled Plasma Optical Emission Spectrometry*, 2nd ed.; Perkin Elmer: USA, **1997**.

[67] High Resolution ICP-OES Spectrometer for Routine Elemental Analysis Requirements in Environmental Protection, Academia and Industry. `http://www.jva.ie/PDF/Spectro/ARCOS_165_Brochure.pdf`, 07.03.2013.

[68] Cserfalvi, T.; Mezei, P.; Apai, P. *J. Phys. D* **1993**, *26*, 2184–2188.

[69] Grimm, W. *Spectrochim. Acta Part B* **1968**, *23*, 443 – 454.

[70] ELEMENT 2 & ELEMENT XR. `https://static.thermoscientific.com/images/D13061~.pdf`, 05.03.2013.

[71] SPECTRO MS Fully Simultaneous ICP-Mass Spectrometer. `http://www.spectro.com/pages/e/p010402tab_brochures.htm`, 05.03.2013.

[72] S2 Picofox Nutzerhandbuch. Bruker advanced X-ray solutions: Berlin, Germany, **2007**.

[73] Jenkins, R.; Manne, R.; Robin, R.; Senemaud, C. *Pure Appl. Chem.* **1991**, *63*, 735–746.

[74] http://lp.uni-goettingen.de/get/text/6634. `http://lp.uni-goettingen.de/get/text/6634`, 01.03.2013.

[75] Lechner, P.; Eckbauer, S.; Hartmann, R.; Krisch, S.; Hauff, D.; Richter, R.; Soltau, H.; Struder, L.; Fiorini, C.; Gatti, E.; Longoni, A.; Sampietro, M. *Nucl. Instrum. Meth. A* **1996**, *377*, 346–351.

[76] Behrens, P. *Trends in Anal. Chem.* **1992**, *11*, 237 – 244.

[77] Walsh, A. *Spectrochim. Acta Part B* **1955**, *7*, 108–117.

[78] High-Resolution Continuum Source AAS. `http://www.analytik-jena.de/fileadmin/content/Home/01_Analytical_Instrumentation/01_Produkte/01_Atomspektrometer/01_HR-CS_AAS/01_contrAA_300/br_contrAA_e_09_07_2012_low.pdf`, 10.03.2013.

[79] Heitmann, U.; Schütz, M.; Becker-Ross, H.; Florek, S. *Spectrochim. Acta Part B* **1996**, *51*, 1095 – 1105.

[80] Becker-Ross, H.; Florek, S.; Heitmann, U. *J. Anal. At. Spectrom.* **2000**, *15*, 137–141.

[81] Welz, B. *Anal. Bioanal. Chem.* **2005**, *381*, 69–71.

[82] Agilent 7700 Series ICP-MS. `http://www.chem.agilent.com/Library/brochures/5990-4025EN.pdf`.

[83] May, T. W.; Wiedmeyer, R. H. *At. Spectrosc.* **1998**, *19*, 150–155.

[84] Olesik, J. W.; Jones, D. In *Plasma Source Mass Spectrometry: Applications and Emerging Technologies*; Holland, J. G., Tanner, S. D., Eds.; RSC Publishing: Cambridge, **2003**; pp 261–270.

[85] D'Ilio, S.; Violante, N.; Majorani, C.; Petrucci, F. *Anal. Chim. Acta* **2011**, *698*, 6 – 13.

[86] Lobo, L.; Pisonero, J.; Bordel, N.; Pereiro, R.; Tempez, A.; Chapon, P.; Michler, J.; Hohl, M.; Sanz-Medel, A. *J. Anal. At. Spectrom.* **2009**, *24*, 1373–1381.

[87] Lobo, L.; Tuccitto, N.; Bordel, N.; Pereiro, R.; Pisonero, J.; Licciardello, A.; Tempez, A.; Chapon, P.; Sanz-Medel, A. *Anal. Bioanal. Chem.* **2010**, *396*, 2863–2869.

[88] Pisonero, J.; Lobo, L.; Bordel, N.; Tempez, A.; Bensaoula, A.; Badi, N.; Sanz-Medel, A. *Sol. Energ. Mater.* **2010**, *94*, 1352 – 1357.

[89] Falkenberg, G.; Clauss, O.; Swiderski, A.; Tschentscher, T. *X-Ray Spectrom.* **2001**, *30*, 170–173.

[90] `http://hasylab.desy.de/facilities/doris\_iii/beamlines/l\_hymo/index\_eng.html`, 20.06.2012.

[91] Ravel, B.; Newville, M. *J. Synchrotron Rad.* **2005**, *12*, 537–541.

[92] Newville, M. *J. Synchrotron Rad.* **2001**, *8*, 322–324.

[93] Schlemmer, G.; Welz, B. *Spectrochim. Acta Part B* **1986**, *41*, 1157–1165.

[94] Welz, B.; Borges, D. L. G.; Lepri, F. G.; Vale, M. G. R.; Heitmann, U. *Spectrochim. Acta Part B* **2007**, *62*, 873–883.

[95] Schumacher, C.; Reinsberg, K.-G.; Akinside, L.; Zastrow, S.; Heiderich, S.; Toellner, W.; Rampelberg, G.; Detavernier, C.; Broekaert, J. A. C.; Nielsch, K.; Bachmann, J. *Adv. Energy Mater.* **2012**, *3*, 345–352.

[96] Moß, K. K. *Determination of trace elements in thermoelectrical materials by TXRF and ICP-OES*. Bachelor Thesis, Universität Hamburg, **2010**.

[97] Andrade, J. M.; Cal-Prieto, M. J.; Gomez-Carracedo, M. P.; Carlosena, A.; Prada, D. *J. Anal. At. Spectrom.* **2008**, *23*, 15–28.

[98] Sadler, D. A.; Littlejohn, D. *J. Anal. At. Spectrom.* **1996**, *11*, 1105–1112.

[99] Daner, K.; Wagner, M. *Fresenius J. Anal. Chem* **1993**, *346*, 520–524.

[100] Salit, M. L.; Turk, G. C. *Anal. Chem.* **1998**, *70*, 3184–3190.

[101] Mermet, J.-M.; Ivaldi, J. C. *J. Anal. At. Spectrom.* **1993**, *8*, 795–801.

[102] Barnett, W. B.; Fassel, V. A.; Kniseley, R. N. *Spectrochim. Acta Part B* **1968**, *23*, 643–664.

[103] Salit, M. L.; Turk, G. C.; Lindstrom, A. P.; Butler, T. A.; Beck II, C. M.; Norman, B. *Anal. Chem.* **2001**, *73*, 4821–4829.

[104] Heo, P.; Hagiwara, K.; Ichino, R.; Okido, M. *J. Electrochem. Soc.* **2006**, *153*, C213–C217.

[105] XRD reference file, Stoe WinXPOW, Ver. 1.10 [15-874].

[106] Aabdin, Z.; Winkler, M.; Bessas, D.; König, J.; Peranio, N.; Eibl, O.; Hermann, R.; Böttner, H. *Mater. Res. Soc. Symp. Proc.* **2011**, *1329*.

[107] Goncalves, L.; Couto, C.; Alpuim, P.; Rowe, D. M.; Correia, J. H. Thermoelectric properties of Bi2Te3/Sb2Te3 thin films. 2006; 3rd International Materials Symposium/12th Meeting of the Sociedad-Portuguesa-da-Materials (Materials 2005/SPM), Univ Aveiro, Aveiro, PORTUGAL, MAR 20-23, 2005.

[108] Giani, A.; Boulouz, A.; Pascal-Delannoy, F.; Foucaran, A.; Charles, E.; Boyer, A. *Mater. Sci. Eng.* **1999**, *64*, 19–24.

[109] Biondi, M. A. *Phys. Rev.* **1952**, *88*, 660–665.

[110] Bogaerts, A. *J. Anal. At. Spectrom.* **2007**, *22*, 502–512.

[111] Morrison, G. H.; Cheng, K. L.; M.;, G. *Pure Appl. Chern.* **1979**, *51*, 2234–2250.

[112] Pisonero, J. *Anal. Bioanal. Chem.* **2006**, *384*, 47–49.

[113] McClenathan, D. M.; Hieftje, G. M. *J. Anal. At. Spectrom.* **2005**, *20*, 1326–1331.

[114] Stoe WinXPOW, Ver. 1.10, Stoe Darmstadt, Germany.

[115] Wu, K. H.; Hung, C. I.; Ziolkowski, P.; Platzek, D.; Karpinski, G.; Stiewe, C.; Mueller, E. *Rev. Sci. Instrum.* **2009**, *80*, 105104.

[116] Resano, M.; García-Ruiz, E. *Anal. Bioanal. Chem.* **2011**, *399*, 323–330.

[117] Welz, B.; Becker-Roß, H.; Florek, S.; Heitmann, U. *High-resolution continuum source AAS*; Wiley-VCH: Weinheim, **2005**.

[118] Welz, B.; Vale, M. G. R.; Silva, M. M.; Becker-Ross, H.; Huang, M. D.; Florek, S.; Heitmann, U. *Spectrochim. Acta Part B* **2002**, *57*, 1043–1055.

List of own Publications

[1] Scheele, M.; Oeschler, N.; Veremchuk, I.; Reinsberg, K.-G.; Kreuziger, A.-M.; Kornowski, A.; Broekaert, J. A. C.; Klinke, C.; Weller, H. ZT Enhancement in Solution-Grown $Sb_{2x}Bi_xTe_3$ Nanoplatelets *Nano Letters* **2010**, *4*, 4283-4291.

[2] Reinsberg, K.-G.; Schumacher, C.; Nielsch, K.; Broekaert, J. A. C. Precision improvements by the use of principal component regression and pooled regression applied to main component determinations with ICP-OES for thermoelectric films *J. Anal. At. Spectrom.* **2011**, *26*, 2477-2482.

[3] Schumacher, C.; Reinsberg, K.-G.; Akinside, L.; Zastrow, S.; Heiderich, S.; Toellner, W.; Rampelberg, G.; Detavernier, C.; Broekaert, J. A. C.; Nielsch, K.; Bachmann, J. Optimization of Electrodeposited p-Doped Sb_2Te_3 Thermoelectric Films by Millisecond Potentiostatic Pulses *Adv. Energy Mater.* **2012**, *3*, 345-352.

[4] Reinsberg, K.-G.; Schumacher, C.; Tempez, A.; Nielsch, K.; Broekaert, J. A. C. Depth-profile analysis of thermoelectric layers on Si wafers by pulsed r.f. glow discharge time-of-flight mass spectrometry *Spectrochim. Acta Part B* **2012**, *76*, 175-180.

[5] Schumacher, C.; Reinsberg, K.-G.; Rostek, R.; Akinsinde, L.; Baessler, S.; Zastrow, S.; Rampelberg, G.; Woias, P.; Detavernier, C.; Broekaert, J. A. C.; Bachmann, J.; Nielsch, K. Optimizations of Pulsed Plated p and n-type Bi_2Te_3-Based Ternary Compounds by Annealing in Different Ambient Atmospheres *Adv. Energy Mater.* **2013**, *3*, 95-104.

[6] Reinsberg, K.-G.; Schumacher, C.; Zastrow, S.; Nielsch, K.; Broekaert, J. A. C.; Fittschen, U. E. A. Investigation on the homogeneity of pulsed electrochemically deposited thermoelectric films with synchrotron µ-XRF, µ-XRD and µ-XANES *J. Mater. Chem. A* **2013**, *1*, 4215-4220.

List of Figures

List of Tables

List of Abbreviations

κ	Thermal conductivity
λ	Wavelength
μ	Absorption coefficient
ν	Frequency
σ	Electrical conductivity
θ	Angle
a_{lat}	Lattice constant
c	Concentration
c_{lat}	Lattice constant
c_{light}	Velocity of light
D	Crystallite size
d	Distance
E	Energy
e	Elementary electric charge
F	Faraday constant
$FWHM$	Full width at half maximum
h	Planck constant

I	Intensity
k	Boltzmann constant
m	Mass
R	Gas constant
r^2	Correlation coefficient
S	Seebeck coefficient
T	Temperature
t	Time
U	Electrode potential
U^0	Standard electrode potential
v	Velocity
z	Charge
ZT	Thermoelectric figure of merit
AAS	Atomic absorption spectrometry
ALD	Atomic layer deposition
CCD	Charge coupled device
CI	Confidence interval
dc	Direct current
DESY	Deutsche Elektronen Synchrotron
EDL	Electrodeless discharge lamp
EDS	Energy dispersive X-ray spectrometry
EXAFS	Extended X-ray absorption fine structure

FEL	Free electron laser
GD	Glow discharge
GF	Graphite furnace
HASYLAB	Hamburger Synchrotronstrahlungslabor
HCL	Hollow cathode lamp
HMI	High matrix introduction
HR	High resolution
ICP	Inductively coupled plasma
IUPAC	International union of pure and applied chemistry
K	Electron shell
KED	Kinetic energy discrimination
L	Electron shell
LOD	Limit of detection
LOQ	Limit of quantification
M	Electron shell
MBE	Molecular beam epitaxy
MS	Mass spectrometry
OES	Optical emission spectrometry
PCR	Principal component regression
PP-TOFMS	Plasma profiling time of flight mass spectrometry
PSM	Potential seebeck microprobe
PTFE	Polytetrafluorethylene

rf	Radio frequent
RSD	Relative standard deviation
SDD	Silicon drift detector
SEM	Scanning electron microscopy
SIMS	Secondary ion mass spectrometry
TEG	Thermoelectric generator
TEM	Tunneling electron microscopy
TOF	Time-of-flight
TXRF	Total reflection X-ray fluorescence
WDS	Wavelength dispersive X-ray Spectrometry
XANES	X-ray absorption near edge structure
XRD	X-ray powder diffraction
XRF	X-ray fluorescence

Chemicals

In Table 8.1 the used chemicals and their GHS classifications are listed.

Table 8.1: Used chemicals and CMR substances.

substance	pictogram	H-sentences	P-sentences
HNO_3, 65%	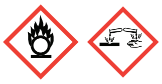	272-314-290	301+330+331-305+351+338-309+310
HCl, 35%		314-335	260-301+330+331-303+361+353-305+351+338-405+501
Sb_2Te_3		302+332+411	6-273-301+312-304+340-312-501
Bi_2Te_3		302-312-332-315-319-335	261-305+351+338-302+352-321-405-501A
Bi-standard solution		290-315-319	302+352-305+351+338
Sb-standard solution		290	-
Te-standard solution		290-315-319	302+352-305+351+338
Se-standard solution		290-315-319	302+352-305+351+338
multi-element standard solution VI		350-290-314	201-280-301+330+331
Petroleum ether		224-304-315-373-411	210-261-273-301+310-331

Eidesstattliche Versicherung über das selbstständige Verfassen der vorliegenden Dissertationsarbeit

Hiermit versichere ich, Dipl. Chem. Klaus-Georg Reinsberg, geboren am 17.09.1983 in Köln, an Eides statt, dass ich die vorliegende Dissertationsarbeit selbstständig verfasst und keine anderen als die angegebenen Hilfsmittel benutzt habe. Alle Stellen, die dem Wortlaut oder dem Sinne nach anderen Texten entnommen sind, wurden unter Angabe der Quellen (einschließlich des World Wide Web und anderer elektronischer Text- und Datensammlungen) und nach den üblichen Regeln des wissenschaftlichen Zitierens nachgewiesen. Dies gilt auch für Zeichnungen, bildliche Darstellungen, Skizzen, Tabellen und dergleichen.

Hamburg, 20.06.2013

Erklärung über frühere Promotionsversuche

Hiermit erkläre ich, dass ich mich bisher nicht um einen Doktorgrad beworben habe.

Hamburg 20.06.2013

CURRICULUM VITAE

Entfällt aus datenschutzrechtlichen Gründen.